Palacký University Olomouc

Faculty of Science

DOCTORAL THESIS

Taras Chutora

Study of molecular structures on solid state surfaces

Department of Experimental Physics and Joint Laboratory of Optics

Supervisor of the doctoral thesis:	prof. RNDr. Miroslav Hrabovský, DrSc.
Consultants:	Ing. Pavel Jelínek, PhD.
	Bruno de la Torre, PhD.
Study programme:	Physics
Specialization:	Applied Physics

Olomouc 2019

Acknowledgements

Undertaking this PhD has been a truly life-changing experience for me and it would not have been possible to do without the support and guidance that I received from many people.

First of all, I would like to express my sincere gratitude to my supervisors prof. RNDr. Miroslav Hrabovský and Ing. Pavel Jelínek, PhD. for the continuous support of my Ph.D study and related research, for they patience, motivation, and immense knowledge. They guidance helped me in all the time of research and writing of this thesis. I could not have imagined having a better advisors and mentors for my Ph.D study.

I would also like to express my special thanks to Dr. Bruno de la Torre and Dr. Martin Sveč for teaching me the fundamentals of STM and AFM measurement. Without their precious support, it would not be possible to conduct this research. I would like to extend my sincere thanks to Dr. Jack Hellerstedt for his insightful comments and critical review of the thesis.

I'm grateful to all my colleagues from the "Nanosurf Lab" Jesus Lopez Roso, Dr. Oleksandr Stetsovych, Dr. Jan Berger, Alesh Cahlik, Benjamin Mallada Faes, Dr. Mykola Telychko, Dr. Maria Moro, Santhini Vijai Meena and Dr. Héctor González for their support and help with experiments. It was a great pleasure for me to work with all of them. I'm also grateful to theoreticians Dr. Hector Vazquez, Dr. Pingo Mutombo, Shayan Edalatmanesh, Dr. Martin Ondracek. who performed the theoretical calculations presented in this thesis. Without their contribution, the correct interpretation of the experimental data would be hardly possible. I would like to thank my collaborators Ana Sánchez-Grande, Dr. Borja Cirera, Dr. Koen Lauwaet and Dr. David Écija.

Finally, I want to thank my family and all the friends who supported me during this time. Especially I want to thank my dear mom for her endless love, understanding and support throughout all these years and my loving and supportive girlfriend, Angelina who provide unending inspiration.

I declare that I carried out this doctoral thesis independently, and only with the cited sources, literature and other professional sources.

I understand that my work relates to the rights and obligations under the Act No. 121/2000 Sb., the Copyright Act, as amended, in particular the fact that the Palacký University Olomouc has the right to conclude a license agreement on the use of this work as a school work pursuant to Section 60 subsection 1 of the Copyright Act.

In ..... date ..... Ing. Taras Chutora

Název práce: Studium molekulárních struktur na povrchu pevných látek

Autor: Taras Chutora

Katedra experimentální fyziky a Společná laboratoř optiky

Vedoucí disertační práce: prof. RNDr. Miroslav Hrabovský, DrSc.,

Konzultanti: Ing. Pavel Jelínek, PhD., Bruno de la Torre, PhD.

Abstrakt: Pro vývoj nové generace nanozařízení jsou klíčové pokroky v porozumění molekulárním strukturám a jejich povrchové konformaci. Z experimentálního hlediska nabízí techniky mikroskopie skenující sondou (SPM) jedinečnou příležitost charakterizovat a manipulovat jednotlivými molekulami v atomárním měřítku. V této práci je představen výzkum fyzikálně-chemických vlastností nanostruktur na bázi fullerenu a hledání nových způsobů povrchové syntézy jednorozměrných molekulárních drátů. Dále je pak prezenrována nová slibná funkcionalizace SPM hrotu, která umožňuje zobrazení povrchových molekulárních struktur v atomárním rozlišení. Všechny experimentální výsledky této práce jsou podloženy nejmodernějšími teoretickými výpočty.

V první části této práce jsou prezentovány výsledky kombinovaného experimentálního a teoretického výzkumu řízené modifikace molekul fullerenu na povrchu Au(111). Použitím nízkoenergetického (120 eV) Ar^+ iontového naprašování jsou vytvářeny nanostruktury odvozené od fullerenu a to při pokojové teplotě. Takové nanostruktury vykazují zvýšenou chemickou interakci se substrátem pomocí stabilních vazeb Au-C.

V druhé části této práce je prezentována nová podrobná metodologie funkcionalizace SPM hrotu s novým molekulárním kandidátem. Úspěšně byl funkcionalizován vrchol Au hrotu s jednou molekulou oxidu dusného (N_2O) a porovnám jeho schopnosti zobrazením molekul FePc s submolekulárním rozlišení a získáním místně specifických silových spektroskopií. Výsledky jsou kvantitativně i kvalitativně porovnány s výsledky získanými pomocí široce využívaných hrotů z oxidu uhelnatého (CO).

Následuje použití povrchové syntézy pro přípravu nízkoelektronového bandgap polymeru založeného na anthracenových molekulárních stavebních blocích. Byly znázorněny cestu syntézy s důrazem na tři hlavní kroky: dehalogenace, difúze molekul na povrchu a homocoupling. Dále budou charakterizovány elektronické a konformační vlastnosti polymeru pomocí nízkoteplotní skenovací tunelové mikroskopie a měření mikroskopie atomové síly (LT-STM/AFM) a teoretických výpočtů.

Klíčová slova: LT-STM/AFM, funkcionalizace hrotu, nanostruktury, molekulární elektronika

Title: Study of molecular structures on solid state surfaces

Author: Taras Chutora

Department of Experimental Physics and Joint Laboratory of Optics

Supervisor: prof. RNDr. Miroslav Hrabovský, DrSc.,

Consultants: Ing. Pavel Jelínek, PhD., Bruno de la Torre, PhD.

Abstract: Advances in understanding of molecular structures and their conformations on surfaces are crucial for developing the next generation of nanodevices. From an experimental point of view, Scanning Probe Microscopy (SPM) techniques offer the unique possibility to characterize and manipulate single molecules at the atomic scale. In this thesis, we present investigations of the physicochemical properties of fullerene-based nanostructures and exploration of new routes for on-surface synthesis of one-dimensional molecular wires. Moreover, we demonstrate a new promising SPM tip functionalization which enables atomic resolution imaging of molecular structures on a surface. All the experimental findings of this thesis are supported by state-of-the-art theoretical calculations.

In the first part of this thesis, we show results of our combined experimental and theoretical investigation of controlled modification of fullerene molecules on Au(111) surface. By using low-energy (120 eV) Ar^+ ion sputtering we create fullerene-derived nanostructures at room temperature. Such nanostructures show enhanced chemical interaction to the substrate via formation of stable Au-C bonds.

In the second part of this thesis, we present a detailed novel methodology for SPM tip functionalization with a new molecular candidate. We successfully functionalize the Au tip apex with a single nitrous oxide molecule (N_2O) and benchmarked its capabilities by imaging FePc molecules with sub-molecular resolution and acquiring site-specific force spectroscopies. The results are both quantitatively and qualitatively compared to those obtained with widely used carbon monoxide (CO) tips.

Finally, we use on-surface synthesis to engineer a low electronic bandgap polymer based on anthracene molecular building blocks. We illustrate the pathway of the synthesis emphasizing three major steps: dehalogenation, diffusion of the molecules on the surface and homocoupling. We further characterize the electronic and conformational properties of the polymer by means of low-temperature scanning tunnelling microscopy and atomic force microscopy (LT-STM/AFM) measurements and theoretical calculations.

Keywords: LT-STM/AFM, tip functionalization, nanostructures, molecular electronics

Contents

Introduction

In the last several decades, continuous miniaturization of computer technology has revolutionized the way people access information and communicate. The main cause of such rapid development of electronic devices is the ability to double the number of the electronic components on integrated circuits every two years, a trend commonly referred to as Moore's law[1]. However, the most widely applied silicon-based technology will soon hit fundamental quantum performance limitations[2] preventing further size reduction.

One well-established approach to overcome this limitation is to use molecular electronics which take advantages of electronic and chemical properties of selected molecules with designed functionalization[3]. Ultimately, the goal is to use a single molecule as the building block for electronic circuitry. This approach will allow realization of electronic components (transistors and diodes) at the limit of miniaturization[4]. Using a single molecule as a building block for electronic devices was first proposed by Aviram and Ratner in 1974[5]. Since then the field has advanced mainly due to instrumental developments.

One significant advance was the realization of scanning tunneling microscopes (STM) in an ultra-high vacuum (UHV) environment, which enables unprecedented visualization and manipulation of single molecules at the atomic scale[6;7]. STM allows to access molecular electronic and conformational properties[8]. In addition, STM experiments give insight on electron transport through single-molecule junctions[9;10], elastic and inelastic molecular vibration modes[11–13], magnetic properties[14–16]and can be used to spatially resolve unperturbed molecular orbitals[17;18]. On top of this, the STM has extraordinary capability for atom manipulation with picometer accuracy as pioneered by D. Eigler at IBM Almaden[19]. This technique has been further employed for triggering selected molecular reaction on the surface[20–22].

Shortly following the development of STM, Atomic Force Microscopy (AFM)[23] provides the capability to perform reliable atomic scale experiments on low conductive surfaces due to its sensitivity to interacting forces between the tip apex and the outermost atoms on the surface. Interestingly, AFM allows the measurement of forces required for controllable manipulation of individual adatoms on a surface[24] and to operate a single molecule switch[25]. The introduction of the qPlus sensor[26;27] allows for simultaneous STM and AFM measurements while operating in the non-contact regime with stable small oscillation amplitudes which enhances sensitivity to short range forces. Enhanced resolution can be achieved with a functionalization of the tip-apex with small and low-reactive species[28] previously adsorbed on the surface. In particular, the functionalization of the tip apex with a CO molecule leads to unprecedented spatial resolution of a single

molecule on a surface. In the pioneering work of Gross et al[29], the atomic structure of the pentacene molecule is clearly resolved in AFM images, pushing forward the resolution of the technique and opening new routes for atomic scale characterization of molecular structures in surfaces[30] with a rising number of applications. For example, it has been successfully used for determination of single molecular adsorption configuration[31], bond order determination[32], visualization of the intermolecular charge distribution[33;34] and discrimination of the spin state of a single molecule[35]. Additionally, sub-molecular resolution was also achieved using scanning tunneling hydrogen microscopy (STHM)[36] where hydrogen molecules are added to the tunneling junction.

The advantages of tip functionalization can be also applied to explore results of single-molecule chemical reactions[37]. The atomic structure of the reaction products and coupling of nanostructures can be visualized using STM and AFM with a functionalized tip. On-surface chemical reactions can be induced in two ways: by using STM/AFM tip manipulation methods[21], or with the help of external stimulus such as thermal annealing[38], light excitations[39;40], or plasmons[41]. On surface synthesis using atomic manipulation (electron injection) enables the formation of various molecular spices such as triangulene[42] and aryne[43] which cannot be synthesized using conventional wet chemistry. Thermal annealing of precursor molecules adsorbed on a metallic surface has been demonstrated to form covalently bonded polymers[44] or metal organic coordinated complexes[45]. This method was also used for the synthesis of nanostructures such as graphene nanoribbons[46].

In this thesis, a combination of Variable Temperature STM (VT-STM) and Low Temperature (LT-STM/AFM) was used to study different molecular structures on a Au(111) surface with atomic resolution. We investigated the formation of fullerene-derived nanostructures on Au(111) at room temperature (RT) with enhanced chemical properties. We investigated the possibility of AFM tip functionalization with a single N_2O molecule to extend its imaging capabilities. Also, we used CO functionalized tips to study on-surface formed anthracene-based polymeric wires and characterize their electronic properties. The objective is to get more insight on new nanostructures which can be used for molecular electronics applications.

The thesis is structured as follows: In Chapter 1, I give an extended literature review and introduce the experimental techniques applied during this thesis describing briefly the experimental and theoretical principles underlying the STM and AFM techniques. In Chapter II, I provide a general overview of the operation a VT-STM (Scienta Omicron GmbH) and an LT-STM/AFM (Createc Fischer & Co. GmbH). I give a detailed description of *in-situ* tip preparation and tip functionalization with CO molecules at cryogenic temperatures (5 K). Also, I include

a small description of Au(111) sample preparation and describe the molecular deposition technique used in experiments.

The main results of the thesis are presented in Chapter III. First, we use STM along with Density Functional Theory (DFT) calculations for investigation of stable fullerene-based nanostructures on Au(111) at RT (Subchapter 3.1 Paper I page 35). These structures were formed by soft Ar^+ ion bombardment of self-assembled fullerene islands. Next, we explore and test new molecular candidates for tip functionalization to gain insights into the origin of high-resolution AFM images (Subchapter 3.2 Paper II page 46). We functionalized an Au tip with a single N_2O molecule from the surface and benchmarked its capabilities by imaging isolated FePc molecules. Finally, by using on-surface synthesis we create low-band-gap π-conjugated polymers (Subchapter 3.3 Paper III page 58). With the help of high-resolution AFM/STM imaging we reveal the bonding motive of the polymer.

1. Experimental methods "Current State of Research"

1.1 Scanning Tunneling Microscopy

Richard Feynman in his famous lecture "There's Plenty of room at the Bottom: An Invitation to Enter a New Field of Physics" [47] introduces a new field of physics which reveals the fascinating world of the atom, as governed by Quantum Mechanics. In 1981 Gerd Binnig and Heinrich Rohrer from IBM invented and built the very first Scanning Tunneling Microscope (STM)[6;7] which enabled imaging individual atoms in real space[48], and laid the foundation of nanotechnology research. These achievements were recognized by the Nobel Prize in Physics in 1986[49]. The STM quickly became the premier experimental technique for nanotechnology and surface science. The atomic-scale structure, local electronic, vibrational and magnetic properties of surfaces and adsorbates can be directly probed[11;13;14;17;50;51]. Additionally STM is a powerful tool for the atomic manipulation[19;52–54] capable of arranging novel structures at the atomic level[55].

1.1.1 Basics of Scanning Tunneling Microscopy

The STM is an extremely sensitive surface technique that uses quantum mechanical tunneling as a sensing method. Figure 1.1. shows a schematic representation of the essential components of the STM setup. The core element of the STM is an atomically sharp probing tip, commonly made of tungsten or platinum-iridium alloy. To ensure precise movement of the probe in three dimensions it is attached to a piezo motor, which has tube shape made of piezoceramics (poled in a radial direction). The piezo tube has an inner and outer metallic coating, where the outside is sectioned into five quadrants. The movement of the tube (i.e. bend, change dimensions) is achieved via the inverse piezoelectric effect with picometer accuracy: by applying voltage between corresponding metal contacts movement is affected[56;57]. To initiate the tunnelling process, the distance between the atomically sharp STM tip and the sample has to be reduced to only a few angstroms which will lead to an overlap of the wave functions. Subsequent applying of a low bias voltage between tip and the sample will induce a quantum mechanical tunnelling current between the two. The tunneling concept will be discussed in the next section.

The tunnelling current is typically in the range of 1 pA to 10 nA and measured with a current to voltage converter. The tunnelling current has exponential dependence on the distance between the tip and the sample which will be shown in

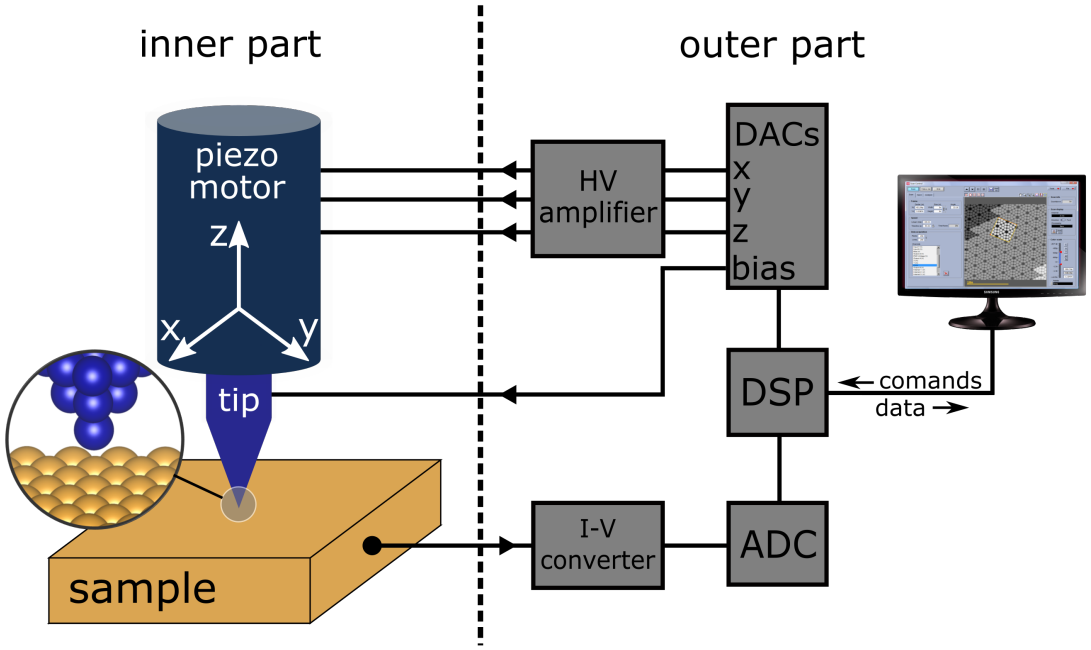

Figure 1.1: STM system overview.

the next section. The current to voltage converter will produce a voltage proportional to the given current. The obtained value is then digitized using analogue to digital converter (ADC) and sent to a digital signal processor (DSP). The DSP acts as a digital feedback loop, calculating and sending corresponding voltages to adjust the vertical position of the piezo motor[56].

The STM has two main modes of operation: constant current and constant height mode as shown on Fig. 1.2. In the constant current mode, the feedback loop maintains constant tunnelling current by continuously adjusting the distance between the tip and the sample. The voltage applied to modify tip heights is used to produce a topographic image of a scanned sample area. This mode is used for studying stepped surfaces and different types of adsorbates[57].

On the other hand, in constant height mode, the feedback is switched off and the tip scans with the defined constant separation from the sample while recording the tunnelling current as a function of lateral tip position. This mode of operation can be applied only to atomically flat samples and can be used to visualize the local density of states (LDOS)[57].

1.1.2 The concept of tunneling effect

The tunnelling effect is a quantum mechanical phenomenon, which acts as a sensing method and provides a high degree of sensitivity required for imaging atoms and molecules on surfaces. We can consider a simple model of vacuum tunneling between two metals (see Fig. 1.3 a) to understand atomic sensitivity of the STM.

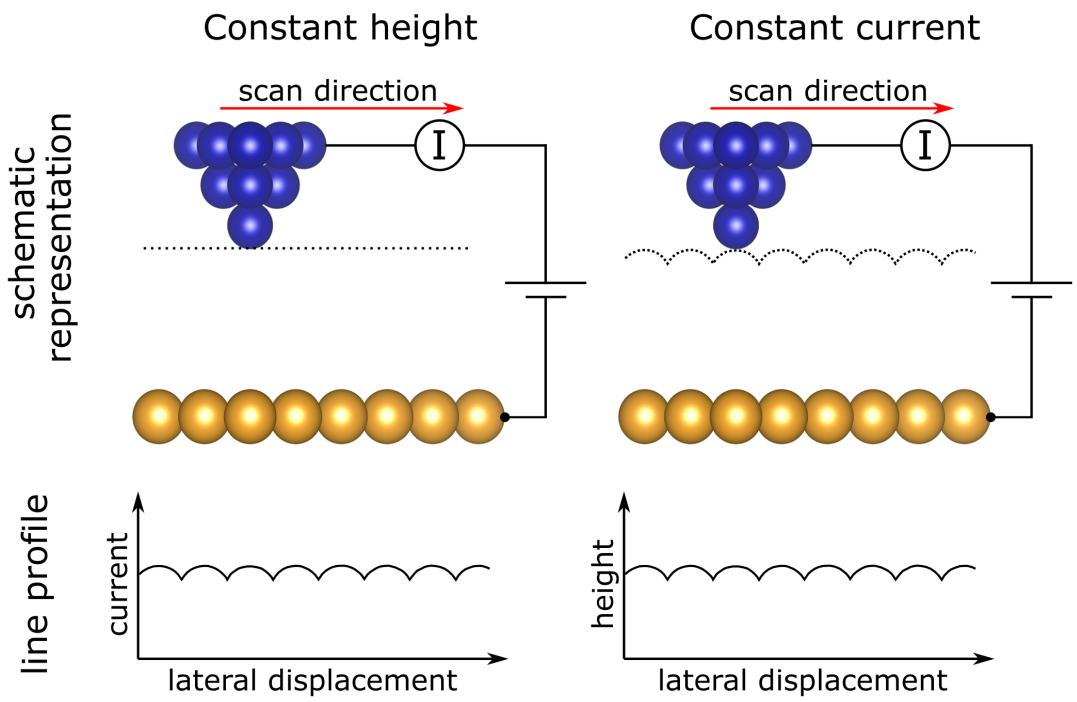

Figure 1.2: Schematic representation of the STM operating modes.

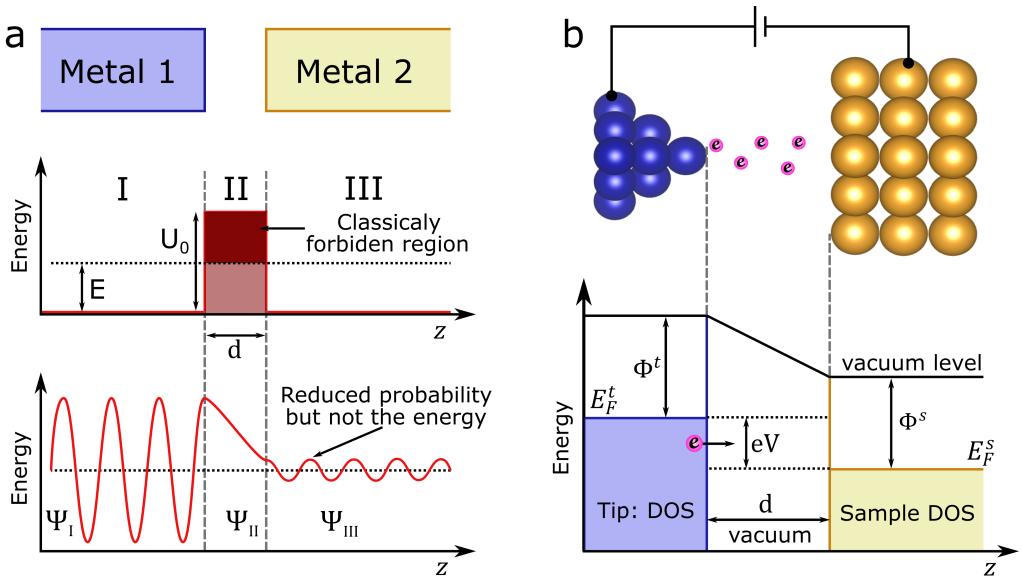

Figure 1.3: Schematic representation of the tunneling effect. (a) Simple one-dimensional model of the metal-vacuum-metal tunneling junction (b) One-dimensional representation of the tip sample vacuum junction.

In the one-dimensional potential barrier tunneling model, the vacuum gap is modelled as a potential barrier $U(z)$ with the height of U_0, thickness (d), and the energy of the electron (E), schematically represented on Fig. (1.3 a). The electron wave function for the one-dimensional square barrier can be analytically solved using the Schrodinger equation. The Schrodinger equation for such system reads as follows:

$$-\frac{\hbar^2}{2m}\frac{\mathrm{d}^2\Psi}{\mathrm{d}z^2} + U(z)\Psi = E\Psi \tag{1.1}$$

Where m is a mass of the electron, $U(z)$ is potential describing the barrier, E is the energy of the electron, $\hbar$ is the reduced Planck's constant and wave function (Ψ). The solution for the wave function (Ψ) outside the potential barrier in regions I and III were $U(z) = 0$ reads as follows:

$$\Psi_1(z) = e^{ikz} + Ae^{-ikz} \tag{1.2}$$

$$\Psi_3(z) = De^{ikz} \tag{1.3}$$

Where A and D complex number with amplitude and phase and $k = \frac{\sqrt{2mE}}{\hbar}$ the wave number. The Eq. 1.2 and 1.3 involves a complex notation which represents the wave function of the free electron in regions (I) and (III). In region (II), inside the barrier where $U = U_0$, the wave function it no longer complex and changes to a simple exponential with respect to z given by:

$$\Psi_2(z) = Be^{-\alpha z} + Ce^{\alpha z} \tag{1.4}$$

Where B and C are complex numbers with amplitude and phase and $\alpha = \sqrt{2mE(U_0 - E)}/\hbar$ is the inverse decay length. Now if the single electron is described by the wave function (Ψ) we can define a probability current density (j) given by:

$$j = \frac{-i\hbar}{2m}\left[\Psi^*\frac{d\Psi}{dz} - \Psi\frac{d\Psi^*}{dz}\right] \tag{1.5}$$

By evaluating the probability current density we can obtain the transmitted current (current after the barrier) and incident current(current before the barrier). The ratio of transmitted current to incident current will give us the transmission probability T which reads as follow:

$$T \cong \frac{j_{trans.}}{j_{inc.}} = |D|^2 = \frac{4k^2\alpha^2}{(k^2\alpha^2)^2\sinh^2(\alpha d) + 4k^2\alpha^2} \tag{1.6}$$

The transmission probability (T) is not zero which means we have certain probability to find the electron at the end of potential barrier. If we take a further assumption $\alpha d \gg 1$ (wide barrier) the term $\sinh^2$ can be approximated

by $\sinh^2(\alpha d) \approx \frac{1}{4}e^{2\alpha d}$ and transmission factor becomes:

$$T \cong \frac{16k^2\alpha^2}{(k^2+\alpha^2)^2}e^{-2\alpha d} \tag{1.7}$$

The transmission probability is exponentially sensitive to the width of the tunnelling barrier which is defined by the tip height (d). Therefore, the tunneling current can be expressed as:

$$\boxed{I \propto T \propto e^{-2\alpha d}} \tag{1.8}$$

From Eq. 1.8 it follows that the tunnelling current has exponential dependence on the tip-sample separation. However, reality is more complex (see Fig. 1.3 b). For a qualitative description of the tunneling process the current model has to be extended. We have to include the electronic structure (density of states (DOS)) of the tip and the sample. The following expression for the tunneling current according to the Bardeen theory[58] reads as:

$$I = \frac{4\pi e}{\hbar}\int_0^{eV} \rho_{tip}(E-eV)\rho_{sam.}(E)|M(E)|^2 dE \tag{1.9}$$

Where I is the tunneling current, ρ_{tip} and $\rho_{sam.}$ are the DOS for the tip and the sample respectively. $|M(E)|^2$ is a matrix element which represents an overlap of the tip and the sample wave functions which exponentially decays in the vacuum gap[58].

$$M(E) = \frac{\hbar}{2m}\int_S [\Psi_{tip}\nabla\Psi^*_{sam} - \Psi_{sam}\nabla\Psi^*_{tip}]dS \tag{1.10}$$

The calculation of tunnelling matrix elements obeys selection rules according to the tip and sample frontier orbital symmetry. With the help of the Tersoff -Hamann approximation (THA) which represents the tip as a spherical s-like orbital with a certain radius (s-like tip shape)[59] the Eq. 1.9 can be further simplified:

$$\boxed{I \propto \int_o^{eV} \rho_{samp.}dE} \tag{1.11}$$

Equation 1.11 shows that the THA of the tunneling current is directly proportional to the local density of states (LDOS) integrated from 0 to the applied bias voltage (eV) near the Fermi level of the sample.

1.1.3 Scanning tunneling spectroscopy

From Eq. 1.11, we can see that tunneling current depends on the LDOS of the surface. By differentiating tunneling current with respect to the voltage, we can

obtain the local dynamic conductance $\frac{dI}{dV}$:

$$\boxed{\frac{dI}{dV} \propto \rho_{samp.}(eV)} \tag{1.12}$$

In this approximation,ρ_{tip} is assumed to be a constant for the given energy interval. Thus, the $\frac{dI}{dV}$ spectra provides direct measurements of the LDOS of the surface. The acquisition of $\frac{dI}{dV}$ curves with STM is known as scanning tunnelling spectroscopy (STS). By applying positive (negative) voltage to the tip with respect to the sample occupied (empty) electronic states of the sample surface are measured.

The experimental realization of spectroscopy measurements using STM are generally performed in the following way. The STM tip is located at the specific point of interest, the bias voltage and tunnelling current are set to a certain stabilization value (varies between investigated systems). Then feedback is switched off and the $\frac{dI}{dV}$ spectrum is recorded in the desired range of voltages. Usually, the $\frac{dI}{dV}$ signal is recorded using a lock-in amplifier which yields better signal to noise ratio in comparison to the numerical calculation from the $\frac{I}{V}$ curve. A detailed description of the lock-in technique can be found elsewhere[56].

1.2 Atomic Force Microscopy

Regardless of the remarkable success of STM as a tool for surface science, its imaging capability is limited to conductive samples. This restricts the usage of STM to metal and semiconductor surfaces. To overcome this limitation, in 1986 Atomic Force Microscopy (AFM) was introduced by G. Binnig and coworkers[23]. AFM relies on sensitivity to the force emerging from interatomic interactions between the tip and sample. Consequently, the AFM can be used to measure insulating samples. The core element of the AFM is a flexible cantilever which acts as a force sensor as shown schematically on Fig. 1.4.

Generally, AFM has two modes of operation: the static mode and dynamic mode. In the static mode of operation, the forces acting between tip and sample lead to deflection of the scanning cantilever. The most common way to measure cantilever bending is the laser beam deflection method[56]. However, achieving atomic resolution in static mode is not straightforward. Mainly due to the strong long-range forces such as attractive van der Waals forces and electrostatic forces, which trigger an undesired jump-to-contact while scanning in small tip-sample separations. Presently, the static mode is the most frequently used mode of AFM when operating in ambient conditions or in liquids[56].

In dynamic mode AFM the cantilever is mechanically excited to oscillate. This allows stable measurements at small tip sample separation, while avoiding jump-to-contact[27]. There are two main force (tip-sample interatomic force) detecting

schemes for the dynamic mode of operation: amplitude modulation (AM)[60] and frequency modulation (FM)[61]. Obtaining true atomic resolution with AFM requires a stable condition which can be achieved by operating at low temperature (LT, typically 5K) under ultrahigh vacuum (UHV,$< 10^{-8}$ mbar).

AM-AFM have a considerably slower scanning speed in comparison to FM-AFM due to the high quality-factor (Q-factor) of the cantilever in vacuum (e.g., the resonant frequency response). The changes in amplitude caused by interatomic interaction in AM-AFM are not instant, they occur over a time period which is proportional to the Q-factor. As a result, AM-AFM is used mostly in ambient conditions. All AFM data in this thesis were obtained with the help of dynamic AFM which use a FM detecting scheme and operates in LT under UHV conditions which are usually abbreviated as FM-AFM or noncontact AFM (nc-AFM).

1.2.1 Basics of FM-AFM

The design of the FM-AFM has one crucial difference in comparison to STM, the metal tip is replaced with a force sensor which is connected to a piezo actuator (see Fig. 1.4). Currently, there are two commonly used force sensors in UHV systems: the qPlus[26] and Kolibri[62]. The main element in both sensors is a quartz oscillator (tuning fork for qPlus or linear extension resonator for Kolibri) which allows for precise deflection measurements. The quartz oscillator usually requires a small amount of energy and therefore it does not produce additional heat in the system which makes it perfectly suitable for use in LT conditions[27]. The quartz oscillator typically has large stiffness and high Q -factor in vacuum conditions.

Figure 1.4 shows a typical implementation for a combined LT-STM/AFM microscope which was used for the data presented in this thesis. The microscope is equipped with a qPlus force sensor which consists of a tuning fork with one prong attached to a heavy substrate and metal tip (PtIr or W) mounted onto the free oscillating prong. Every qPlus sensor is characterized by four main parameters: the stiffness (k), quality factor (Q), eigenfrequency (f_0) and oscillation amplitude (A). The qPlus sensor allows stable force measurement and increases the signal-to-noise ratio, which is beneficial for short range force sensitivity[63]. Additionally, the sensor enables simultaneous STM/AFM measurement[27]. The typical parameters for a commercial qPlus sensor operating in cryogenic temperatures under UHV condition are the following:$f_0 \sim 30$ kHz, $Q \sim 30$ k, $k \sim 1.8$ kNm^{-1}, $A = 50 - 100$ pm.

Figure 1.4 illustrates the feedback scheme of the FM-AFM. First, the tip-sample interactions (force gradient) are measured with a deflection sensor. A current-to-voltage transducer converts the sensor signal to a voltage modulation

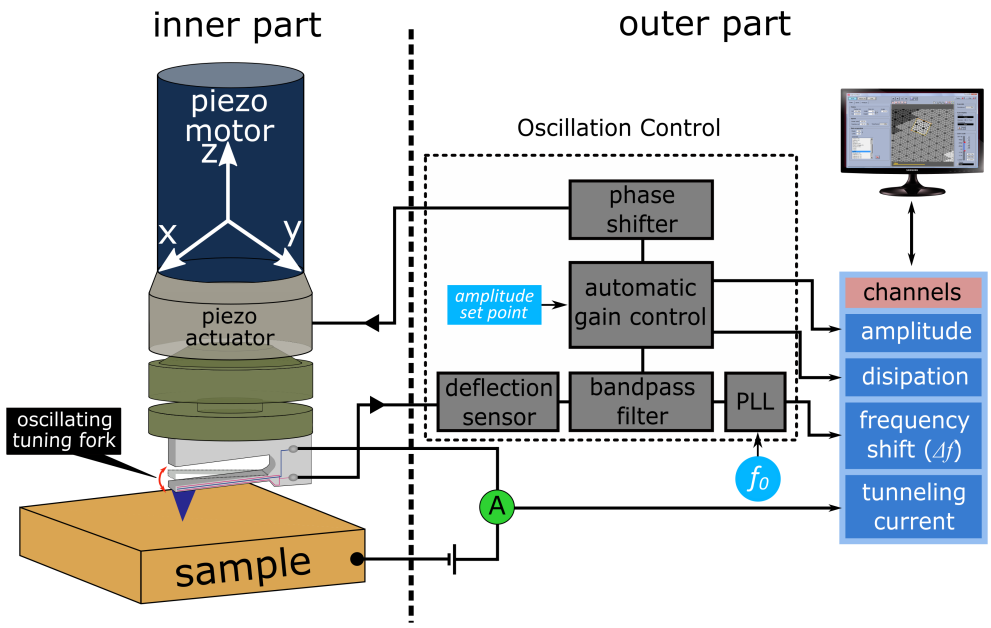

Figure 1.4: Scheme of FM-AFM with qPlus sensor. The inner part represents a simplified scheme of the AFM head. The outer part represents the block diagram of the oscillation control unit for constant amplitude control and frequency shift measurements. The tuning fork deflection is measured with a current-to-voltage converter and fed into the band pass filter and subsequently passed to the PLL which determines the frequency shift. Input quantities (User) such as the amplitude set point and resonant frequency are denoted using light blue.

and has a hardware band pass filter in order to cut off undesirable noise. The filtered signal is then fed to the phase-lock loop (PLL) controller to determine the frequency shift ($\triangle f$) by comparing the phase of the detected signal with the phase of the reference signal. The $\triangle f$ serves as the main imaging signal for FM-AFM. The sensor oscillation is maintained by using a feedback loop which is established through automatic gain control. It keeps the vibration amplitude at a constant level set by the user.

1.2.2 Theory of FM-AFM

The force sensor (see Fig. 1.5 a) can be treated as a harmonic oscillator[56]. We can describe it as an externally driven, damped harmonic oscillator. The interaction of the force sensor with a sample can be effectively described with the simple mass-spring system (see Fig. 1.5 b)[56]. We can view it as a mass (m) on the spring (k) which is externally excited with the force $F_d = F_0 \cos(\omega_e t)$ (see Fig. 1.5 b). The tuning fork has an intrinsic damping factor (γ) as a result of friction: to account for that we introduce to the model the resistive force $F_r = -b\nu$ where b is the constant. The equation of motion for the position $x(t)$ is:

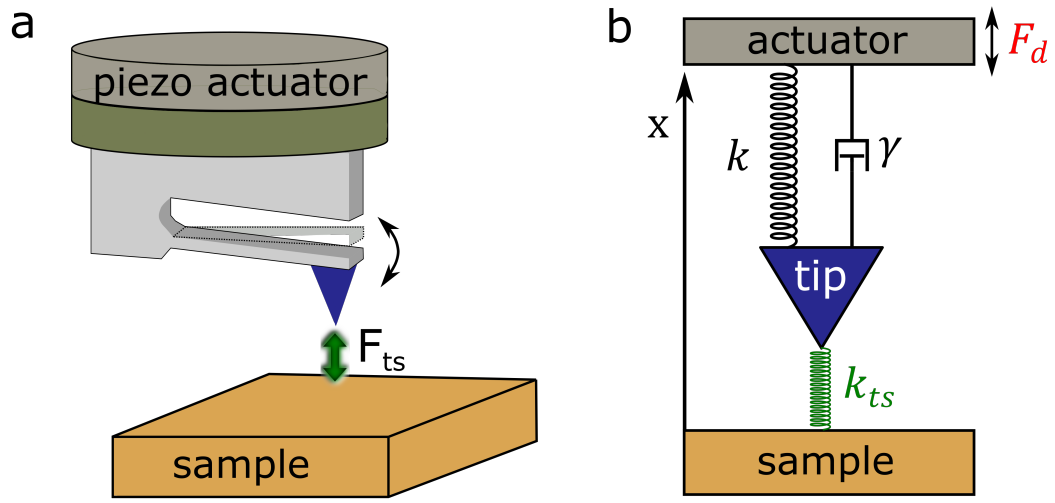

Figure 1.5: Model of the sensor under the influence of tip sample interaction. (a) 3D model of the oscillating qPlus sensor under the influence of the force gradient. (b) One-dimensional representation of the force sensor by a mass m on a spring with spring constant k and damping factor γ.

$$\ddot{x} + \gamma\dot{x} + \omega_0^2 x = \frac{F_0}{m}\cos(\omega_e t) \tag{1.13}$$

Where $\omega_0 = 2\pi f_0 = \sqrt{\frac{k_0}{m}}$ is the resonant frequency, and $\gamma = \frac{b}{m}$ is a damping factor. The steady state solution ($t \gg \frac{1}{\gamma}$) for the force oscillator is then:

$$x(t) = A_0\cos(\omega_d t - \delta) \tag{1.14}$$

Where the amplitude (A_0) of the steady state solution is given by

$$A_0 = \frac{\frac{F_0}{m}}{\sqrt{(\omega_0^2 - \omega_d^2)^2 + \left(\frac{\omega_0\omega_d}{Q}\right)^2}} \tag{1.15}$$

The expression for the phase (δ) of oscillation reads as follows:

$$\tan(\delta) = \frac{-\omega_0 - \omega_d}{Q(\omega_0^2 - \omega_d^2)} \tag{1.16}$$

When ($\omega_0 = \omega_d$) the amplitude becomes very large and resonance occurs. The phase shift (δ) at resonance is equal to $\pi/2$. The Q -factor is a dimensionless parameter which can be defined as the oscillation efficiency. The Q -factor represents the ratio between total energy stored in the excited oscillator to the energy dissipated per oscillation cycle. When driven at a frequency close to resonance frequency the Q -factor can be calculated as:

$$Q = \frac{\omega_0}{2\gamma} \tag{1.17}$$

From Eq. 1.15 we can predict that if an oscillation frequency goes out of resonance ($\omega_d \to 0$ or $\omega_d \to \infty$) the amplitude will attenuate. Therefore, it is useful to define the width of the resonance curve ($\triangle\omega$) at half amplitude height:

$$\triangle\omega = \frac{\omega_0}{Q}. \tag{1.18}$$

Thus, the higher the Q-factor of the oscillation system the narrower the resonance peak. The Q-factor determines the FM-AFM feedback as well as the signal to noise ratio. Higher Q factors can significantly enhance the force sensitivity[61]

For precise calculation (measurement) of Q and ω_0 for the corresponding oscillation system (force sensor), the following procedure is used: we retract the sensor far away from the surface (where interatomic forces cannot influence the oscillation cycle) and measure the frequency dependent response at constant excitation. By fitting the resulting peak response function, we can determine Q and ω_0.

We can analyze the influence of tip-sample interaction forces (F_{ts}) of the sensor by considering a simple externally driven damped harmonic oscillator under the influence of the interatomic forces. In the small amplitude limit, we can consider the tip-sample force as a slowly varying function of the actual tip position:

$$F_{ts}(x) = F_0 + \frac{\partial F_{ts}}{\partial x}\Big|_{x=0} x + ... \tag{1.19}$$

This approximation allows us to represent the tip sample interaction as a simple spring with stiffness k_{ts} ($k_{ts} \ll k$) as shown in Fig. 1.5, which is proportional to the force gradient:

$$k_{ts} = \frac{\partial F_{ts}}{\partial x}\Big|_{x=0} \tag{1.20}$$

In the presence of a force, the equation of motion is:

$$\ddot{x} + \gamma\dot{x} + \omega_0^2 x = \frac{F_0}{m}\cos(\omega_e t) + \frac{F_{ts}}{m} \tag{1.21}$$

By approaching the sensor towards the sample, the interatomic force will come into play which will eventually generate a shift of the equilibrium position (x_0) of sensor oscillation. In the small amplitude approximation, we can substitute $x(t)$ with $y(t) = x(t) - x_0$ in Eq. 1.20 which results in the following:

$$\ddot{y} + \gamma\dot{y} + \omega_0^{'2} y = \frac{F_0}{m}\cos(\omega_e t) \tag{1.22}$$

Where $\omega_0^{'}$ is the new resonance frequency caused by the influence of the tip

sample interaction:

$$\omega_0^{'} = \sqrt{\frac{k+k_{ts}}{m}} = \sqrt{\frac{k}{m}\left(1+\frac{k_{ts}}{k}\right)} = \omega_0\sqrt{1+\frac{k_{ts}}{k}} \tag{1.23}$$

Where m is the effective mass and $k + k_{ts}$ is the effective spring constant of the system. With a further approximation $|k_{ts}| \ll k$ and a Taylor expansion ($\sqrt{1+x} = 1 + \frac{1}{2}x$) the new resonant frequency of the force sensor can be written as:

$$\omega_0^{'} \approx \omega_0\left(1+\frac{k_{ts}}{2k}\right) \tag{1.24}$$

Consequently, the frequency shift results in:

$$\triangle\omega = \omega_0^{'} - \omega_0 = \omega_0\frac{k_{ts}}{2k} = -\frac{\omega_0}{2k}\frac{\partial F_{ts}}{\partial x} \tag{1.25}$$

The simple division of the resulting frequency shift by a factor of 2π, yields:

$$\boxed{\triangle f = \frac{\omega_0^{'} - \omega_0}{2\pi} = f_0\frac{k_{ts}}{2k} = -\frac{f_0}{2k}\frac{\partial F_{ts}}{\partial x}} \tag{1.26}$$

This result corresponds to the experimentally observed frequency shift ($\triangle f$). Thus, the frequency shift caused by tip-sample interaction is proportional to the negative force gradient, *if the following approximations are applied*: (a) the force gradient can be linearly approximated and (b) the force gradient is significantly smaller in comparison to the spring constant of the tip (k)[63]

However, in the case of a large oscillation amplitude, the equation for the frequency shift has a more general expression[56]. The tip-sample interaction is strongly dependent on the scale of the amplitude. In the large amplitude limit, the tip spends most of its time at the extrema of its motion cycle, and as a result, the biggest contribution to the frequency comes from the lower turnaround point where the tip is influenced by the force gradient. The equation for the frequency shift in the large amplitude limit is as follows:

$$\triangle f = -\frac{f_0}{\pi k A^2}\int_{-A}^{A} F_{ts}(d+x)\frac{x}{\sqrt{A^2-x^2}}dx = -\frac{f_0}{\pi k A^2}\int_{-A}^{A} F_{ts}(d+x)g(x)dx \tag{1.27}$$

In the presence of dissipative tip-sample interactions, the force at particular points may vary upon approach or retraction of the tip. Therefore, the tip-sample force in Eq. 1.27 should be $F_{ts} = F_{ts,approach} + F_{ts,retract}/2$[64;65].

However, the physical description of the system is given by force rather than frequency shift. There are two common methods to recover the force from the measured frequency: the matrix method[66] or the Sader - Jarvis method[67].

1.2.3 Interatomic forces in FM-AFM

The tip-sample interaction force measured with FM-AFM consists of the various force contributions which mainly originate from electrostatic interaction which contains several long- and short-range components. The separation of the different force components is not a trivial task and requires the fulfilment of special conditions[68]. Next, we discuss in detail the long- and short-range contribution to the total tip-sample interaction force.

Long-range contributions are mainly due to van der Waals (vdW) forces and electrostatic (ES) forces. The vdW forces occur mainly from instantly formed dipole moments as a result of the electron density fluctuation around atoms. The vdW forces can be described as a sum of the temporary dipole-dipole interaction between molecules or atoms[56]. As a result of the long-range nature of vdW forces, not only the front atom of the tip apex but also from the neighbouring atoms contribute to the observable vdW interaction. Thus, the interaction energy between the elementary volume of the tip dV_t and elementary volume of the sample dV_s can be written as:

$$dU_{vdW} = -\frac{C\rho_t\rho_s}{|r_t - r_s|^6} dV_t dV_s \tag{1.28}$$

where ρ_t is a density of the atoms of the tip, ρ_s is a density of the atoms of the sample, C is a coefficient in atom-atom pair potential and r_t, r_s are the position of the tip and the sample. We can approximate the tip as a paraboloid with local radius R and sample surface as a semi-infinite solid[56 57]. The vdW interaction energy and force between the tip and sample are:

$$U_{vdW} = -\frac{HR}{6x} \tag{1.29}$$

$$F_{vdW} = -\frac{HR}{6x^2} \tag{1.30}$$

where $H = \pi^2 C\rho_t\rho_s$ is the Hamaker constant, an intrinsic property of the material (metal is typically 2-3 eV[57]) and x is the tip sample distance. It is evident from Eq. 1.29 that a sharper tip (smaller radius) can significantly reduce the influence of the vdW forces.

The long-range electrostatic (ES) force originates mainly from inhomogeneity of the charge distribution. On the macroscopic scale a conductive tip and conductive sample can be approximated as a parallel plane capacitor, with a capacitance $C(x)$. The resulting electrostatic force will be:

$$F_{el} = \frac{1}{2}\frac{\partial C}{\partial x}(V - V_{CPD})^2 \tag{1.31}$$

where V_{CPD} is a contact potential difference (CPD) and V is the applied bias

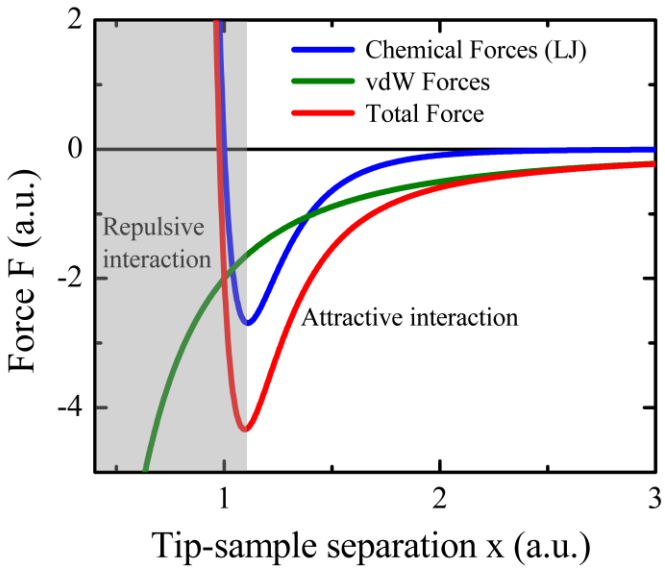

Figure 1.6: Forces which act between tip and sample.

voltage. The ES force has a parabolic dependence on the applied bias voltage ($F_{el} \propto V^2$). The ES force can be minimized by adjusting the bias voltage to the negative contact potential difference ($V = V_{CPD}$). The contact potential difference can be measured via Kelvin Probe Force Microscopy (KPFM)[69] which is based on non-contact AFM.

Short-range Chemical Bonding (CB) forces have a small range and become dominant in the close tip-sample distances when the electron wave functions of the tip and the sample start to overlap. CB can be both attractive and repulsive, depending on the tip-sample separations. The repulsive interaction occurs mainly from ion core repulsion which occurs due to the Pauli exclusion principle which states that only two electrons can occupy the same quantum state simultaneously.

The simplest way to model the CB forces is the famous Lennard-Jones (LJ) potential which partially describes the dispersion forces[70]:

$$U_{LJ} = U_0 \left[\left(\frac{x_0}{x} \right)^{12} - 2 \left(\frac{x_0}{x} \right)^{6} \right] \tag{1.32}$$

where U_0 is the bonding energy at the equilibrium distance x_0. The resulting force due to the LJ potential Eq. 1.32 will be:

$$F_{LJ} = \frac{12U_0}{x_0} \left[\left(\frac{x_0}{x} \right)^{13} - 2 \left(\frac{x_0}{x} \right)^{7} \right] \tag{1.33}$$

The distance dependence for the all these force contributions are illustrated in Fig. 1.6.

2. Main objectives of this thesis

The main aim of the thesis **"Study of molecular structures on solid state surfaces"** is to gain more insight into new nanostructures which can be used for molecular electronics applications. In this thesis, a combination of Variable Temperature STM and Low Temperature STM/AFM was used to study different molecular structures on Au(111) surface with atomic resolution in UHV conditions. The scanning probe techniques allows to visualize the internal structure of single molecule and access molecular electronic and conformational properties. All our results are supported with state of the art DFT calculations.

The main objectives of the thesis can be summarized as follow:

- Investigations of the physicochemical properties of fullerene-based nanostructures on Au(111) at room temperature. These structures were formed by soft Ar^+ ion bombardment of self-assembled fullerene islands.
- Functionalization of the Au tip apex with the single nitrous oxide molecule to provide further inside regarding the origin of sub-molecular resolution in AFM. We evaluate its high-resolution imaging and spectroscopic capabilities using FePc molecules.
- On-surface synthesis of anthracene-based π-conjugated polymers on the Au(111) surface. The synthesized polymers were characterized using high-resolution AFM imaging with CO functionalized tip.

3. Experimental setups

The results presented in this thesis were performed in UHV conditions to enable the preparation of well-defined surfaces and avoid sample contamination[71]. The STM measurements presented in section 3.1.3 (Paper I) were obtained using a modified commercial UHV (5×10^{-10} mbar) variable temperature STM/AFM (VT-STM/AFM) manufactured by Omicron GmbH[72]. The STM/AFM measurements presented in sections 3.2.2 (Paper II) and 3.3.2 (Paper III) were carried out using a UHV LT microscope. The microscope is commercially available from Createc[73] and equipped with a qPlus sensor[26]. The microscope is mechanically connected to the bottom of the liquid helium cryostat to allow LT operation (5 K). This section is devoted to a basic overview of the experimental tools.

3.1 Brief description of the STM/AFM systems

3.1.1 VT-STM/AFM

The VT-AFM/STM was developed in 2008 by Omicron. Figure (3.1 a) shows a photo of the system which was used during this PhD thesis. The whole setup consists of one UHV chamber where all STM measurements and sample preparations are performed with a base pressure below 5×10^{-10} mbar. To achieve and maintain UHV conditions we use a turbo molecular pump backed by a rotary pump, as well as an ion pump combined with a titanium sublimation pump.

For safe sample transfer from the ambient atmosphere to UHV, a small load lock chamber is used. The load-lock chamber is connected to the chamber through a gate valve and has its own high vacuum pumping system combined with capacity to vent to atmospheric pressure with dry nitrogen gas. The load lock has two magnetic transfer arms which allow safe sample transfer to the prep chamber without breaking vacuum.

The 3-axis manipulator within the chamber is equipped with one stage for annealing treatment by resistive and direct current heating. Additionally, the chamber is equipped with low-energy electron diffraction (LEED), a quadrupole mass spectrometer (QMS), and an ion gun. Transfer of the sample is accomplished with a pincer-grip wobble stick. The wobble stick allows a quick and reliable sample interchange between the main system manipulator, as well as the sample/tip storage carousel. The sample/tip storage carousel can house up to 12 samples/tips. The chamber has additional viewports for optimal observation of the tip/sample coarse positioning using an externally mounted CCD camera. The chamber has two additional ports for in-situ evaporation. The tunnel gap is very sensitive to mechanical vibrations. To suppress them, the microscope is

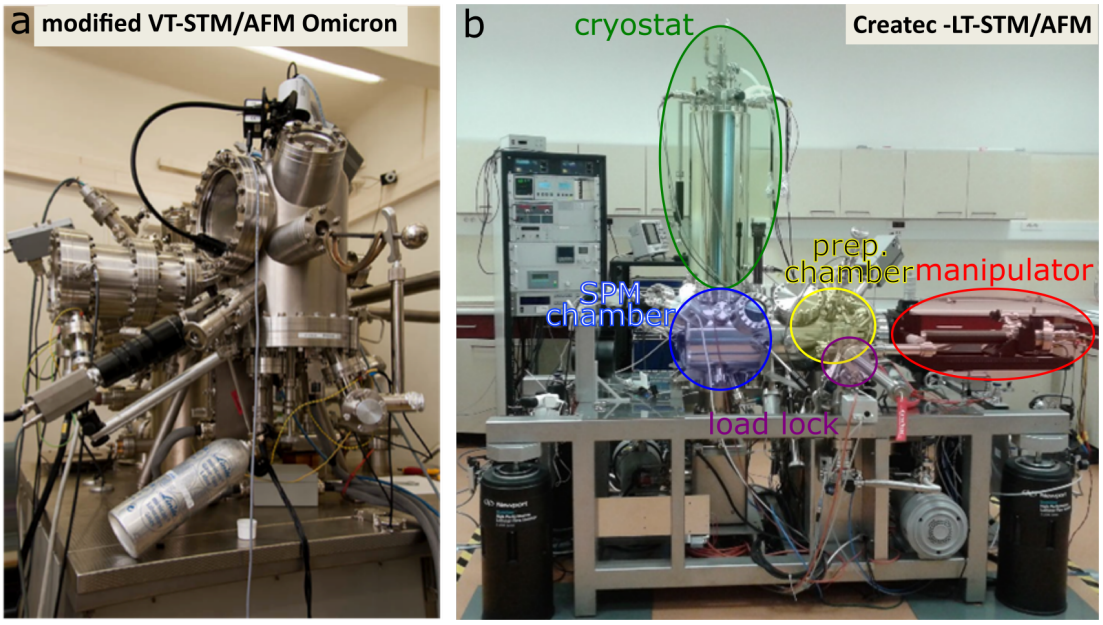

Figure 3.1: Experimental setups. (a) Photo of modified VT-STM/AFM Omicron system. (b) Photo of Createc LT STM/AFM system.

equipped with an eddy current damping mechanism and springs[56].

To perform reliable tunneling current measurement the microscope is equipped with an analogue pre-amplifier, intended to provide the highest possible signal to noise ratios. The pre-amplifier allows stable STM operation with currents as low as 50 pA at room temperature. The process of operating the microscope (lateral/ vertical modulation of the tip/sample relative position) is controlled through the Omicron Matrix user interface[72].

3.1.2 LT-STM/AFM

The Createc LT-STM/AFM microscope is based on the design initially developed by Gerhard Meyer[74]. The whole setup consists of the following components: SPM chamber with bath cryostat, preparation chamber with manipulator, and load-lock chamber for transfer from ambient to UHV (see Fig. 3.1 b). All three chambers are separated with gate valves and have separate pumping systems. Both SPM and preparation chamber have similar pumping systems, based on ion getter pumps (IGP) with integrated titanium sublimation pumps (TSP).

The load-lock is connected to the preparation chamber and has two magnetically coupled linear motion arms for sample transfer, as well as a storage carousel for samples and sensors. The load-lock has a separate pumping system (scroll and turbo molecular pump (TMP)) which can pump from ambient conditions down to 10^{-8} mbar. For sample preparation and transfer between the preparation and microscope chambers, a 3-axis manipulator is mounted on the preparation chamber with infinite rotation about the long axis of motion. The manipulator has

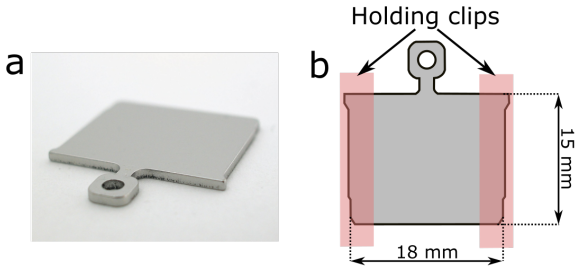

Figure 3.2: Flag style sample holder (a) photo of the sample plate. (b) specification and dimensions of the sample holder

multiple different sample slots which allow for direct current and e-beam heating.

The main feature of the current system is an LT bath cryostat which allows sample cooling up to 5 K. The cryostat consists of two tanks containing liquid nitrogen and helium. The helium tank is located in the center and surrounded by nitrogen tank. Both tanks have evaporation shields ($\approx$ 30 K) and are covered with the outer wall. The nitrogen tank has vacuum separation from the outer wall.

The SPM head is mounted directly under the cryostat and suspended by four springs for vibration isolation. Additionally, the entire microscope frame is placed on four pneumatic legs to decouple the system from the mechanical vibrations of the building. Detailed description of the SPM head design and cryostat is provided by the manufacturer[73].

The microscope is controlled with Nanonis SPM control system manufactured by Specs Zurich. The ease of use and versatility of experiments that can be performed makes this one of the most prevalent pieces of control hardware in the scanning probe community.

3.2 Sample Preparation

Au(111) single crystal (Mateck) was used in all experiments presented in this thesis. The Au(111) surface was chosen due to its chemical inertness which leads to weak molecular adsorption primarily through van der Waals interactions[75]. High-quality large terraces can be easily created through standard cleaning procedures. The gold sample was mounted on a flag style molybdenum or tantalum sample holder which allowed resistive heating in the UHV environment (Fig. 3.2).

The surface was cleaned by the standard procedure of Ar^+ sputtering (1 keV) and subsequent high-temperature annealing to 600° C. The sputtering and annealing process needs to be repeated for a few cycles until a clean surface with the herringbone reconstruction can be observed by STM. Typically, three Ar^+ sputtering and annealing cycles (5 minutes each) were required to obtain samples

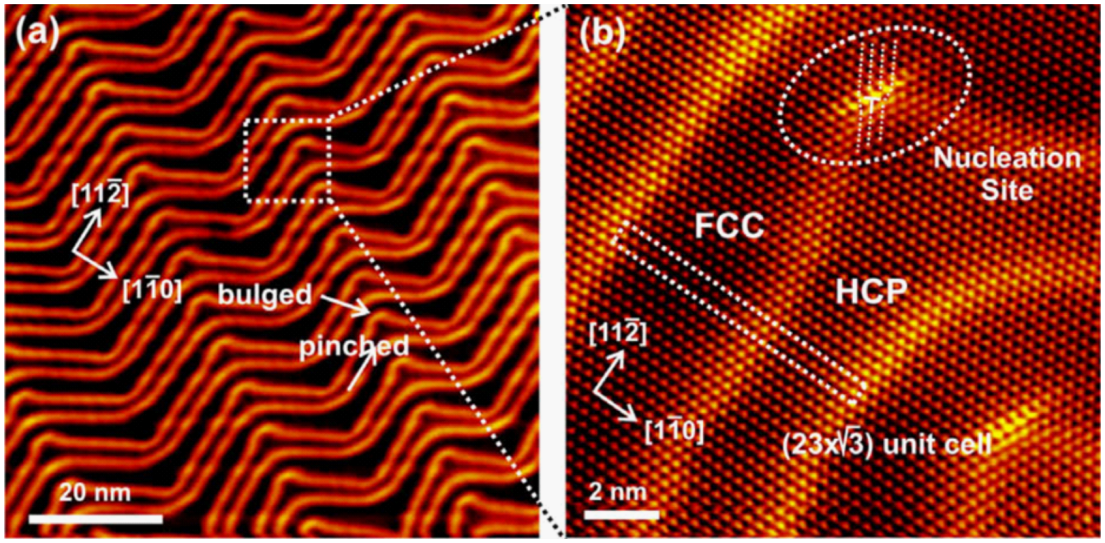

Figure 3.3: STM images of a gold substrate (a) Large scale STM image of the Au (111) herringbone reconstruction after the cleaning procedure in UHV. (b) Detailed STM image of the Au(111) surface showing atomic resolution. The characterized surface unit cell is indicated with the white rectangle. The bulged elbow site is indicted with the white circle. Images taken from F. Besenbacher, et. al[76]

with overall cleanliness suitable for achieving atomic resolution with STM. A typical large-scale STM image of the clean Au(111) surface is depicted in Fig. (3.3 a). The image reveals a well-known characteristic herringbone reconstruction.

Au(111) has a unique surface reconstruction denoted as $Au(111) - 22 \times \sqrt{3}$. This reconstruction is characterized by paired rows which form a so-called herringbone pattern (Fig. 3.3 a). The bright lines are transition areas between face-centered (FCC) and hexagonal close-packed (HCP) atoms stacking. Notably, both areas are not equally represented; the FCC region is larger than HCP[77]. The bending points of the lines are cooled elbow sites that can serve as nucleation centers[77]. There are two types of elbow sites: the pinched and bulged elbows. The characteristic Au(111) reconstruction occurs due to uniaxial compression of the surface layer along a [1$\bar{1}$0]-crystallographic direction and as a result the surface contains more atoms than a comparable cross-section of the bulk crystal[78]. The interatomic distance between two neighbouring Au atoms is a = 2.88 Å. The (111) surfaces of Nobel metals (Au, Cu, Ag) generally possess a electronic surface state, which can be probed with scanning tunnelling spectroscopy (STS). The surface state of Au(111) measured with STS can be approximated as a step function with the band minimum at 450 mV relative to the Fermi level[77].

3.3 Tip preparation

The core element of both STM and AFM is a scanning probe which has a major impact on the quality of the measured data. The shape and chemical composition (cleanliness) are the main factors determining the performance of a scanning probe. Tips used in a UHV environment are commonly made of tungsten (W) or platinum-iridium (Pt-Ir) alloys. These materials have a high melting temperature and substantial mechanical strength.

STM tips were fabricated using a "drop-off" electrochemical etching technique[79;80]. A piece of tungsten wire (0.5 mm diameter) was mounted to a STM tip holder commercially available from Omicron[72]. The tip holder then was magnetically held to the etching station to ensure precise vertical movement of the tip. The apex of the wire is placed through the center of a metallic ring, which has been immersed in a 2.5 M NaOH solution. A bias voltage (about 10 V) is then applied between the ring and the W wire. For an optimized etching procedure, the tip and the counter electrode are connected using an electronic control circuit[80] to ensure a smooth cutoff of power just as the tip wire is etched through. The resulting tip is then cleaned in alcohol and distilled water to remove residuals. The tip is left to dry out for a couple of minutes whereupon it is ready to be loaded in a UHV system.

For AFM measurements, we used the qPlus sensor[26] commercially available from Createc. The qPlus sensors first need to be cut or etched to obtain the desired length of the wire. The tips of a cut sensors (see Fig. 3.4 a) are then sharpened and shortened by a Xenon plasma focused ion beam (P-FIB) (see Fig. 3.4 b,c). To lower the harm from ion beam on the probe, the position for the final cut is determined solely using electron beam imaging. The probe was kept in a home-made holder grounded to prevent charging. The process was performed in the sofmat laboratory[81]. Pt-Ir alloys are relatively inert towards oxidation, therefore, the sensors after the cutting procedure can be introduced to the UHV environment and installed in the SPM head without additional cleaning.

3.3.1 In-situ tip preparation

STM tips and qPlus sensors require additional in-situ treatment to obtain an atomically sharp probe suitable for imaging and spectroscopy. The easiest way to modify the tip apex is to indent it (for several nm) into a metal substrate. If after several indentations the tip is still unstable, and the desired (known) surface reconstruction cannot be observed, the next step is to indent the tip deeper into the surface while simultaneously applying higher voltages ($\sim \pm 7$ V) and high currents (~ 50 nA). This can eventually improve the tip. If the tip has a large apex and cannot be sharpened by indentation or bias pulses one final option

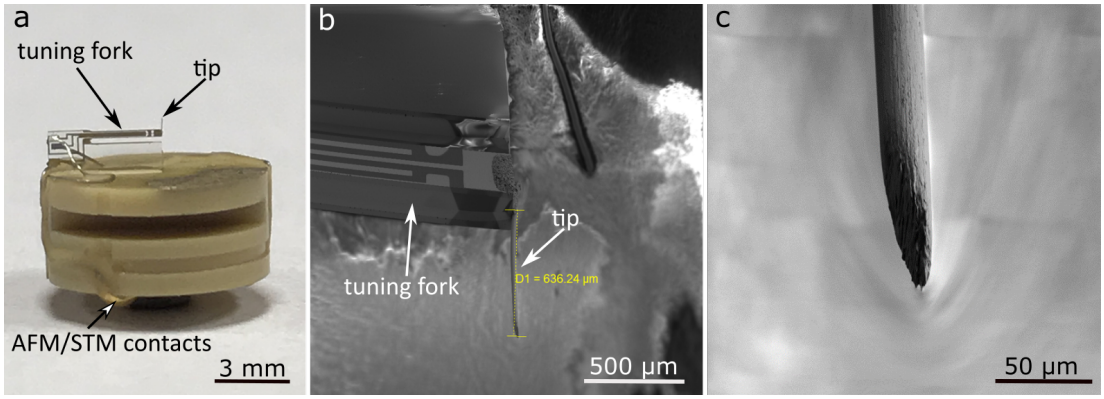

Figure 3.4: Process of qPlus sensor cutting. (a) Photo of the Createc compatible qPlus sensor after shortening the wire. (b) Scanning Electron Microscope (SEM) image of the tip after the FIB cut. (c) The tip apex upon completion of the sharpening procedure.

is to lower the current preamplifier gain to allow for micro-ampere currents to flow through the tip-sample junction during the indentation procedure. Currents above 10 uA and 20 V bias have enough power to destroy the conductive glue that holds the tip to the end of the qPlus.

However, in the case when a controlled tip crash is not helpful, one can apply additional in-situ treatment to W STM tips. The STM tips can be sputtered[82;83] and annealed[57;82;84] to remove the contamination (oxide) layer. Importantly, the annealing or sputtering cannot be applied to a qPlus sensor. The sputtering used for cleaning and sharpening uses energies of 0.5 to 4 keV and are usually done in the same way as for the sample sputtering. It is also possible to sharpen the tip by applying a high voltage (field emission technique).

3.3.2 Tip functionalization

To functionalize the metal tip apex with a single carbon monoxide molecule the prior tip treatment must be applied. First, the metal tip has to be mesoscopically sharp, and stable to lower the influence of long-range forces. One way to check the tip sharpness/mesoscopic shape is to measure the frequency shift value in the tunnelling regime: the smaller the frequency shift relative to the far-distance baseline, the sharper the tip. In some cases, a mesoscopically sharp tip requires additional treatment to obtain an atomically terminated tip apex.

After obtaining a sharp and stable metal tip, it can be used for functionalization with a carbon monoxide (CO) molecule. Usually, tip functionalization is done in three stages:

In the first stage, the molecule which will be used for functionalization has to be deposited (described in next section) and located via STM (see Fig. 3.5 a,d). Usually, the CO molecule can be detected in STM mode by scanning with

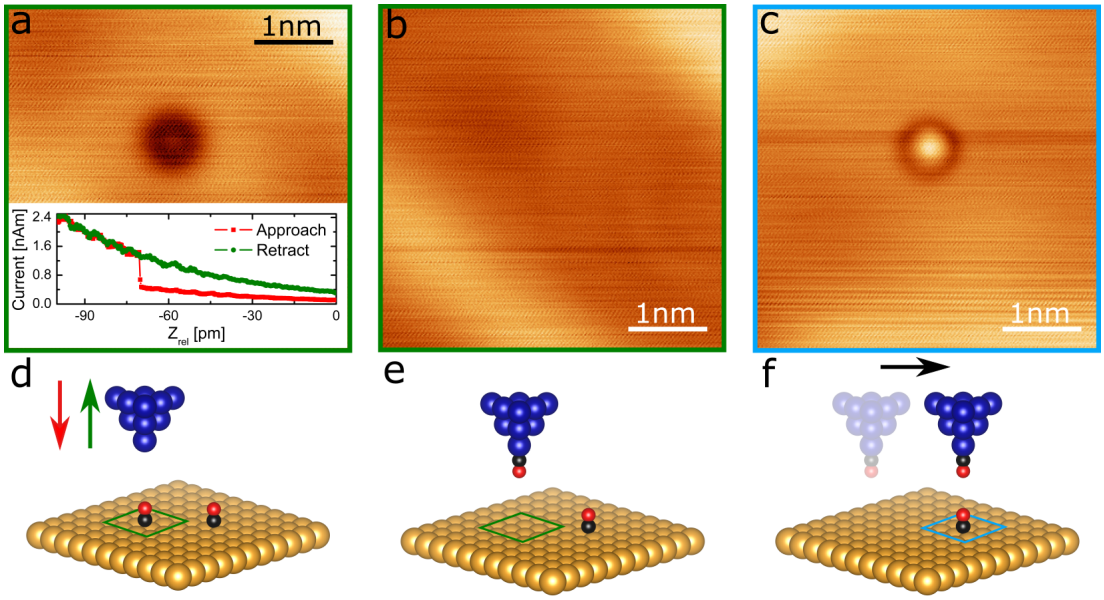

Figure 3.5: CO tip functionalization on Au(111). (a) STM image (U_b = 60 mV, I = 20 pA) of the single CO molecule with metal tip. (b) STM image (U_b = -60 mV, I = 20 pA) of the area in (a) after tip functionalization. (c) STM image (U_b = -60 mV, I = 20 pA) of a single CO molecule with CO decorated metal tip. (d,e,f) Illustrate the procedure of tip functionalization. The carbon atom on the 3D model colored in black and the oxygen atom is red.

relatively low bias (50-100 mV) and low current set point (I = 20 pA). The CO molecule on Au(111) surface imaged with a metallic tip appears in STM as a dark depression (see Fig. 3.5 a).

In the second stage, the metallic tip is positioned directly above the CO molecule. Then the feedback is switched off and the tip is continuously approached (10 pm steps) towards the molecule until a characteristic jump in the current occurs (inset of Fig. 3.5 a). After the jump, the tip is retracted and feedback is restored. By re-scanning the area (Fig. 3.5e,b), the lack of CO molecule on the surface is usually serves as indication of a successful tip functionalization.

In the third stage, the functionalized tip is used to locate and imaging an additional CO molecule on Au(111) (see Fig. 3.5 c,f). Then STM contrast of CO appears as a bright protrusion. The shape of the protrusion generally can serve as an indication of the quality of molecular adsorption on the tip apex. The symmetric protrusion with a rounded dark halo (see Fig. 3.5 c) indicates a perpendicular/symmetric CO adsorption (see Fig. 3.5 f). The CO molecule attaches to the tip apex via the carbon atom with the oxygen pointing towards the surface (see Fig. 3.5 f).

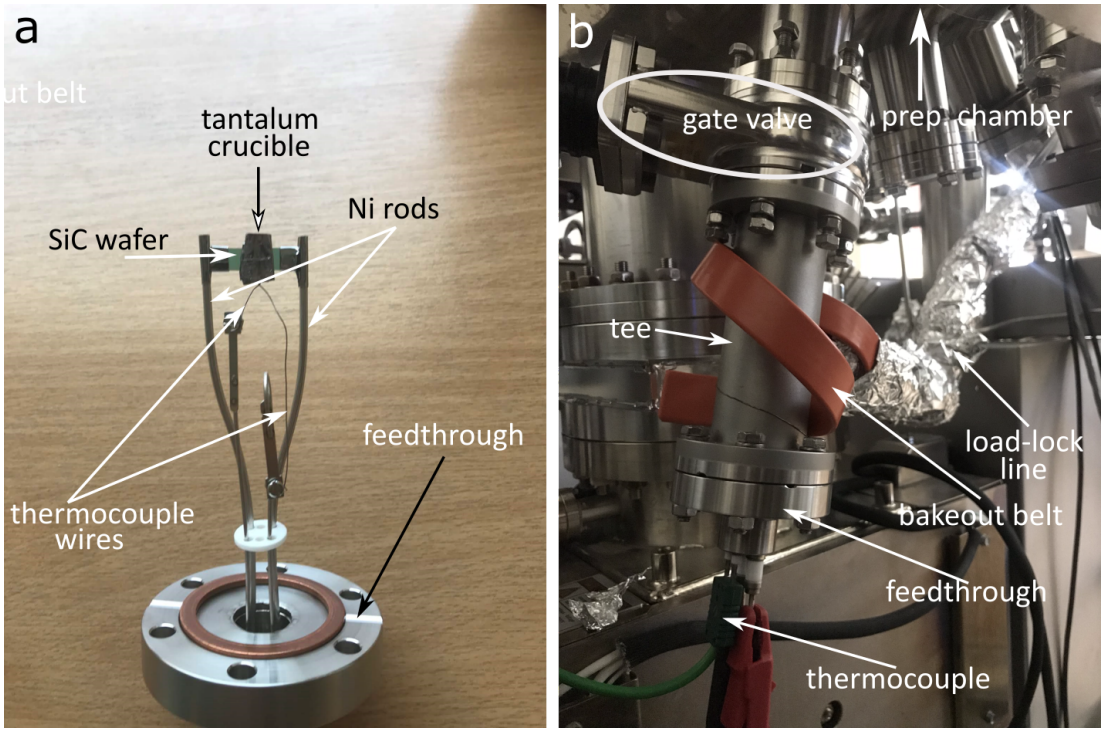

Figure 3.6: Evaporator. (a) Photo of the home-built molecular evaporator. (b) Photo of the home-built evaporator connected to the prep chamber.

3.4 Molecular deposition in UHV

To deposit molecular species on a clean metal surface, we employed a home-made thermal evaporation source (see Fig. 3.6). The evaporator has a pocket made of tantalum, suitable for the evaporation of molecules such as C_{60}, FePc (C32H16FeN8), and 4BrAn (11,11,12,12-tetrabromoanthraquinodimethane). The tantalum crucible is mechanically attached to a silicon carbide wafer slice which allows for resistive heating. To ensure precise temperature control, a K-type thermocouple is attached (spot welded) directly to the tantalum crucible.

Generally, before placing new molecules inside the tantalum crucible, it is cleaned with isopropanol and annealed in UHV environment up to 700° C to remove the residual material from previous evaporations. After the cleaning procedure is complete, molecules can be placed inside the crucible and the evaporator can be reinstalled on the prep chamber. The evaporator is installed to the preparation chamber through a tee which is separated from the prep chamber with a gate valve (see Fig. 3.6 b). Before the opening gate valve and connecting evaporator to preparation chamber, it's pumped with the load-lock pumping system for 12 hours with subsequent molecular degassing. Prior to each deposition, the molecular source was degassed for several minutes to remove contaminations (e.g., water and other non-desirable organic species). During deposition the sample was kept at room temperature.

C_{60} molecular deposition: For the C_{60} deposition the home-built evaporator (Fig. 3.6a) was used. After loading the evaporator with C_{60} molecules, it was connected line-of-sight to the sample surface stored inside the STM head. Prior to each deposition, the C_{60} source was preheated to 360° C and degassed (420° C) for 5 minutes to remove contamination. After this procedure the sample was transferred into the STM head for the deposition of molecules by heating the evaporation source at 420° C.

FePc molecular deposition: FePc molecules (Sigma Aldrich, evaporation temperature ca. 250° C) were thermally evaporated using a variant of the home-build evaporator (tantalum pocket mounted directly to the flag style sample holder (Fig. 3.2)). The tantalum pocket was loaded with molecules and placed on the manipulator which allows indirect heating. Before each deposition the molecules were degassed for 15 minutes. During deposition the sample was kept at room temperature.

4BrAn molecular deposition: The molecules were thermally evaporated using the home-build evaporator (Fig. 3.6). The 4BrAn molecules were loaded inside the tantalum pocket and after the evaporator was mounted to the preparation chamber. Before each molecular deposition, molecules were degassed for several minutes and deposited to the sample which was kept at room temperature.

CO, N_2O molecular deposition: In both cases, the gases were deposited while the Au(111) surface was at low temperature (< 12 K). The gas line was flushed (using load-lock pumping system) three times before the molecules were introduced directly to the SPM head through the leak valve for approximately 15 seconds.

4. Results

4.1 Formation of stable Au–C bonds for fullerene-based nanostructures on Au(111) surface at RT

Molecular self-assembly on surfaces has attracted a great deal of attention during the past decade, because of its potential in molecular electronic device fabrication[85–89]. The coupling of molecules to metal surfaces determines their electronic properties[90]. Understanding of their electronic properties is the first step towards designing functional electronic devices. Fullerenes on metal surfaces are among the most extensively studied systems[91–98] . Due to their practical properties, fullerenes are a key topic of contemporary nanotechnology and industrial research. This chapter presents a detailed study of a new type of system: fullerenes with artificially created defects, which bind to a Au(111) surface via covalent bonds. The formation of the covalent bonds enhances the conductivity and stability[99;100].

4.1.1 Basic properties of fullerene molecules

Fullerenes were discovered by Kroto and Smalley in 1985[101], which helped them win the Nobel Prize in 1996. C_{60} is a remarkably stable molecule with a truncated icosahedron structure consisting of 60 carbon atoms arranged as 12 pentagons and 20 hexagons (see Fig. 4.1 a)[102]. The carbon atoms are all interconnected predominantly through an sp^2 bonding configuration. However, the actual bonding of C_{60} is more complex due to the cage structure of the molecule. The environment of each carbon is curved (non-planar) which causes partial re-hybridization and leads to sp^3 bonding configuration. A single C_{60} molecule has 90 covalent bonds between carbon atoms: 60 single bonds and 30 double bonds. The hexagons and pentagons are connected through single bonds (C-C bond) which have a bond length of around 1.46 Å and are thus considered as electron-poor areas. The two hexagons are connected through double bonds (1.40 Å) and referred to as electron rich areas[103]. The diameter of a single C_{60} molecule is about 7.1 Å by adding the width of the π electron cloud around the molecule the total radius of the molecule enlarge up to 1 nm.

Electronic properties of the C_{60} molecule have been intensively studied using both experimental[105–107] and theoretical methods[108–110]. The electronic properties of a single C_{60} molecule are mostly determined by the delocalized π electrons[102]. The C_{60} molecule has a fivefold degenerate highest occupied molecular orbital (HOMO) and a threefold lowest unoccupied molecular orbital (LUMO).

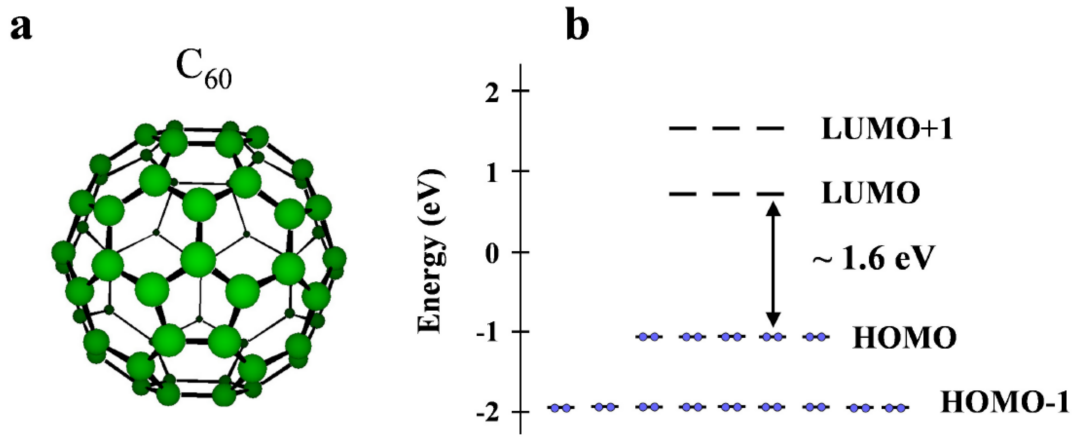

Figure 4.1: (a) Ball stick model of a single C_{60} molecule. (a) Energy level of a single C_{60} molecule. Images taken from R. Yamachika[104].

The HOMO energy level is completely filled with 10 electrons, while the LUMO could host 6 electrons. The energy gap between HOMO and LUMO levels is around 1.6 eV (see Fig. 4.1 b). However the HOMO to LUMO transition is forbidden which makes pure C_{60} an insulator[102].

4.1.2 C_{60} molecules on a Au(111) substrate

The clean Au(111) surface has a unique herringbone reconstruction with a unit cell $22 \times \sqrt{3}$ (see Fig. 3.3) and is considered to be a standard substrate for the study of molecular self-assembly[111]. The Au(111) substrate is relatively inert and easy to clean in a UHV environment. In the initial step of the experiment, we observe that almost all the C_{60} molecules are adsorbed at the terrace edges of the atomic steps. Molecules are assembled into one-dimensional islands or short chains along the step edges. This might be attributed to the existence of increased local reactivity of the step edges and high mobility of the C_{60} molecules on the surface at room temperature.

The covalently bonded spherical shape of C_{60} molecule leads to hexagonal compact self-assembly on low interacting metal substrates. After adsorption of fullerenes on Au(111) two distinct types of molecules can be discriminated, namely "dim" and "bright" molecules. The apparent height difference between dim and bright C_{60} molecules is clearly visible in cross-sectional profiles[94]. The "dim" molecule can be attributed to absorption above a single-atom vacancy (hex-vac) while "bright" molecules adsorb on top positions of the Au(111) surface[113]. The structure of a single C_{60} molecule can be observed using LT-STM. Three distinguishable molecular patterns have been observed (see Fig. 4.2) which can be attributed to the three different molecular orientations[96].

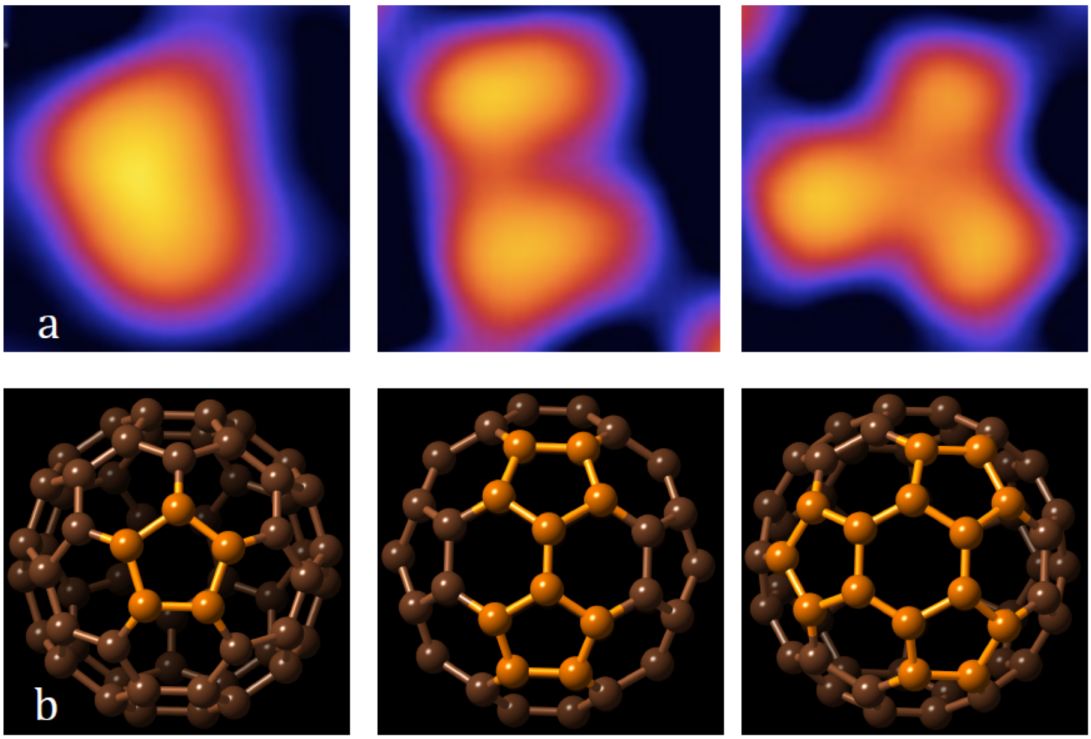

Figure 4.2: Adsorption configuration of the C_{60} molecule on Au(111). (b) Corresponding ball-stick models. Image taken from Y. Xie[112].

4.1.3 STM study of activated Au–C coupling

Our motivation for Ar^+ bombarding was to introduce atomic defects into C_{60} molecules. In this context the term defected C_{60} refers to fullerenes that have lost one (or more) C atoms after Ar^+ bombardment and saturate their newly-acquired dangling bonds through intramolecular rearrangement.

In the following study (see Paper I on page 31) we deposited C_{60} on Au(111) substrate. The molecule formed self-assembled 2D islands. Next we used Ar^+ ions sputtering to successfully remove carbon atoms from the C_{60} molecules. Defects inside the C_{60} islands formed by sputtering were distinguished and characterized by STM. We observed a single molecules detached from the islands as the result of the sputtering process. These functionalized molecules stabilized at the kinks in the herringbone reconstruction of the substrate.

Density Functional Theory (DFT) calculations reveal the character of the electronic structure at the interface. The unsaturated C atoms formed by Ar^+ sputtering react with the Au surface. Different binding geometries are studied, and their electronic properties are calculated.

My contribution was experimental STM measurements and sample preparation. I carried out data acquisition at room temperature and identified single bright dots on the surface that correspond to single C_{59} molecules which were disjointed from islands during the sputtering process. These molecules occupy

the elbow sites of the herringbone reconstruction which possess increased reactivity. I analyzed and prepared the experimental data for the publication and actively participated in the composition of the manuscript.

BEILSTEIN JOURNAL OF NANOTECHNOLOGY

Stable Au–C bonds to the substrate for fullerene-based nanostructures

Taras Chutora[1,2], Jesús Redondo[1], Bruno de la Torre[1], Martin Švec[1], Pavel Jelínek[*1] and Héctor Vázquez[*1]

Full Research Paper

Open Access

Address:
[1]Institute of Physics, Academy of Sciences of the Czech Republic, Cukrovarnicka 10, Prague, Czech Republic and [2]Palacký University, RCPTM, Joint Laboratory of Optics, 17. listopadu 12, Olomouc, Czech Republic

Email:
Pavel Jelínek[*] - jelinekp@fzu.cz; Héctor Vázquez[*] - vazquez@fzu.cz

* Corresponding author

Keywords:
Au–C bonds; density functional theory (DFT); fullerenes; scanning tunneling microscopy (STM); sputtering

Beilstein J. Nanotechnol. **2017,** *8,* 1073–1079.
doi:10.3762/bjnano.8.109

Received: 15 February 2017
Accepted: 26 April 2017
Published: 17 May 2017

This article is part of the Thematic Series "Towards molecular spintronics".

Guest Editor: G. Salvan

Abstract

We report on the formation of fullerene-derived nanostructures on Au(111) at room temperature and under UHV conditions. After low-energy ion sputtering of fullerene films deposited on Au(111), bright spots appear at the herringbone corner sites when measured using a scanning tunneling microscope. These features are stable at room temperature against diffusion on the surface. We carry out DFT calculations of fullerene molecules having one missing carbon atom to simulate the vacancies in the molecules resulting from the sputtering process. These modified fullerenes have an adsorption energy on the Au(111) surface that is 1.6 eV higher than that of C_{60} molecules. This increased binding energy arises from the saturation by the Au surface of the bonds around the molecular vacancy defect. We therefore interpret the observed features as adsorbed fullerene-derived molecules with C vacancies. This provides a pathway for the formation of fullerene-based nanostructures on Au at room temperature.

Introduction

In single-molecule electronics, the active element in an electronic circuit is a small molecule connected to two nanoelectrodes, and molecular chemical properties determine the characteristics of current flow. The reliable preparation and characterization of such nanostructures has been made possible by state-of-the-art scanning probe methods with which individual atoms and molecules can be manipulated. In parallel, the use of atomistic simulations, mainly based on density functional theory (DFT), has allowed for a detailed understanding of the basic mechanisms that determine the electronic and nanoscale transport properties [1]. For spintronics, small organic molecules are appealing since they feature weak spin–orbit interaction and long spin lifetimes [2,3].

The large pool of organic molecules opens the possibility of almost unlimited functionalities given the right molecular

design [4]. Fullerenes are particularly well-studied molecules. Since their discovery in 1985 [5], fullerenes have played an important role in molecular surface science, organic photovoltaics and single-molecule electronics. Fullerenes can be deposited on a series of metallic and semiconducting substrates [6-8]. In molecular transport, they have been used both as target molecules as well as anchoring groups [9-12]. They have featured in spin transport studies, where spin currents can be achieved by encapsulating magnetic atoms or impurities inside the fullerene cage [13-18]. The adsorption of C_{60} on the metal surface determines the strength and spread of electronic coupling and conductance values [9-12]. For an archetypal electrode material in single molecule transport studies such as Au, however, their high mobility at room temperature can lead to a large spread in conductance or to problems in trapping the molecule at the interface [19,20]. It might therefore be desirable to achieve strong metal–molecule bonds that result are electronically transparent or exhibit a well-defined conductance. Au–C metal–molecule bonds were found to be highly conducting [21,22].

Here we report on the formation of stable fullerene-based nanostructures on Au(111) at room temperature in ultra-high vacuum (UHV) environment. These structures were realized by soft sputtering of fullerene films on the surface with Ar^+ ions and were studied using scanning tunneling microscopy (STM). After sputtering, bright spots on the herringbone corners are observed, which we show to be adsorbed fullerenes with defects created by the sputtering process. The sputtering process is expected to result in the formation of vacancies in the fullerene molecules, where C atoms are knocked out. A series of fullerene fragments can be formed in the collision with high-energy atoms and ions. In our work, we gradually increased the energy of the incident ions starting from a low value until changes in the film morphology (in particular the spots on the herringbone elbows) were observed. We therefore hypothesize that the damaged fullerenes in our study are C_{59} molecules, an assumption discussed below. C_{59} molecules have the highest energetic stability (difference between the cluster energy and the sum of the energy of the individual C atoms) after C_{60} [23-25]. These findings are corroborated by total-energy DFT simulations.

Since the diffusion of fullerenes on Au is very fast at room temperature, individual molecules cannot be stabilized and contacted outside islands. This has important consequences for single-molecule transport, where it would be desirable to have reliable and stable metal–molecule contacts. In the case of molecular spintronics, the stable fullerene-based structures proposed here might be useful for transport studies on magnetic atoms and impurities encapsulated inside molecules based on fullerenes.

Results and Discussion

STM room-temperature measurements

Figure 1a shows a constant-current STM image acquired at room temperature after the deposition of C_{60} molecules on the reconstructed Au(111) surface [26-28]. The deposition process was performed at room temperature. In this initial state of adsorption, we observe that almost all the C_{60} molecules are adsorbed at the terrace edges of the monoatomic steps. Molecules are assembled into one-dimensional islands or short chains along the steps. This can be attributed to the increased local reactivity of the step edges [29-31]. STM images taken after Ar^+ bombardment (120 eV, 5 min) [32-34] of the system (Figure 1b) show single bright dots on the surface, which correspond to individual molecules disjoined from islands as a result of the sputtering process. Line profiles (indicated by blue lines in Figure 1b) reveal an apparent height difference of approximately 0.15 nm between the individual molecules and those inside the island.

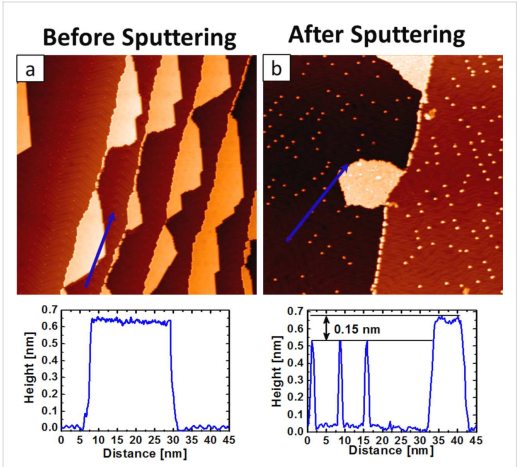

Figure 1: (a) (200 × 200 nm^2) High-resolution STM image (U_b = −0.5 V, I_s = 0.3 nA) of Au (111) after deposition of C_{60}. The molecules formed self-assembled islands, attached to the surface-terrace edges as expected. (b) (200 × 200 nm^2) High-resolution STM image (U_b = −0.6 V, I_s = 0.3 nA) of the system after sputtering with 120 eV Ar^+ ions for 5 min. Single molecules were detached from the islands as the result of the sputtering process. Profiles measured along the indicated blue arrows reveal the apparent height differences between isolated molecules and those inside the island.

Figure 2a shows a high-resolution STM image of the close-packed arrangement of C_{60} inside the island after deposition [35-37]. In addition, we observe dim molecules (indicated by green arrows), which can be attributed to C_{60} molecules above gold vacancies [29,37]. Closer inspection of molecules inside the island after Ar^+ ion bombardment (Figure 2b) enables the sorting of the molecules in the island according to their appear-

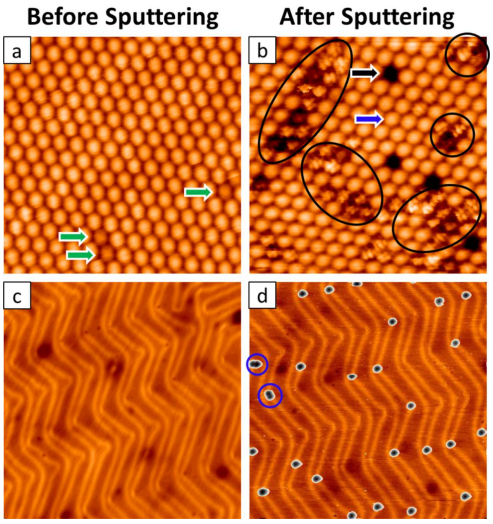

Figure 2: (a) (14 × 14 nm^2) STM image (U_b = −2.5 V, I_s = 0.3 nA) of a fullerene island before Ar^+ bombardment. (b) (14 × 14 nm^2) STM image (U_b = 0.6 V, I_s = 0.3 nA) of the fullerene island after Ar^+ bombardment. The blue arrow indicates a pristine C_{60} molecule. The black arrow points to a vacancy inside the island. Black circles mark regions with modified molecules. (c) (65 × 65 nm^2) STM image (U_b = 1.8 V, I_s = 0.3 nA) of the herringbone reconstruction before Ar^+ bombardment. (d) (65 × 65 nm^2) STM image (U_b = 0.5 V, I_s = 0.09 nA) of single molecules attached to the herringbone elbow sites. Two dimers are enclosed by blue circles.

ance. We can easily identify pristine C_{60} (blue arrow). Also, we observe regions in the island (indicated by black circles) corresponding to modified molecules, with a variation in the topographic heights. We assume that the varying apparent heights of these molecules inside the island stem from different adsorption geometries and possibly the local influence of neighboring molecules. Finally, we observe dark spots in the islands (black arrows in Figure 2b), which we can attribute to holes formed due to the ion bombardment and subsequent departure of the fullerenes from the islands.

Figure 2c shows a high-resolution STM image of reconstructed Au(111) after C_{60} deposition prior to the Ar^+ ion bombardment. From this image, it is clear that no molecules are seen at the elbow sites before soft sputtering. In Figure 2d we observe the adsorption pattern of isolated molecules that were disjoined from the islands after sputtering. Importantly, these molecules bind to the elbow sites of the herringbone reconstruction of the substrate. This can be explained by the increased reactivity of the elbow sites, so-called Shockley partial dislocations of the Au bulk [38,39]. The faulty structure of the elbow site makes it a favorable nucleation site for the functionalized molecules to bind. STM images also show the presence of dimer structures bound at the elbow sites (indicated by blue circles). We attribute these features to be dimers of molecules damaged during the sputtering. The number of observed dimers was very limited.

We turn to the features on the herringbone corners. Given the higher reactivity of these elbow sites, we consider the possibility of the bright spots being normal C_{60} molecules and for the structures on the herringbone corners being unrelated to the formation of molecular defects. However, this scenario can be ruled out since these spots are only observed after sputtering of the fullerene film. First, without sputtering, C_{60} molecules are highly mobile on terraces at room temperature and form islands that are adsorbed at step edges. Second, the creation of reactive sites in the Au surface due to sputtering and to which normal C_{60} molecules could bind, can also be excluded: no features on the elbow sites were observed when sputtering the clean Au surface prior to C_{60} deposition. Molecules bound to the herringbone corner sites were only observed after soft sputtering of the fullerene films, implying that these adsorbates result from an increased reactivity of the molecules after sputtering.

Isolated fullerenes with C vacancies

In order to understand the STM measurements, we carried out electronic-structure calculations based on DFT, focusing on fullerene molecules with vacancy defects where the missing C atoms result in increased reactivity and stronger binding with the substrate. We consider C_{59} molecules, resulting from the removal of a single C atom. While high-energy collisions can result in a wide range of products after removal of a series of fragments [23], it has been shown that sputtering of carbon materials with such low energies as in our case results in predominantly single vacancies [32-34]. C_{59} molecules also have the highest energetic stability after C_{60} [24,25] and, as described below, result in strong and stable bonds to the Au(111) surface, in particular stronger than those of C_{58}. We therefore study the binding of C_{59} species to the substrate which, as detailed below, explains the STM observations.

We start by discussing the structure of isolated C_{59} molecules. From the equilibrium C_{60} molecule, we remove a C atom and explore low-energy structures by optimizing the geometry. The removal of an atom from the C_{60} molecule results in many unsaturated bonds that induce a geometric rearrangement of the molecule. In the calculations, we find two different structural isomers (Figure 3), depending on how the fullerene vacancy is healed. In the first isomer, the atoms surrounding the vacancy rearrange to form two rings, one consisting of four atoms, and the other of nine atoms. In the other one, the C atoms around the vacancy assemble into a ring of eight atoms, and another ring of five atoms. Notice that in both structural isomers two

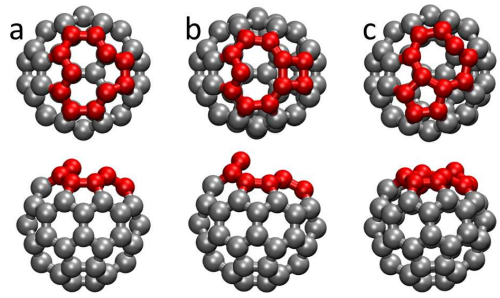

Figure 3: Top and side views of the computed structure of C_{59} structural isomers. Carbon atoms around the vacancy are shown in red. (a) Initial structure for geometry optimization, obtained from a C_{60} molecule by removing one atom. (b) Isomer where the atoms around the vacancy form one four- and one nine-membered ring. (c) More stable isomer having eight- and five-membered rings.

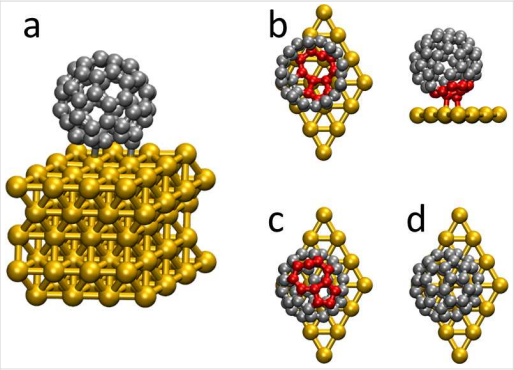

Figure 4: (a) Unit cell used in the calculations. (b) Top and side views of the 8,5-isomer with the single vacancy close to the metal surface. In the top view, the upper C atoms have been removed for clarity. (c) Top view of the 8,5-isomer with the vacancy away from the surface. (d) Fullerene with no defects (C_{60}). Carbon atoms around the vacancy are shown in red.

C atoms belong to both rings, but for clarity we choose to name them according to the total number of atoms in each ring. At the optimized structures, both C_{59} isomers have a carbon atom protruding from the shape of a C_{60} molecule or that of a C_{60} molecule with one missing C atom (the starting geometry of the structural optimizations). Despite the structural rearrangement, interatomic C–C bond distances are not dramatically altered. Calculated interatomic bond distances for C_{60} are 1.42 and 1.47 Å, to be compared to the reported values of 1.40 and 1.46 Å [40,41]. For the 4,9- isomer, C–C distances around the vacancy are in the range of 1.42–1.49 Å, while for the 8,5-isomer the calculated values are between 1.40 and 1.51 Å. When comparing the total energy of both species we find the isomer with 8- and 5-atom rings to be more stable by ca. 0.9 eV than the 4,9-isomer, consistent with previous quantum chemical calculations [25]. Therefore, when considering the adsorbed defected fullerenes on the surface we study the 8,5-isomer only.

Fullerenes with defects adsorbed on the Au(111) surface

We now describe the adsorption of this 8,5-fullerene with vacancy defect on the (111) surface of Au using DFT simulations. The herringbone reconstruction arises from the $22\times\sqrt{3}$ reconstruction of the Au(111) surface. However, the calculation of the very large supercells needed to explicitly describe this reconstruction would require a huge computational effort [42]. We therefore follow previous works and study the adsorption on the ideal (111) surface. Figure 4a shows the unit cell used in the calculations, illustrated for pristine fullerene (C_{60}). There are five Au layers, each consisting of 16 atoms. We calculate the fullerene molecule before and after sputtering, where we model it as having 60 and 59 atoms, respectively. In both cases, above the molecule there is a large vacuum gap. Technical details of the calculations are given in the Experimental section at the end of the paper.

We first screen the possible adsorption geometries by carrying out structural optimizations starting from a series of initial metal–molecule structures. We investigated several initial geometries where the C_{59} molecule was rotated or its center of mass had been shifted, in order to explore the metal–molecule interaction. We considered geometries where the fullerene vacancy was oriented towards the Au substrate ("defect-down" structure) as well as towards the vacuum ("defect-up" structure). Figure 4b–d show the optimized geometries for the fullerene molecules with vacancy defect having the vacancy towards the interface or towards the vacuum, and for the adsorbed pristine C_{60} molecule. We find that, upon adsorption, the calculated interatomic C–C bond distances are only slightly changed compared to the isolated 8,5-isomer. When the vacancy is oriented towards the vacuum, the changes in the C–C bond distances are negligible. In the defect-down geometry they are larger, as expected, with the smaller five-atom ring exhibiting smaller bond distance variations upon adsorption (mean change less than 0.005 Å) than the eight-atom ring (mean change of ca. 0.025 Å). This is consistent with the intuitive idea that the eight-atom ring is more reactive, and in fact is found to be closer to the metal surface in the optimized geometry. From the calculations, the binding energy of the defect-down geometry (Figure 4b) is ca. 1.6 eV. This is much higher than that of the defect-up (Figure 4c) and the pristine C_{60} (Figure 4d) structures. The calculated binding energies of these two structures is (in the absence of van der Waals forces) close to zero. This indicates that changes in the electronic structure arising from the vacancy when it is oriented towards vacuum do not significant-

ly affect the metal–molecule contact. In contrast to the value of the defect-down structure, previous calculations on C_{60}/Au(111) have established that the binding energy results almost solely from van der Waals interactions [43]. Finally, we also considered the case of a double vacancy. Calculations for the binding of a C_{58} molecule with the defect pointing towards the metal result in a binding energy close to 0.6 eV. This value is significantly smaller than that of C_{59}, further supporting the idea that the bright spots observed in STM are fullerenes with single vacancies.

The optimized geometry of the defect-down C_{59} structure has three different C atoms separated by less than 2.5 Å from an Au atom in the surface layer. As expected, one of these atoms is the C atom protruding from the eight-atom ring, consistent with the intuitive notion of its high reactivity and readiness to form bonds with the substrate. As seen in Figure 4b, these small Au–C distances result from the three C atoms being close to an atop position with respect to the Au layer. For comparison, these values are slightly larger than the Au–C distances of ca. 2.1 Å found in other molecular nanostructures [21,22]. In our simulations, we found another local minimum of the C_{59} defect-down configuration with a smaller binding energy of 1.2 eV. In this geometry, the protruding C atom in the eight-atom ring is also close to a surface Au atom, while other C atoms in the eight- and five-membered rings are further away. This shows that, although several atoms around the fullerene vacancy contribute to the binding energy at the interface, the most important contribution comes from the apical C atom sticking out of the former icosahedral structure. In the case of the defect-up and the pristine structures (Figure 4c,d), a C–C bond shared by two hexagons relaxed to a position above a Au surface atom. This was previously found to be a favorable binding site for C_{60}/Au(111) [37]. Changes in the orientation of the defect-up structure resulted in minor variations in the calculated binding energy [43]. This is again consistent with the notion that when the vacancy is oriented towards vacuum, the carbon atoms close to the Au surface are relatively unaffected and the binding to the metal is similar to that of pristine C_{60}.

To sum up, the passivation of the bonds of the C atoms around the vacancy defect by the Au surface results in the formation of metal–molecule bonds and an energy gain of 1.6 eV. On the other hand, a vacancy exposed towards the vacuum would by very unstable and energetically unfavorable and it is unlikely that it would be present in experiment. Finally, from the calculations, the height of the defect-down fullerene is ca. 0.9 Å lower than that of the pristine C_{60} molecule.

Finally, we turn to the electronic properties of the adsorbed fullerenes with vacancy defect, and compare them to those of the C_{60}/Au(111) system. Figure 5 shows the calculated density of states (DOS) of the isolated molecule (dashed lines) and junction (solid lines) projected onto the molecular atoms. Upon adsorption, the calculated spectrum of C_{60} is not appreciably modified, nor is that of C_{59} for the defect-up geometry. When the defect is adsorbed facing the substrate, however, significant changes are seen with respect to the isolated molecule. Spectral features, especially in the empty part of the spectrum, are broadened due to hybridization with metal states. Three scenarios at the interface are compared: the C_{59} molecules adsorbed with the vacancy towards the Au substrate or away from it, and the case of C_{60} for comparison. The spectrum of C_{60} on Au is well known [29,44-46]. Fullerene has a three-fold degenerate LUMO and a five-fold degenerate HOMO. In Figure 5 these are the peaks at about 0.8 and about −0.9 eV. The vacancy defect in the fullerene is related to the existence of states in the former gap of the molecule. For the defect-up geometry this is clearly seen in the peaks at 0.2 and around −0.5 eV, which can be explained by the breaking of degeneracy of one empty and two occupied states. Other molecular states are relatively unaffected compared to C_{60}/Au(111). When the vacancy is adsorbed towards the substrate, the Au–C bonds result in the broadening of the molecular spectrum, and there are broad features in the former energy gap. Identifying individual peaks and comparing them with C_{60} is more difficult but the occupied part of the spectrum seems to have changed more than the empty states upon adsorption. Unfortunately, attempts to reliably measure at room temperature the dI/dV spectrum of molecules adsorbed at the herringbone elbow sites or in islands were unsuccessful.

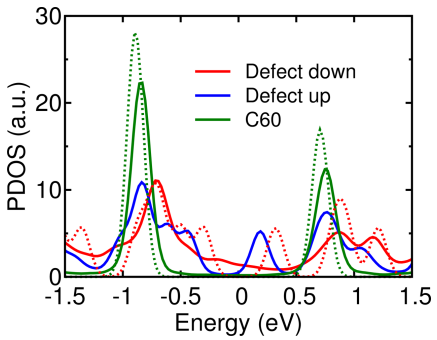

Figure 5: Calculated DOS of fullerenes with and without vacancy defects adsorbed on Au(111). In the case of defects, the molecule was adsorbed with the vacancy close to the surface ("defect-down") or towards the vacuum layer ("defect-up"). The DOS of isolated molecules are shown as dashed lines.

Conclusion

To summarize, we presented a combined theoretical–experimental study of sputtered fullerene-based films on Au(111). We

carried out STM measurements at room temperature in UHV. Initially we observed C_{60} molecules forming islands or chains at terrace edges of monoatomic Au steps. After soft sputtering, bright spots were visible at the Au herringbone corners. Line scans revealed these spots to have an apparent height difference of 1.5 Å with respect to fullerenes in islands. We interpret these bright spots as fullerene molecules with vacancies created by the sputtering process. DFT-based calculations show that C_{59} fullerenes with single defects are consistent with experimental findings. The vacancy created by the removal of a C atom from a fullerene molecule results in structural rearrangement and increased molecular reactivity. We showed that C_{59} molecules adsorbed with the defect close to the surface have a binding energy on Au that is 1.6 eV higher than that of C_{60}. This results from the passivation of C unsaturated bonds around the defect by the Au surface atoms. The calculated metal–molecule structure has several Au–C bond distances below 2.5 Å at the interface. This favorable binding configuration of the fullerene defect is consistent with the stable isolated molecules observed experimentally at the herringbone corners after sputtering. Our work thus provides a pathway for the formation of strong metal–molecule anchors for fullerene-based nanostructures at room temperature.

Experimental

Deposition and sputtering of C_{60}

Experiments were performed in ultrahigh vacuum, variable temperature STM (VT-STM), with base pressure below 5×10^{-10} mbar. Typically, six cycles of Ar^+ ion sputtering (1 kV, 10 min) and annealing (600 °C, 5 min) were required to obtain samples with overall cleanliness suitable for achieving the atomic resolution by means of STM. For deposition, we employed a custom-made thermal evaporation source, which contained a pocket made of tantalum, suitable for the evaporation of molecules such as C_{60}. During the deposition, the evaporation source and substrate were placed inside a vacuum chamber with a base pressure around 5×10^{-10} mbar. Before every deposition, the C_{60} source was preheated to 360 °C and degassed for 5 min to remove contaminations. After this procedure the sample was transferred into the STM head for the deposition of C_{60} by heating the evaporation source at 420 °C. In order to remove C atoms from the C_{60} molecules, the sample was bombarded with Ar^+ ions (120 eV, 5 min).

DFT-based calculations

We use the DFT code Siesta [47] for the calculation of the adsorption and electronic properties. We used single-zeta polarized orbitals for gold and a double-zeta polarized basis for carbon atoms. Exchange–correlation was described with the Perdew–Burke–Ernzerhof implementation of the Generalized Gradient Approximation (GGA) [48]. Each Au layer consisted of 16 atoms and five layers were used in the calculations. A vacuum gap of about 10 Å was introduced above the topmost molecular atom to avoid interaction with the cell images in the *z*-direction. Interface geometries were optimized using the Conjugated Gradient algorithm. We used a 2×2 Monkhorst–Pack grid for the *k*-point sampling of the Brillouin zone. The position of Au atoms in the surface layer and C atoms was relaxed until the forces acting on these atoms were smaller than 0.02 eV/Å. Projected DOS curves were calculated using a denser 15×15 Monkhorst–Pack *k*-point grid at optimized geometries. For the calculation of fullerene binding energies, ghost orbitals were used to correct for basis set superposition errors [49].

Acknowledgements

We gratefully acknowledge financial support from the Czech Science Foundation (GAČR) under project 15-19672S and the Purkyně Fellowship program of the Academy of Sciences of the Czech Republic. T.C. acknowledges support by the project LO1305 of the Ministry of Education, Youth and Sports of the Czech Republic. H.V. thanks the National Grid Infrastructure MetaCentrum for access to computing and storage facilities provided by the "Projects of Large Research, Development, and Innovations Infrastructures" (CESNET LM2015042) program.

References

1. Cuevas, J. C.; Scheer, E. *Molecular Electronics: An Introduction to Theory and Experiment;* World Scientific Series in Nanoscience and Nanotechnology, Vol. 1; World Scientific Publishing Co. Pte. Ltd: Singapore, 2010. doi:10.1142/7434
2. Sanvito, S. *Chem. Soc. Rev.* **2011,** *40,* 3336–3355. doi:10.1039/c1cs15047b
3. McCamey, D. R.; Seipel, H. A.; Paik, S.-Y.; Walter, M. J.; Borys, N. J.; Lupton, J. M.; Boehme, C. *Nat. Mater.* **2008,** *7,* 723–728. doi:10.1038/nmat2252
4. Su, T. A.; Neupane, M.; Steigerwald, M. L.; Venkataraman, L.; Nuckolls, C. *Nat. Rev. Mater.* **2016,** *1,* 16002. doi:10.1038/natrevmats.2016.2
5. Kroto, H. W.; Heath, J. R.; O'Brien, S. C.; Curl, R. F.; Smalley, R. E. *Nature* **1985,** *318,* 162–163. doi:10.1038/318162a0
6. Rosei, F.; Schunack, M.; Naitoh, Y.; Jiang, P.; Gourdon, A.; Laegsgaard, E.; Stensgaarda, I.; Joachim, C.; Besenbacher, F. *Prog. Surf. Sci.* **2003,** *71,* 95–146. doi:10.1016/S0079-6816(03)00004-2
7. Bonifazi, D.; Enger, O.; Diederich, F. *Chem. Soc. Rev.* **2007,** *36,* 390–414. doi:10.1039/B604308A
8. Moriarty, P. J. *Surf. Sci. Rep.* **2010,** *65,* 175–227. doi:10.1016/j.surfrep.2010.08.001
9. Kiguchi, M.; Kaneko, S. *Phys. Chem. Chem. Phys.* **2013,** *15,* 2253–2267. doi:10.1039/C2CP43960C
10. Schwarz, F.; Lörtscher, E. *J. Phys.: Condens. Matter* **2014,** *26,* 474201. doi:10.1088/0953-8984/26/47/474201
11. Sun, L.; Diaz-Fernandez, Y. A.; Gschneidtner, T. A.; Westerlund, F.; Lara-Avila, S.; Moth-Poulsen, K. *Chem. Soc. Rev.* **2014,** *43,* 7378–7411. doi:10.1039/C4CS00143E

12. Leary, E.; La Rosa, A.; González, M. T.; Rubio-Bollinger, G.; Agraït, N.; Martín, N. *Chem. Soc. Rev.* **2015,** *44,* 920. doi:10.1039/C4CS00264D
13. Yagi, Y.; Briere, T. M.; Sluiter, M. H. F.; Kumar, V.; Farajian, A. A.; Kawazoe, Y. *Phys. Rev. B* **2004,** *69,* 075414. doi:10.1103/PhysRevB.69.075414
14. Sakai, S.; Yakushiji, K.; Mitani, S.; Takanashi, K.; Naramoto, H.; Avramov, P. V.; Narumi, K.; Lavrentiev, V.; Maeda, Y. *Appl. Phys. Lett.* **2006,** *89,* 113118. doi:10.1063/1.2354035
15. Koleini, M.; Brandbyge, M. *Beilstein J. Nanotechnol.* **2012,** *3,* 589–596. doi:10.3762/bjnano.3.69
16. Lu, X.; Feng, L.; Akasaka, T.; Nagase, S. *Chem. Soc. Rev.* **2012,** *41,* 7723–7760. doi:10.1039/c2cs35214a
17. Saffarzadeh, A.; Kirczenow, G. *Appl. Phys. Lett.* **2013,** *102,* 173101. doi:10.1063/1.4803471
18. Stróżecka, A.; Muthukumar, K.; Dybek, A.; Dennis, T. J.; Larsson, J. A.; Mysliveček, J.; Voigtländer, B. *Appl. Phys. Lett.* **2016,** *95,* 133118. doi:10.1063/1.3236529
19. Guo, S.; Fogarty, D. P.; Nagel, P. M.; Kandel, S. A. *J. Phys. Chem. B* **2004,** *108,* 14074–14081. doi:10.1021/jp048481m
20. Kaneko, S.; Wang, L.; Luo, G.; Lu, J.; Nagase, S.; Sato, S.; Yamada, M.; Slanina, Z.; Akasaka, T.; Kiguchi, M. *Phys. Rev. B* **2012,** *86,* 155406. doi:10.1103/PhysRevB.86.155406
21. Cheng, Z.-L.; Skouta, R.; Vazquez, H.; Widawsky, J. R.; Schneebeli, S.; Chen, W.; Hybertsen, M. S.; Breslow, R.; Venkataraman, L. *Nat. Nanotechnol.* **2011,** *6,* 353–357. doi:10.1038/nnano.2011.66
22. Chen, W.; Widawsky, J. R.; Vázquez, H.; Schneebeli, S. T.; Hybertsen, M. S.; Breslow, R.; Venkataraman, L. *J. Am. Chem. Soc.* **2011,** *133,* 17160–17163. doi:10.1021/ja208020j
23. Gatchell, M.; Zettergren, H. *J. Phys. B: At., Mol. Opt. Phys.* **2016,** *49,* 162001. doi:10.1088/0953-4075/49/16/162001
24. Hu, Y. H.; Ruckenstein, E. *J. Chem. Phys.* **2003,** *119,* 10073. doi:10.1063/1.1617971
25. Lui, L. V.; Tian, W. Q.; Wang, Y. A. *Int. J. Quantum Chem.* **2009,** *109,* 3441. doi:10.1002/qua.22298
26. Altman, E. I.; Colton, R. J. *Surf. Sci.* **1992,** *279,* 49–67. doi:10.1016/0039-6028(92)90741-N
27. Altman, E. I.; Colton, R. J. *Phys. Rev. B* **1993,** *48,* 18244–18249. doi:10.1103/PhysRevB.48.18244
28. Altman, E. I.; Colton, R. J. *Surf. Sci.* **1993,** *295,* 13–33. doi:10.1016/0039-6028(93)90181-I
29. Paßens, M.; Waser, R.; Karthäuser, S. *Beilstein J. Nanotechnol.* **2015,** *6,* 1421–1431. doi:10.3762/bjnano.6.147
30. Zhang, X.; Yin, F.; Palmer, R. E.; Guo, Q. *Surf. Sci.* **2008,** *602,* 885–892. doi:10.1016/j.susc.2007.12.036
31. Gardener, J. A.; Briggs, G. A. D.; Castell, M. R. *Phys. Rev. B* **2009,** *80,* 235434. doi:10.1103/PhysRevB.80.235434
32. Lehtinen, O.; Kotakoski, J.; Krasheninnikov, A. V.; Tolvanen, A.; Nordlund, K.; Keinonen, J. *Phys. Rev. B* **2010,** *81,* 153401. doi:10.1103/PhysRevB.81.153401
33. Krasheninnikov, A. V.; Banhart, F. *Nat. Mater.* **2007,** *6,* 723. doi:10.1038/nmat1996
34. López-Polín, G.; Gómez-Navarro, C.; Parente, V.; Guinea, F.; Katsnelson, M. I.; Pérez-Murano, F.; Gómez-Herrero, J. *Nat. Phys.* **2015,** *11,* 26–31. doi:10.1038/nphys3183
35. Wang, H.; Zeng, C.; Wang, B.; Hou, J. G.; Li, Q.; Yang, J. *Phys. Rev. B* **2001,** *63,* 085417. doi:10.1103/PhysRevB.63.085417
36. Schull, G.; Berndt, R. *Phys. Rev. Lett.* **2007,** *99,* 226105. doi:10.1103/PhysRevLett.99.226105
37. Shin, H.; Schwarze, A.; Diehl, R. D.; Pussi, K.; Colombier, A.; Gaudry, É.; Ledieu, J.; McGuirk, G. M.; Serkovic Loli, L. N.; Fournée, V.; Wang, L. L.; Schull, G.; Berndt, R. *Phys. Rev. B* **2014,** *89,* 245428. doi:10.1103/PhysRevB.89.245428
38. Barth, J. V.; Brune, H.; Ertl, G.; Behm, R. J. *Phys. Rev. B* **1990,** *42,* 9307. doi:10.1103/PhysRevB.42.9307
39. Maksymovych, P.; Sorescu, D. C.; Dougherty, D.; Yates, J. T., Jr. *J. Phys. Chem. B* **2005,** *109,* 22463. doi:10.1021/jp058154u
40. Hedberg, K.; Hedberg, L.; Bethune, D. S.; Brown, C. A.; Dorn, H. C.; Johnson, R. D.; De Vries, M. *Science* **1991,** *254,* 410. doi:10.1126/science.254.5030.410
41. Leclercq, F.; Damay, P.; Foukani, M.; Chieux, P.; Bellissent-Funel, M. C.; Rassat, A.; Fabre, C. *Phys. Rev. B* **1993,** *48,* 2748. doi:10.1103/PhysRevB.48.2748
42. Hanke, F.; Björk, J. *Phys. Rev. B* **2013,** *87,* 235422. doi:10.1103/PhysRevB.87.235422
43. Hamada, I.; Tsukada, M. *Phys. Rev. B* **2011,** *83,* 245437. doi:10.1103/PhysRevB.83.245437
44. Lu, X.; Grobis, M.; Khoo, K. H.; Louie, S. G.; Crommie, M. F. *Phys. Rev. B* **2004,** *70,* 115418. doi:10.1103/PhysRevB.70.115418
45. Schull, G.; Néel, N.; Becker, M.; Kröger, J.; Berndt, R. *New J. Phys.* **2008,** *10,* 065012. doi:10.1088/1367-2630/10/6/065012
46. Wang, L.-L.; Cheng, H.-P. *Phys. Rev. B* **2004,** *69,* 165417. doi:10.1103/PhysRevB.69.165417
47. Soler, J. M.; Artacho, E.; Gale, J. D.; García, A.; Junquera, J.; Ordejón, P.; Sánchez-Portal, D. *J. Phys.: Condens. Matter* **2002,** *14,* 274. doi:10.1088/0953-8984/14/11/302
48. Perdew, J. P.; Burke, K.; Ernzerhof, M. *Phys. Rev. Lett.* **1996,** *77,* 3865–3868. doi:10.1103/PhysRevLett.77.3865
49. van Duijneveldt, F. B.; van Duijneveldt-van de Rijdt, J. G. C. M.; van Lenthe, J. H. *Chem. Rev.* **1994,** *94,* 1873–1885. doi:10.1021/cr00031a007

License and Terms

4.2 Nitrous oxide as an effective AFM tip functionalization: a comparative study

Sub-molecular resolution of various organic molecules and nanostructures are routinely achieved by means of nc-AFM with a CO functionalized tip[29;114]. Additionally, the metal tip apex can be functionalized with different molecular species[115–117] or single atoms[28;118;119] which can also achieve sub-molecular resolution. Properties of the tip termination such as chemical structure, internal charge distribution, and structural flexibility can significantly affect the contrast and cause distortion in molecular images. Therefore, it is important to explore new potential candidates for tip functionalization and characterize their unique properties.

4.2.1 Why do we need AFM with functionalized tips?

The invention of the qPlus sensor[26] made possible to obtain nc-AFM images of the fairly reactive Si(111) – (7x7) surface[120]. The high stiffness of the tuning fork enables small amplitude oscillations which overcome the jump to contact problem while operating in the regime of small tip sample distances. These positive attributes make the qPlus sensor a core element for nc-AFM being able to investigate all variety of sample surfaces from conductors to insulators and the measurement of tiny forces acting during atom manipulation[24].

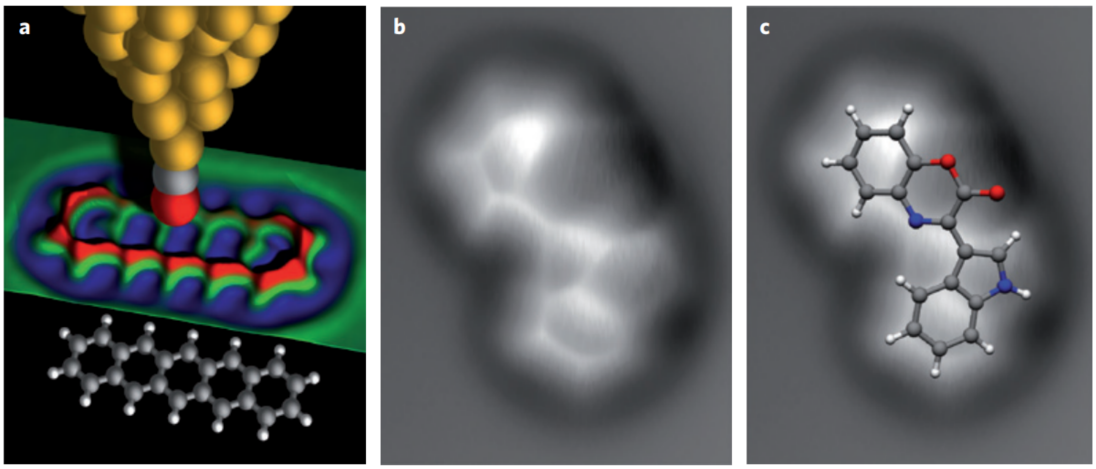

Figure 4.3: Sub-molecular resolution with a CO functionalized tip. (a) Schematic representation of the metal tip passivated with a CO molecule scanning over a molecule. (b) nc-AFM Δf image of a Cephalandole A molecule obtained with a CO functionalized tip. (C) The data in b) with overlaid ball and stick model. Images taken from L.Gross[121].

To obtain sub-molecular resolution of a single organic molecule one needs to

approach the reactive metal tip so close that it inevitably leads to unintentional transfer of the molecule to the tip apex. In order to solve this problem Leo Gross and co-workers came up with the brilliant idea to passivate the reactive metal tip apex with a single carbon monoxide molecule[29] (see Fig. 4.3 a). The functionalization of the tip apex with a single CO molecule allows one to approach the tip to the point where repulsive forces become dominant without any unintentional manipulation of the investigated molecule. This approach enabled the first sub-molecular resolution of a single pentacene molecule and heralded a new era in the investigation of molecules on surfaces.

Furthermore, tip functionalization allows for bond order discrimination[32] and determination of the molecular adsorption geometry[31]. Most importantly, high-resolution imaging with a CO molecule has become the ultimate technique for identification of different molecular structures[30]. The example presented on Fig. (4.3 b,c) of the imaged molecule was identified as Cephalandole A using high resolution imaging techniques with the help of supplementary techniques such as Nuclear Magnetic Resonance (NMR) spectroscopy and DFT calculations.

At a first glance, the AFM image on Fig. (4.3 b) is simply representing the atomic structure of the investigated molecule. However, it is not that simple. Atomic contrast mainly originates from a complex interaction between the CO and the species under investigation. The nc-AFM signal is a sum of long- and short-range force contributions (see Chapter 1 for more details). The chemical inertness of the CO molecule enables the smallest accessible tip-sample separation and allows operation in the repulsive regime where atomic contrast starts to be observed. As a result, the CO molecule starts to deflect while experiencing the repulsive interaction caused by overlap of the electron wave functions. Hence, the observed repulsive atomic contrast is primarily attributed to Pauli repulsion[56].

4.2.2 Effect of different tip functionalizations

While the flexibility of the CO molecule leads to a high spatial resolution of the bonds it also causes distortion in the appearance of investigated molecules[122]. Consequently, intermolecular features like benzene rings and bond lengths appear elongated.

On the other hand, tip functionalization for sub-molecular resolution is not restricted to CO. For instance, the tip apex can be decorated with various atoms such as Br, Cl, Xe[28], O[118] which yield similar atomic resolution in comparison to CO (see Fig. 4.4). However, the chemical structure of the molecule is more clearly resolve in the case of the CO tip despite the fact that the Xe tip produces less distortion as can be seen from Laplacian filtered image on Fig. (4.4 g,h)[28].

AFM tips with different termination, have comparative advantages depending on the measurement. For example, tips functionalized with O or Xe atoms

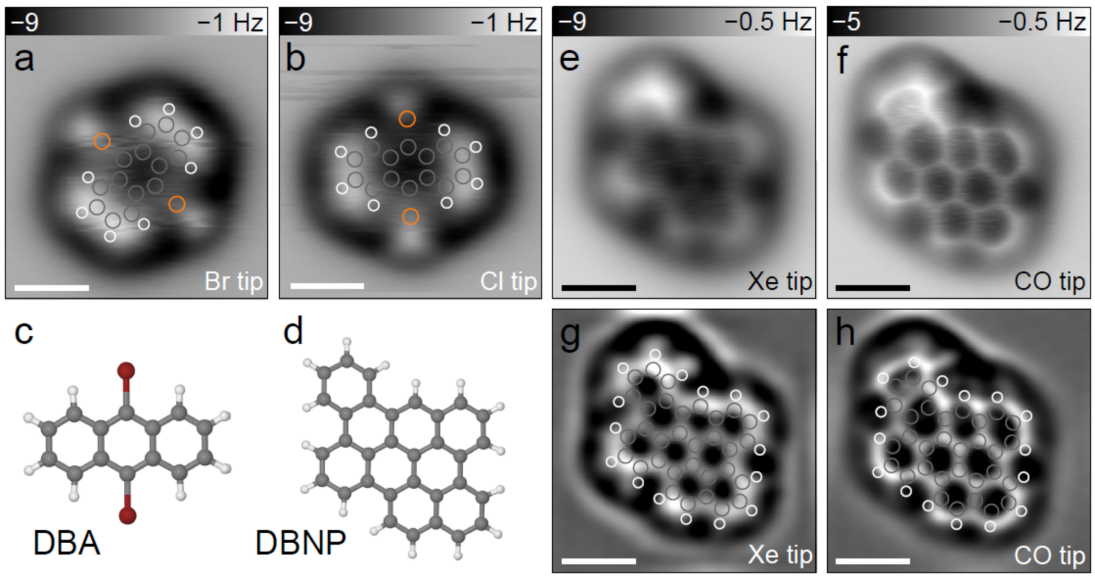

Figure 4.4: Comparison of different tip terminations for nc-AFM. Sub-molecular resolution of DBA and DBNP molecules on NaCl(2ML)/Cu(111) obtained with (a) Br (b) Cl (e) Xe (f) CO tip terminations. Scale bars: 5 Å. Image taken from B. Schuler[123]

provides accurate absorption heights and geometry determination while Br tips facilitate atomic manipulation[28]. At the moment of writing this PhD thesis, the CO tip was the best suited for identification of molecular structure, bond order discrimination and adsorption site determination[28].

4.2.3 The process of the tip functionalization with a single N_2O molecule

The atomic structure of the metal cluster supporting a molecular termination can affect the AFM contrast and cause undesired image distortion[122]. This problem can be solved by using linear three atomic molecules for tip termination as proposed by Xin et. al[124]. Therefore, in the following study (see paper II, page 46) we explore the possibility of tip functionalization with the single nitrous oxide molecule (N_2O). N_2O is a linear triatomic molecule and has proven to be UHV compatible.

In paper II on page 46 we present a new tip functionalization with a single nitrous oxide molecule. A N_2O molecule was picked up from a Au(111) surface at 5 K. Stable bonding of N_2O on the tip apex permits reliable STM/AFM with sub-molecular contrast of a single Fe(II)-phthalocyanine (FePc) molecule (see Fig. 5 in paper II page 49). We compare nc-AFM images obtained with a N_2O-tip to the more commonly used CO-tip. Our high-resolution images with N_2O show features comparable to those acquired with CO tips. DFT calculations reveal that the N_2O and CO tips have a similar electrostatic potential maps. Additionally

we study the adsorption of N_2O molecules on the Au(111) surface by means of STM/AFM with N_2O functionalized tips combined with AFM simulations[114].

My contribution to the Paper II can be summarized as follows: I performed all the nc-AFM and STM measurements as well as sample preparation. I characterized the adsorption of the N_2O molecules on a Au(111) and performed tip functionalization with single N_2O molecules. I obtained sub-molecular resolution of single FePc molecules using both N_2O and CO tip terminations. I obtained site specific force spectroscopy with both tip terminations. I was the primary contributor to the data analysis, preparation of the results, and composition of the manuscript.

BEILSTEIN JOURNAL OF NANOTECHNOLOGY

Nitrous oxide as an effective AFM tip functionalization: a comparative study

Taras Chutora[1], Bruno de la Torre[*1,2], Pingo Mutombo[2], Jack Hellerstedt[2], Jaromír Kopeček[2], Pavel Jelínek[1,2] and Martin Švec[*1,2]

Full Research Paper

Open Access

Address:
[1]Regional Centre of Advanced Technologies and Materials, Department of Physical Chemistry, Faculty of Science, Palacký University, Šlechtitelů 27, 78371 Olomouc, Czech Republic and [2]Institute of Physics of the Czech Academy of Sciences, Cukrovarnická 10, 162 00 Prague, Czech Republic

Email:
Bruno de la Torre[*] - bruno.de@upol.cz; Martin Švec[*] - svec@fzu.cz

* Corresponding author

Keywords:
atomic force microscopy; Au(111); carbon monoxide; functionalization; high resolution; nitrous oxide; submolecular resolution

Beilstein J. Nanotechnol. **2019,** *10,* 315–321.
doi:10.3762/bjnano.10.30

Received: 24 October 2018
Accepted: 07 January 2019
Published: 30 January 2019

This article is part of the thematic issue "Advanced atomic force microscopy II".

Guest Editor: T. Glatzel

Abstract

We investigate the possibility of functionalizing Au tips by N_2O molecules deposited on a Au(111) surface and their further use for imaging with submolecular resolution. First, we characterize the adsorption of the N_2O species on Au(111) by means of atomic force microscopy with CO-functionalized tips and density functional theory (DFT) simulations. Subsequently we devise a method of attaching a single N_2O to a metal tip apex and benchmark its high-resolution imaging and spectroscopic capabilities using FePc molecules. Our results demonstrate the feasibility of high-resolution imaging. However, we find an inherent asymmetry of the N_2O probe-particle adsorption on the tip apex, in contrast to a CO tip reference. These findings are consistent with DFT calculations of the N_2O- and CO tip apexes.

Introduction

Frequency-modulated atomic force microscopy (AFM) has become the tool of choice for the characterization of molecules on the atomic scale. Functionalization of a metallic tip apex with a single carbon monoxide molecule (CO) was the key to achieve submolecular resolution for the first time, on a pentacene molecule [1]. This milestone initiated a vigorous development of the technique that now serves a variety of purposes. For example, it can identify molecular structures of natural and pure compounds [2-5], determine the bond order in conjugated systems [6], visualize intramolecular charge distributions [7-9], image three-dimensional molecular structures [10-12], discern complex molecular mixtures [13,14], resolve the intermediate states of chemical reactions [15-19] or discriminate the spin state of single molecules [20].

In most of these cases, the functionalized tip is routinely obtained by picking up a single CO molecule from the substrate. Applying an analogous approach, atomically sharp metal apexes can be also decorated either by different molecular species such as C_{60} [21], naphthalenetetracarboxylic diimide (NTCDI) [22], NO [23] or single atoms such as Xe [24,25], Br [24], Kr [24], O [26], and Cl [1,27]. Such tip terminations have proved to be fairly stable and therefore capable of achieving submolecular resolution. The characteristics of each type of tip termination, such as chemical structure or internal charge distribution, are extremely important for the AFM contrast, distortions in the molecule images, and spatial resolution [8,27,28]. The tip-terminating particle also significantly affects the spectroscopy measurements, i.e., the interaction energy toward different atomic species in force spectroscopy, the contact potential difference in Kelvin probe force microscopy (KPFM) [9,29] and vibrational levels of inelastic tunneling spectroscopy (IETS) [30,31]. A particular termination of the tip may be bound to certain types of substrates, and better suited for a limited range of investigated objects, such as molecules with specific functional groups or atomic impurities with characteristic charge distribution. Therefore it is of utmost importance to search for new potentially practical molecules for tip functionalization and describe their unique properties.

Here we present a process in which N_2O was deposited on a Au(111) substrate and characterized. Subsequently we functionalized the Au tip with N_2O and benchmarked its capabilities by imaging a FePc molecule and performing force–distance spectroscopy. The data is compared to equivalent measurements done with a Au tip functionalized with CO.

Results and Discussion

A clean Au(111) surface was inserted into the microscope head and cooled to 5 K before exposing it to N_2O gas. Figure 1a shows a characteristic constant-current image of the N_2O/Au(111) system, revealing the formation of small 2D clusters, preferentially located at the kinks of the characteristic herringbone structure. Their variable size is typically a few nanometers in diameter. The estimated average apparent height of the cluster formations was 70 pm.

After the N_2O cluster formation, the metallic tip (pre-treated by a gentle indentation into the substrate) was functionalized by an impurity CO molecule, which significantly improved the resolution in both STM and AFM. We performed high-resolution AFM/STM measurements on various clusters (comparable to the inset of Figure 1a), which revealed elongated structures; we attribute these to individual flat-lying N_2O molecules. In a cluster, typically composed of 5–25 molecules, the N_2O molecules have a preferential short-range arrangement of rotationally symmetrical trimers, with intermolecular distances of about 4.3 Å. A DFT calculation of a single N_2O molecule on the surface confirms that its adsorption configuration on Au(111) is primarily driven by a non-covalent dispersion interaction and prefers to orient its longer axis parallel to the $[2\bar{1}\bar{1}]$ axis of the surface. The vertical distance between the single molecule and the surface was estimated to be 3.5 Å. Based on this finding, we construct an atomic model of the three flat-lying N_2O molecules on Au(111) and optimize it with total-energy DFT calculations. We find that the trimer is stabilized by electrostatic interactions between the N and O atoms of adjacent N_2O molecules, due to their slightly different polarization. The calculations reveal that the preferred orientation of the N_2O molecules in the clusters is with the O atoms outward (Figure 1b), being 17 meV more stable than the opposite arrangement.

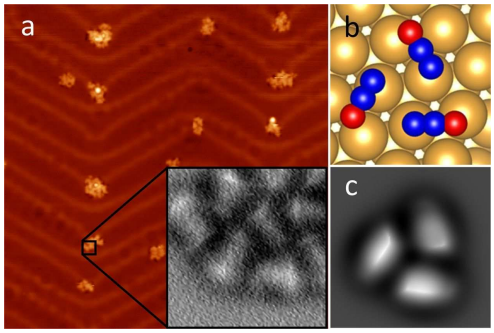

Figure 1: Adsorption of N_2O molecules on the Au(111) substrate. (a) Overview STM image (100 mV, 10 pA, 50 × 50 nm^2) of a sample after N_2O deposition. Inset: a close-up AFM image (1.5 × 1.5 nm^2) of the N_2O cluster adsorbed on the herringbone elbow, scanned with a CO-functionalized tip. (b) Top view of the calculated adsorption geometry of a N_2O trimer. (c) Simulated AFM image (1.5 × 1.5 nm^2) of a N_2O trimer on Au (111) using the probe-particle model [32].

Using the optimized geometry of the cluster obtained from DFT calculations, as an input for the probe-particle model [32], we simulated the AFM images to determine the atomic contrast of the N_2O trimer (Figure 1c). Note that the probe–particle was mimicking a CO molecule. We found good agreement between theory and experiment.

We were able to functionalize the tip with a N_2O molecule. In various attempts to adsorb N_2O onto the tip, we discovered that by intentionally reducing the bias to 50–100 mV for several seconds in constant-current mode while scanning an area containing a cluster of N_2O molecules, a sudden improvement of the resolution occurred (as shown in Figure 2a). This event is characteristic for the tip picking up a molecule from the surface [33,34] and therefore can be attributed to a transfer of a N_2O

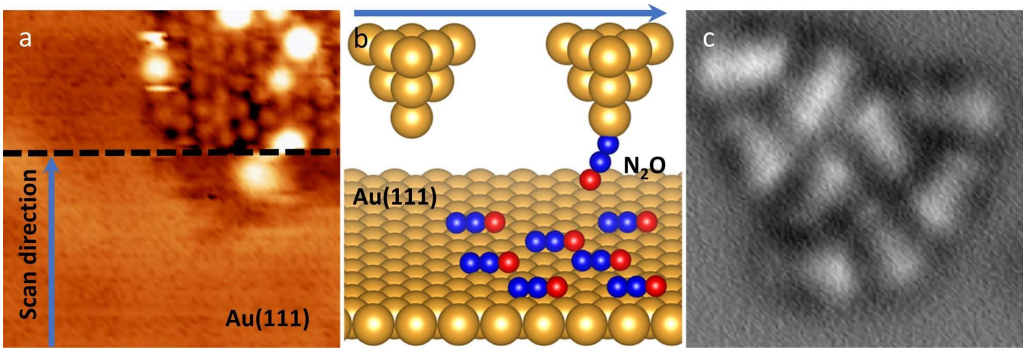

Figure 2: Tip functionalization with a N_2O molecule. (a) STM image (100 mV, 10 pA, 6 × 6 nm^2) demonstrating a spontaneous enhancement of the resolution while scanning over the N_2O-covered surface. (b) Schematic representation of the functionalization process (blue arrow indicates the scan direction). (c) Constant-height AFM image (2 × 2 nm^2) of a single N_2O cluster obtained with a N_2O-functionalized tip.

molecule from the surface to the tip apex, as schematically shown in Figure 2b. We propose that the N_2O molecule is attached to the tip apex through the terminal N (Figure 2b), which has a more reactive character compared to the O atom [35]. In this manner, the O atom would be responsible for the majority of interaction with the substrate.

After functionalization of the tip apex with a single N_2O molecule, we obtained a high-resolution AFM image of the N_2O cluster (Figure 2c). The N_2O tip exhibits good stability during the measurement, allowing us to scan at smaller tip–sample separations and to enter the Pauli repulsion regime. The AFM image of the N_2O cluster Figure 2c shows a remarkably similar resolution to the images acquired with a CO-decorated tip.

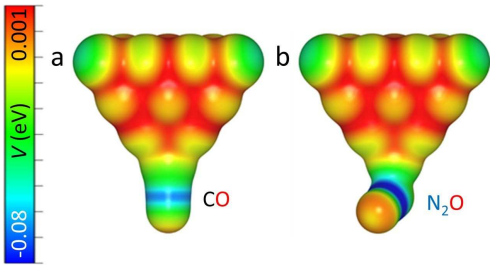

Figure 3: Comparison of the calculated electrostatic potential projections of the CO (a) and N_2O (b) tips obtained through DFT calculations.

In order to understand the chemical behavior of the N_2O tips and compare them to the CO tips, we carried out DFT calculations of their electrostatic potential and total densities (see Methods for more detail). Figure 3 shows the calculated electrostatic potential (ESP) map for CO and N_2O attached to a Au pyramid, projected onto isosurfaces of their respective total electron densities (cut at 0.03 e/A^3). The spatial ESP variation is an important factor for the determination of the molecular reactivity and can be interpreted as the static distribution of the charge around the molecule [36].

The ESP maps of the CO and the N_2O molecule attached to the gold tip (Figure 3) possess some similar characteristics. Both molecules have similar variation of the potential along the probe molecule, i.e., the regions with negative values around the C–O and N–O bonds (electron-rich area, colored in blue) and regions with positive values at the terminal O atoms (electron-poor area, colored in red). This indicates that the N_2O tip is very similar to the CO tip in terms of spatial charge distribution. However, the Hirschfeld analysis [37] of atomic charge at the O apex atom gives −0.077*e* for the N_2O tip, compared to −0.055*e* for the CO tip. This can result in a larger electrostatic interaction of the N_2O probe with a charged atom or molecule. Also, the geometry of the probe particles on the tip is remarkably different. The CO molecule is attached to the Au pyramid almost perfectly on its axis, whereas N_2O is bent strongly. The bent adsorption configuration of the N_2O molecule is caused by electrostatic interactions between the molecule and the Au tip, which arise from the mutual dipole–dipole interaction. Furthermore, the calculated adsorption energies of the two molecules on the tip differ as well. We have found a value of −0.840 eV for CO, compared to −0.156 eV for N_2O. So while a N_2O tip might still provide the resolution and sensitivity needed for submolecular imaging, an asymmetry is expected in the images made by the N_2O tips and interaction forces may have a larger electrostatic contribution.

To benchmark the performance of the N_2O-decorated tip experimentally, we used it to obtain high-resolution STM/AFM images of a single FePc molecule, which is suitable as a standard due to its planar shape and the flat adsorption geometry on Au(111) [31]. A submonolayer coverage of FePc molecules was deposited on Au(111) at room temperature, and the FePc/Au(111) surface was subsequently cooled down in the microscope and exposed to N_2O. Figure 4 shows an overview STM image of the obtained sample, where the FePc molecules predominantly occupy the fcc-stacked Au regions and the kinks of the Au(111) herringbone reconstruction. The N_2O species adsorbs planarly as in the previous experiment, clustering in the vicinity of single FePc molecules. To functionalize the tip with a single N_2O molecule on such a sample we used the procedure described above. We scan a small region around a single FePc molecule that is surrounded by N_2O molecules, at a setpoint of 50 mV and 20 pA until the characteristic change in the contrast, which is associated with the functionalization, occurs (inset of Figure 4).

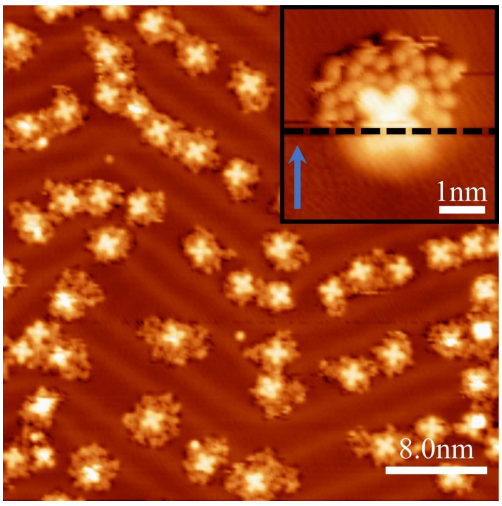

Figure 4: Constant-current STM images of the co-adsorption of FePc and N_2O molecules on a Au(111) surface (200 mV, 20 pA, 40 × 40 nm^2), imaged with a N_2O-functionalized tip. Inset: STM image (50 mV, 20 pA, 5 × 5 nm^2) of a FePc molecule surrounded by N_2O species, demonstrating a tip-functionalization event (on the scan line marked by the dashed line). The scan direction is indicated by a blue arrow.

With this functionalized tip, we performed imaging with submolecular resolution on one of the FePc molecules, surrounded by the N_2O species. Figure 5a shows the corresponding set of constant-height STM/AFM maps, along with the reference data acquired with a CO tip on a single FePc molecule on Au(111).

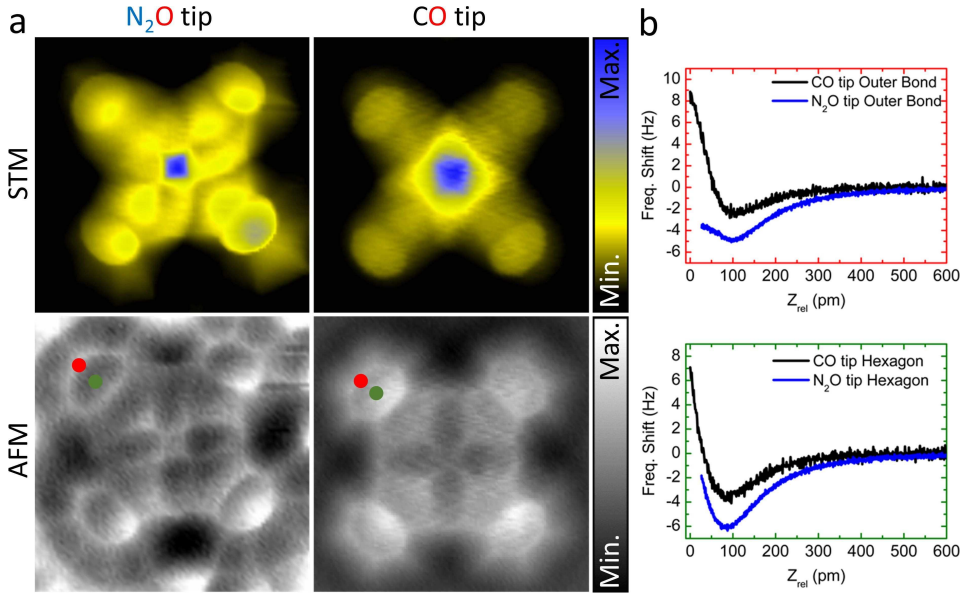

Figure 5: (a) STM and AFM constant-height images of the FePc on Au(111) (1.7 × 1.7 nm^2, V_b = 3 mV) obtained with two different tip terminations, N_2O and CO. The STM scale for N_2O ranges from 0.6 to 43 pA and for CO from 3.8 to 410 pA. The AFM gray scale for N_2O ranges from −23 to −12 Hz and for CO from −12 to 10 Hz. (b) Site-specific Δf spectroscopy obtained with N_2O and CO tip terminations above the outer C–C bonds (red dot) and the centers (green dot) of the peripheral benzene rings of the molecule.

The observed AFM contrast for both the tips generally corresponds to the FePc backbone structure; it shows the four peripheral benzene rings, the inner pyrrole groups and a signature of the metal atom at the center. In the STM images both tips detect a dominating electron tunneling contribution of the central Fe molecular orbital at the Fermi level [31] and also the overall shape of the molecule.

The AFM image taken with the N_2O tip exhibits slightly lower resolution, in comparison to the CO tip termination, with a strong directionality of the submolecular features within the peripheral benzene rings. The tunneling current image also reveals a significant shadow cast in the same direction as the asymmetric features in AFM. These features are indicative of a general probe asymmetry, consistent with the theoretical calculations, which shows a strongly bent adsorption configuration of the N_2O molecule on the tip apex.

For a quantitative comparison of the interaction energy of the two tip terminations with FePc, we performed site-specific frequency-shift spectroscopy $\Delta f(z)$ measurements on the outer C–C bonds and centers of the peripheral benzene molecules indicated by the red and green dots in Figure 5a. In Figure 5b, the short-range Δf curves recorded with N_2O and CO tips are shown (after subtracting the background measured on clean Au [38]). The $\Delta f(z)$ dependence recorded for the N_2O tips is considerably different from the one obtained with a CO tip, both qualitatively and quantitatively. The value of the maximum attractive force [39] for the N_2O tip (Figure S1, Supporting Information File 1) on both spectroscopy sites (outer C–C bond, $F_{N_2O} \approx -125$ pN, and hollow site, $F_{N_2O} \approx -132$ pN) are significantly higher in comparison to the CO tip (outer C–C bond, $F_{CO} \approx -30$ pN, and hollow site, $F_{CO} \approx -56$ pN). Consequently, the interaction energies (Figure S1, Supporting Information File 1) measured with the N_2O tip (outer C–C bond, $E_{N_2O} \approx -156$ meV, and hollow site, $E_{N_2O} \approx -167$ meV) are substantially greater in comparison to the values measured by the CO tip (outer C–C bond, $E_{CO} \approx -43$ meV, and hollow site, $E_{CO} \approx -75$ meV). This difference can be understood as a result of stronger electrostatic interaction of the molecule with the N_2O tip, which is consistent with the DFT calculations of the two different tip terminations.

Conclusion

We have investigated the behavior of N_2O molecules on the surface of Au(111) and determined that they adsorb parallel to the surface, forming typical triangular clusters. We were able to readily functionalize a metallic tip with a single N_2O molecule by picking it up from the Au(111) substrate and demonstrated that the functionalization of the tip can be achieved even when N_2O is co-adsorbed on the surface with other species, in this case FePc molecules. We evaluated the performance of the N_2O tips in submolecular imaging of FePc and site-specific $\Delta f(z)$ spectroscopies. We reproducibly achieved a resolution qualitatively equivalent to the resolution otherwise routinely observed with CO tips, distinguishable by a noticeable asymmetry and higher interaction energies, indicative of a bent adsorption geometry of the N_2O on the tip and more electrostatic charge relative to CO. These observations were corroborated by DFT calculations.

Methods

Experimental

Experiments were carried out in an ultra-high vacuum STM/AFM system (Createc) operated at 5 K. The Au(111) sample (Mateck) was cleaned by repeated cycles of sputtering (1 keV) and subsequent annealing to 600 °C. FePc molecules (Sigma Aldrich, evaporation temperature ca. 250 °C) were directly evaporated onto a clean Au(111) surface at room temperature. N_2O was adsorbed onto the Au(111) surface at temperatures below 12 K with exposures of 0.5–1.7 L. AFM measurements were performed with a qPlus sensor (resonance frequency ca. 30 kHz; $k \approx 1800$ N/m), using an oscillation amplitude of 50 pm. Prior to functionalization, the Pt tip was repeatedly indented into the Au(111) substrate several nanometers deep for sharpening and coating with Au. Experimental data were analyzed using WSxM software [40]; all models were visualized using Vesta software [41].

DFT calculations

We performed density functional theory calculations using the FHI-AIMS code [42] to study the interaction of N_2O with the Au(111) surface. We have used a 6 × 6 supercell, composed of three Au layers to represent the Au(111) surface. Both a single molecule and trimer clusters were initially placed on the surface according to experimental findings. The structural optimization of the slab was carried out, except for the two bottom Au layers, until the remaining atomic forces and the total energy were found to be below 10^{-2} eV/Å and 10^{-5} eV, respectively. A Monkhorst–Pack grid of 3 × 3 × 1 was used for integration in the Brillouin zone.

DFT calculations were performed at the GGA-PBE level including the Tkatchenko–Scheffler treatment of the van der Waals interactions [43]. The scaled zeroth-order regular approximation [44] was applied to take into account the relativistic effects. The total density and the Hartree potential were calculated to determine the electronic interactions between the surface and the molecules.

AFM images were simulated based on the probe-particle model [32,45], which takes into account van der Waals (vdW) and

electrostatic interactions between the tip and the sample. The calculations were performed varying the effective charge of the probe particle in order to obtain the best possible agreement between the experimental findings and the simulated AFM images. The lateral stiffness was set to $k = 0.25$ N/m. The correlation of the experimental evidence and theory permit us to understand the nature and origin of the chemical contrast.

Supporting Information

Supporting Information File 1

Additional computational data.
[https://www.beilstein-journals.org/bjnano/content/supplementary/2190-4286-10-30-S1.pdf]

Acknowledgements

This work was supported by the Operational Programme Research, Development and Education financed by European Structural and Investment Funds and the Czech Ministry of Education, Youth and Sports (Project No. SOLID21 CZ.02.1.01/0.0/0.0/16_019/0000760). M. S. gratefully acknowledges the grant no. 17-24210Y provided by the Czech grant agency. J. K. gratefully acknowledges the MEYS SAFMAT CZ.02.1.01/0.0/0.0/16_013/0001406, LO1409 and LM2015088 projects. Access to computing and storage facilities owned by parties and projects contributing to the National Grid Infrastructure MetaCentrum provided under the programme "Projects of Large Research, Development, and Innovations Infrastructures" (CESNET LM2015042), is greatly appreciated.

ORCID® iDs

Pingo Mutombo - https://orcid.org/0000-0002-8175-7587
Jack Hellerstedt - https://orcid.org/0000-0003-2282-8223
Jaromír Kopeček - https://orcid.org/0000-0002-9337-4639
Martin Švec - https://orcid.org/0000-0003-0369-8144

References

1. Gross, L.; Mohn, F.; Moll, N.; Liljeroth, P.; Meyer, G. *Science* **2009,** *325,* 1110–1114. doi:10.1126/science.1176210
2. Gross, L.; Mohn, F.; Moll, N.; Meyer, G.; Ebel, R.; Abdel-Mageed, W. M.; Jaspars, M. *Nat. Chem.* **2010,** *2,* 821–825. doi:10.1038/nchem.765
3. Hanssen, K. Ø.; Schuler, B.; Williams, A. J.; Demissie, T. B.; Hansen, E.; Andersen, J. H.; Svenson, J.; Blinov, K.; Repisky, M.; Mohn, F.; Meyer, G.; Svendsen, J.-S.; Ruud, K.; Elyashberg, M.; Gross, L.; Jaspars, M.; Isaksson, J. *Angew. Chem., Int. Ed.* **2012,** *51,* 12238–12241. doi:10.1002/anie.201203960
4. Schuler, B.; Collazos, S.; Gross, L.; Meyer, G.; Pérez, D.; Guitián, E.; Peña, D. *Angew. Chem.* **2014,** *126,* 9150–9152. doi:10.1002/ange.201403707
5. Pavliček, N.; Schuler, B.; Collazos, S.; Moll, N.; Pérez, D.; Guitián, E.; Meyer, G.; Peña, D.; Gross, L. *Nat. Chem.* **2015,** *7,* 623–628. doi:10.1038/nchem.2300
6. Gross, L.; Mohn, F.; Moll, N.; Schuler, B.; Criado, A.; Guitian, E.; Pena, D.; Gourdon, A.; Meyer, G. *Science* **2012,** *337,* 1326–1329. doi:10.1126/science.1225621
7. Mohn, F.; Gross, L.; Moll, N.; Meyer, G. *Nat. Nanotechnol.* **2012,** *7,* 227–231. doi:10.1038/nnano.2012.20
8. Hapala, P.; Švec, M.; Stetsovych, O.; van der Heijden, N. J.; Ondráček, M.; van der Lit, J.; Mutombo, P.; Swart, I.; Jelínek, P. *Nat. Commun.* **2016,** *7,* 11560. doi:10.1038/ncomms11560
9. Albrecht, F.; Repp, J.; Fleischmann, M.; Scheer, M.; Ondráček, M.; Jelínek, P. *Phys. Rev. Lett.* **2015,** *115,* 076101. doi:10.1103/physrevlett.115.076101
10. Moreno, C.; Stetsovych, O.; Shimizu, T. K.; Custance, O. *Nano Lett.* **2015,** *15,* 2257–2262. doi:10.1021/nl504182w
11. Albrecht, F.; Pavliček, N.; Herranz-Lancho, C.; Ruben, M.; Repp, J. *J. Am. Chem. Soc.* **2015,** *137,* 7424–7428. doi:10.1021/jacs.5b03114
12. Albrecht, F.; Bischoff, F.; Auwärter, W.; Barth, J. V.; Repp, J. *Nano Lett.* **2016,** *16,* 7703–7709. doi:10.1021/acs.nanolett.6b03769
13. Schuler, B.; Meyer, G.; Peña, D.; Mullins, O. C.; Gross, L. *J. Am. Chem. Soc.* **2015,** *137,* 9870–9876. doi:10.1021/jacs.5b04056
14. Schuler, B.; Fatayer, S.; Meyer, G.; Rogel, E.; Moir, M.; Zhang, Y.; Harper, M. R.; Pomerantz, A. E.; Bake, K. D.; Witt, M.; Peña, D.; Kushnerick, J. D.; Mullins, O. C.; Ovalles, C.; van den Berg, F. G. A.; Gross, L. *Energy Fuels* **2017,** *31,* 6856–6861. doi:10.1021/acs.energyfuels.7b00805
15. Riss, A.; Paz, A. P.; Wickenburg, S.; Tsai, H.-Z.; De Oteyza, D. G.; Bradley, A. J.; Ugeda, M. M.; Gorman, P.; Jung, H. S.; Crommie, M. F.; Rubio, A.; Fischer, F. R. *Nat. Chem.* **2016,** *8,* 678–683. doi:10.1038/nchem.2506
16. de Oteyza, D. G.; Gorman, P.; Chen, Y.-C.; Wickenburg, S.; Riss, A.; Mowbray, D. J.; Etkin, G.; Pedramrazi, Z.; Tsai, H.-Z.; Rubio, A.; Crommie, M. F.; Fischer, F. R. *Science* **2013,** *340,* 1434–1437. doi:10.1126/science.1238187
17. Shiotari, A.; Nakae, T.; Iwata, K.; Mori, S.; Okujima, T.; Uno, H.; Sakaguchi, H.; Sugimoto, Y. *Nat. Commun.* **2017,** *8,* 16089. doi:10.1038/ncomms16089
18. Rogers, C.; Chen, C.; Pedramrazi, Z.; Omrani, A. A.; Tsai, H.-Z.; Jung, H. S.; Lin, S.; Crommie, M. F.; Fischer, F. R. *Angew. Chem., Int. Ed.* **2015,** *54,* 15143–15146. doi:10.1002/anie.201507104
19. Stetsovych, O.; Švec, M.; Vacek, J.; Chocholoušová, J. V.; Jančařík, A.; Rybáček, J.; Kosmider, K.; Stará, I. G.; Jelínek, P.; Starý, I. *Nat. Chem.* **2017,** *9,* 213–218. doi:10.1038/nchem.2662
20. de la Torre, B.; Švec, M.; Hapala, P.; Redondo, J.; Krejčí, O.; Lo, R.; Manna, D.; Sarmah, A.; Nachtigallová, D.; Tuček, J.; Błoński, P.; Otyepka, M.; Zbořil, R.; Hobza, P.; Jelínek, P. *Nat. Commun.* **2018,** *9,* 2831. doi:10.1038/s41467-018-05163-y
21. Hauptmann, N.; Mohn, F.; Gross, L.; Meyer, G.; Frederiksen, T.; Berndt, R. *New J. Phys.* **2012,** *14,* 073032. doi:10.1088/1367-2630/14/7/073032
22. Sweetman, A. M.; Jarvis, S. P.; Sang, H.; Lekkas, I.; Rahe, P.; Wang, Y.; Wang, J.; Champness, N. R.; Kantorovich, L.; Moriarty, P. *Nat. Commun.* **2014,** *5,* 3931. doi:10.1038/ncomms4931
23. Shiotari, A.; Odani, T.; Sugimoto, Y. *Phys. Rev. Lett.* **2018,** *121,* 116101. doi:10.1103/physrevlett.121.116101
24. Mohn, F.; Schuler, B.; Gross, L.; Meyer, G. *Appl. Phys. Lett.* **2013,** *102,* 073109. doi:10.1063/1.4793200

25. Schuler, B.; Liu, W.; Tkatchenko, A.; Moll, N.; Meyer, G.; Mistry, A.; Fox, D.; Gross, L. *Phys. Rev. Lett.* **2013,** *111,* 106103. doi:10.1103/physrevlett.111.106103
26. Mönig, H.; Hermoso, D. R.; Díaz Arado, O.; Todorović, M.; Timmer, A.; Schüer, S.; Langewisch, G.; Pérez, R.; Fuchs, H. *ACS Nano* **2016,** *10,* 1201–1209. doi:10.1021/acsnano.5b06513
27. Peng, J.; Guo, J.; Hapala, P.; Cao, D.; Ma, R.; Cheng, B.; Xu, L.; Ondráček, M.; Jelínek, P.; Wang, E.; Jiang, Y. *Nat. Commun.* **2018,** *9,* 122. doi:10.1038/s41467-017-02635-5
28. Jelínek, P. *J. Phys.: Condens. Matter* **2017,** *29,* 343002. doi:10.1088/1361-648x/aa76c7
29. Wagner, C.; Green, M. F. B.; Leinen, P.; Deilmann, T.; Krüger, P.; Rohlfing, M.; Temirov, R.; Tautz, F. S. *Phys. Rev. Lett.* **2015,** *115,* 026101. doi:10.1103/physrevlett.115.026101
30. Chiang, C.-l.; Xu, C.; Han, Z.; Ho, W. *Science* **2014,** *344,* 885–888. doi:10.1126/science.1253405
31. de la Torre, B.; Švec, M.; Foti, G.; Krejčí, O.; Hapala, P.; Garcia-Lekue, A.; Frederiksen, T.; Zbořil, R.; Arnau, A.; Vázquez, H.; Jelínek, P. *Phys. Rev. Lett.* **2017,** *119,* 166001. doi:10.1103/physrevlett.119.166001
32. Hapala, P.; Kichin, G.; Wagner, C.; Tautz, F. S.; Temirov, R.; Jelínek, P. *Phys. Rev. B* **2014,** *90,* 085421. doi:10.1103/physrevb.90.085421
33. Temirov, R.; Soubatch, S.; Neucheva, O.; Lassise, A. C.; Tautz, F. S. *New J. Phys.* **2008,** *10,* 053012. doi:10.1088/1367-2630/10/5/053012
34. Wagner, C.; Temirov, R. *Prog. Surf. Sci.* **2015,** *90,* 194–222. doi:10.1016/j.progsurf.2015.01.001
35. Kokalj, A.; Matsushima, T. *J. Chem. Phys.* **2005,** *122,* 034708. doi:10.1063/1.1829652
36. Murray, J. S.; Politzer, P. *Wiley Interdiscip. Rev.: Comput. Mol. Sci.* **2011,** *1,* 153–163. doi:10.1002/wcms.19
37. Hirshfeld, F. L. *Theor. Chim. Acta* **1977,** *44,* 129–138. doi:10.1007/bf00549096
38. Lantz, M. A. *Science* **2001,** *291,* 2580–2583. doi:10.1126/science.1057824
39. Giessibl, F. J. *Appl. Phys. Lett.* **2001,** *78,* 123–125. doi:10.1063/1.1335546
40. Horcas, I.; Fernández, R.; Gómez-Rodríguez, J. M.; Colchero, J.; Gómez-Herrero, J.; Baro, A. M. *Rev. Sci. Instrum.* **2007,** *78,* 013705. doi:10.1063/1.2432410
41. Momma, K.; Izumi, F. *J. Appl. Crystallogr.* **2011,** *44,* 1272–1276. doi:10.1107/s0021889811038970
42. Blum, V.; Gehrke, R.; Hanke, F.; Havu, P.; Havu, V.; Ren, X.; Reuter, K.; Scheffler, M. *Comput. Phys. Commun.* **2009,** *180,* 2175–2196. doi:10.1016/j.cpc.2009.06.022
43. Tkatchenko, A.; Scheffler, M. *Phys. Rev. Lett.* **2009,** *102,* 073005. doi:10.1103/physrevlett.102.073005
44. van Lenthe, E.; van Leeuwen, R.; Baerends, E. J.; Snijders, J. G. *Int. J. Quantum Chem.* **1996,** *57,* 281–293. doi:10.1002/(sici)1097-461x(1996)57:3<281::aid-qua2>3.0.co;2-u
45. Hapala, P.; Temirov, R.; Tautz, F. S.; Jelínek, P. *Phys. Rev. Lett.* **2014,** *113,* 226101. doi:10.1103/physrevlett.113.226101

BEILSTEIN JOURNAL OF NANOTECHNOLOGY

Supporting Information

for

Nitrous oxide as an effective AFM tip functionalization: a comparative study

Taras Chutora, Bruno de la Torre, Pingo Mutombo, Jack Hellerstedt, Jaromír Kopeček, Pavel Jelínek and Martin Švec

Beilstein J. Nanotechnol. **2019,** *10,* 315–321. doi:10.3762/bjnano.10.30

Additional computational data

Calculated force and energy

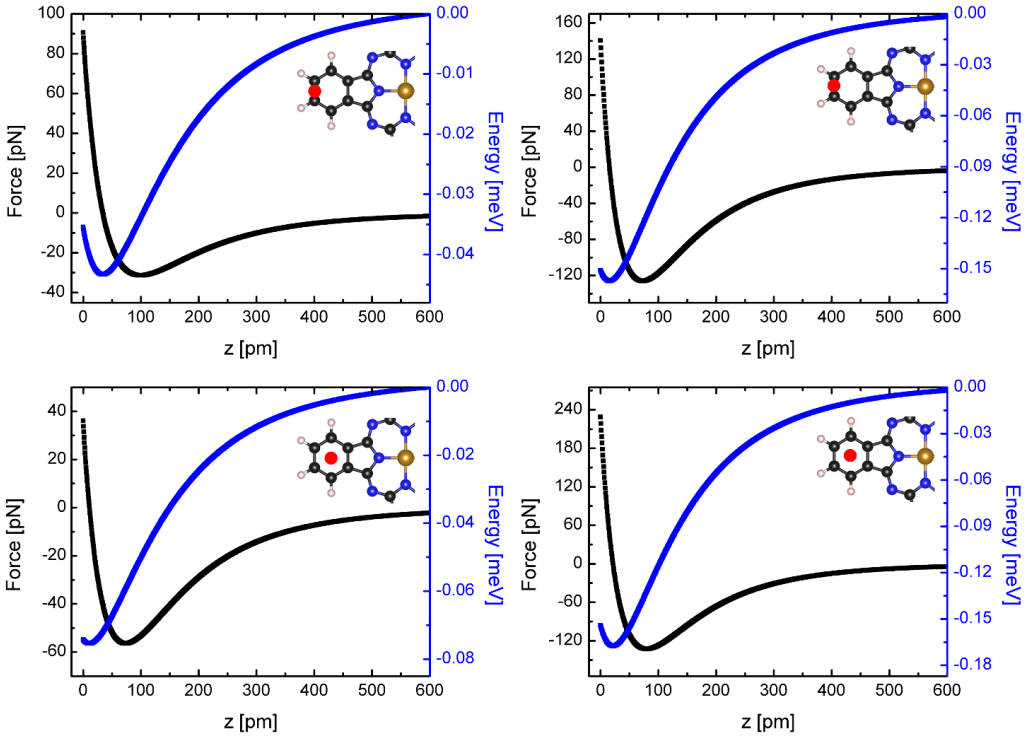

Figure S1: Deconvoluted force and energy from the experimentally obtained frequency shift as a function of the tip–sample distance for CO (left side) and N_2O tips (right side). The long-range component measured on bare Au(111) was subtracted prior to calculation from the total interaction curve. The measurements were acquired above an outer C–C bond and above a hollow site of a peripheral benzene of the FePc molecule (position indicated with a red dot in the inset of each plot). The force and energy were calculated using the Giessibl method [1].

References

[1] Giessibl F. J. *Appl. Phys. Lett*. **2001,** *78,* 123–125. doi:10.1063/1.1335546

4.3 On-surface design of ethynylene linked anthracene polymers

On-surface synthesis has become a very powerful technique for the formation of conjugated functional nanostructures which are not achievable by standard wet chemistry[125;126] due to solubility limitations. This has enabled the fabrication of graphene nanoribbons[46], organometallic chains[127] and covalent polymers[128] by using specifically designed molecular precursors. Such materials have promising applications in nanoelectronics[129] and can be used for light emitting devices[130]. This chapter focusses on an unprecedented on-surface synthesis protocol to design poly (p-anthracene ethynylene) molecular wires on Au(111) surface.

4.3.1 On-surface synthesis of polymers

The investigation of on-surface reactions[131] has received tremendous attention mainly due to the increasing demand for novel materials with versatile and tunable properties for the construction of electronic devices[129]. The most commonly pathway is the Ullmann type reaction which was first applied to fabricate 2D covalently bonded nanostructures on a Au(111) surface[38].

C–C coupling is a complex surface reaction[131] which requires preparation of specific molecular precursors. Usually, it is done by adding halogen atoms such as Br or I to aryl groups. The molecular precursor is usually deposited on coinage metal surfaces where the reaction is typically induced by thermal annealing. Importantly, the activation energy of the C-X bond should not be higher than the desorption barrier of the precursor molecule. This factor introduces additional limitations for the synthesis of molecular precursors. Therefore, the molecular weight and chemical composition of the precursor monomer must be considered. However, in the case when the molecules are weakly coupled to the substrate and have a small molecular weight, annealing simply leads to precursor desorption. In this case the reaction can be induced with a simple bias pulse (electron injection through a metal tip)[21] without unintentional desorption of the molecules from the surface. The final structure of the polymers and oligomers formed via on-surface chemical reactions can be influenced by the structure and chemical composition of the precursor molecule. For example, the precursor monomer which has two or four hydrogens substituted with halogen atoms usually produces one-dimensional covalently bonded polymers[38 132]. Moreover, the electronic properties of the final polymer can be further modified by introducing donor and acceptor units in the precursor[133].

Generally, the covalently bonded polymers can be formed in two ways: (1) the precursor molecules can be deposited to the surface at RT and subsequently an-

nealed to the desired temperature or (2) the precursor molecule can be deposited on a "hot" substrate to induce the reaction. In the first method, after the room temperature deposition the molecule tends to form self-assembled islands which limit monomer diffusion during the reaction phase. In this way, the molecule will start to form dimers and small chains which will eventually fuse to each other. In the second way, the single monomer has a higher diffusion rate which can eventually lead to attachment to already formed chains[134].

4.3.2 Characterization of anthracene polymers by means of AFM and STS

Recently, the fabrication and study of π-conjugated polymers has received considerable attention mainly because of their unique electronic properties and possible application in nanoelectronics. Several publications have appeared in recent years reporting on-surface formation of various oligocene derivatives and polymers which notably have large bandgaps such as poly(meta-phenylene)-like (3.7 eV)[135] and poly(para-phenylene) (3.2 eV)[127]. Although there is tremendous potential of acene for plastic optoelectronics, the fabrication of high-quality π-conjugated polymers with small bandgaps based on oligoacene building units has not been achieved.

In paper III on page 58 we report the on-surface synthesis of long molecular wires exclusively based on anthracene building blocks. To fabricate covalently bonded polymers, we use a quinoid anthracene precursor which has four hydrogens substituted with four bromine atoms as shown in Fig. 4.5. The molecular precursor (11,11,12,12-tetrabromoanthraquinodimethane) used in our experiments can be fabricated using the procedure described elsewhere[136].

First, the precursor molecules were deposited on the Au(111) surface at RT using a home-build molecular evaporator. STM inspection revealed large, close-packed, self-assembled molecular islands which mainly formed near step edges. Close STM/AFM inspection in combination with AFM simulations and DFT calculations revealed two different adsorption configurations of the bromine group towards and away from the surface as shown in Fig. SI1 (page 66).

Second, to induce the reaction the sample was annealed to 500 K which lead to the formation of anthracene-based polymers, with a measured electronic bandgap of 1.5 eV. Using high-resolution nc-AFM with a CO functionalized tip we established the nature of the ethynylene bridge bond between anthracene moieties. With the help of complementary theoretical simulations, we successfully identified the mechanism of the chemical reaction. The three major steps: debromination, diffusion of the dehalogenated species, and homocoupling which enabled polymerization, are depicted in Fig. 4.5

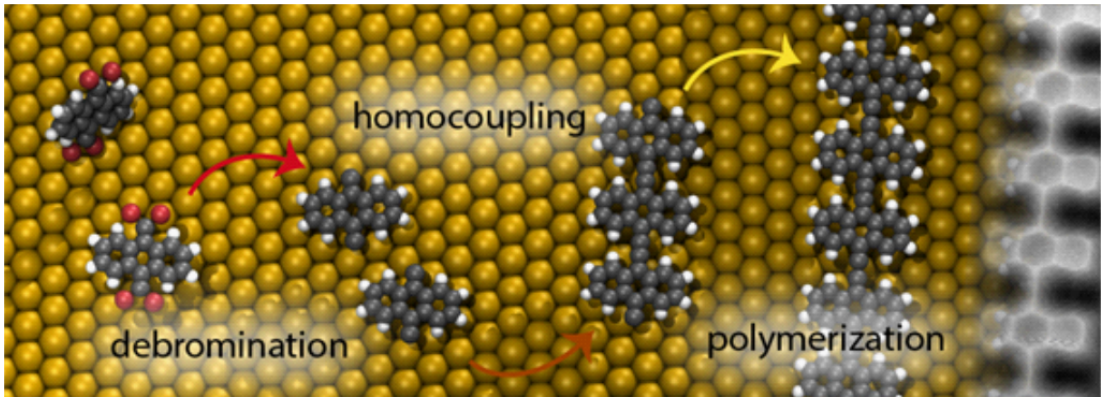

Figure 4.5: Representation of the thermal reaction steps which enable polymerization, namely debromination followed by homocoupling which leads to polymerization

My contribution to paper III can be summarized as follows: I performed nc-AFM and STM measurements as well as sample preparation. During the SPM measurements, I worked to determine the adsorption characterization of the quinoid anthracene precursors on the Au(111) surface. I also participated in data processing and analysis.

Surface Chemistry

International Edition: DOI: 10.1002/anie.201814154
German Edition: DOI: 10.1002/ange.201814154

On-Surface Synthesis of Ethynylene-Bridged Anthracene Polymers

Ana Sánchez-Grande, Bruno de la Torre, José Santos, Borja Cirera, Koen Lauwaet, Taras Chutora, Shayan Edalatmanesh, Pingo Mutombo, Johanna Rosen, Radek Zbořil, Rodolfo Miranda, Jonas Björk, Pavel Jelínek,* Nazario Martín,* and David Écija**

Abstract: *Engineering low-band-gap π-conjugated polymers is a growing area in basic and applied research. The main synthetic challenge lies in the solubility of the starting materials, which precludes advancements in the field. Here, we report an on-surface synthesis protocol to overcome such difficulties and produce poly(p-anthracene ethynylene) molecular wires on Au(111). To this aim, a quinoid anthracene precursor with $=CBr_2$ moieties is deposited and annealed to 400 K, resulting in anthracene-based polymers. High-resolution nc-AFM measurements confirm the nature of the ethynylene-bridge bond between the anthracene moieties. Theoretical simulations illustrate the mechanism of the chemical reaction, highlighting three major steps: dehalogenation, diffusion of surface-stabilized carbenes, and homocoupling, which enables the formation of an ethynylene bridge. Our results introduce a novel chemical protocol to design π-conjugated polymers based on oligoacene precursors and pave new avenues for advancing the emerging field of on-surface synthesis.*

The design and study of π-conjugated polymers has received great attention during the last decades due to the relevant optical and electronic properties that emerge from the delocalization of the π-electrons. Such materials find use in different applications including light-emitting devices, solar cells, organic field-effect transistors, photocatalysis, and biosensors.[1–3] However, despite great synthetic advances in the field, there are enormous efforts coming from emerging areas of chemistry targeting to overcome the accompanying limitation of solubility, which precludes highly interesting conjugated nanomaterials to be synthesized by wet chemistry.[2,3]

On-surface synthesis has become a powerful discipline to design many novel molecular compounds, polymers, and nanomaterials with atomistic precision,[4–12] some of them not accessible by standard synthetic methods. Additionally, on-surface chemistry enables the structural and electronic characterization of the designed products with advanced surface-science techniques.[10,13,14] Recently, and within the scope of on-surface synthesis, particular success has been achieved in the field of oligoacenes, where anthracene,[15,16] tetracene,[17] hexacene,[18] heptacene,[19,20] nonacene,[21] decacene,[22] and undecacene[20] precursors have been deposited on coinage metals and transformed into oligoacene derivatives through external stimuli. However, despite the great potential of such acene compounds for plastic optoelectronics, the design of high-quality π-conjugated polymers exclusively based on oligoacene building units remains difficult. On-surface chemistry opens the gate to obtain acene-based polymers. Although their predicted intrinsic insolubility may hinder their practical application at first glance, state-of-the-art substrate-to-substrate transfer techniques already permit the implementation of highly insoluble nanomaterials into molecular electronic devices.[23]

Here, we report a comprehensive scanning tunneling microscopy (STM), non-contact atomic force microscopy (nc-AFM), and density functional theory (DFT) study of the on-surface synthesis of poly(*p*-anthracene ethynylene) molecular wires on Au(111). Our novel chemical approach is based on

[*] A. Sánchez-Grande, Dr. J. Santos, Dr. B. Cirera, K. Lauwaet, Prof. R. Miranda, Prof. N. Martín, Prof. D. Écija
IMDEA Nanociencia, C/ Faraday 9
Ciudad Universitaria de Cantoblanco
28049 Madrid (Spain)
E-mail: nazmar@quim.ucm.es
david.ecija@imdea.org

Dr. B. de la Torre, T. Chutora, Prof. R. Zbořil, Dr. P. Jelínek
Regional Centre of Advanced Technologies and Materials
Palacký University Olomouc
Šlechtitelů 27, 78371 Olomouc (Czech Republic)

Dr. B. de la Torre, S. Edalatmanesh, P. Mutombo, Dr. P. Jelínek
Institute of Physics, The Czech Academy of Sciences
Cukrovarnická 10, 16200 Prague 6 (Czech Republic)
E-mail: jelinekp@fzu.cz

Prof. J. Rosen, Dr. J. Björk
Department of Physics, Chemistry and Biology, IFM
Linköping University
58183 Linköping (Sweden)
E-mail: jonas.bjork@liu.se

Prof. R. Miranda
Departamento de Física de la Materia Condensada
Facultad de Ciencias, Universidad Autónoma de Madrid
28049 Madrid (Spain)

Prof. N. Martín
Departamento de Química Orgánica
Facultad de Ciencias Químicas, Universidad Complutense
28040 Madrid (Spain)

Supporting information and the ORCID identification number(s) for the author(s) of this article can be found under: https://doi.org/10.1002/anie.201814154.

the dehalogenation, homocoupling, and aromatization of a quinoid anthracene precursor endowed with $=CBr_2$ moieties at their 9- and 10- positions. The deposition of this precursor (11,11,12,12-tetrabromoanthraquinodimethane), abbreviated **4BrAn**, on Au(111) gives rise to a close-packed assembly. Annealing to 400 K enables debromination, and, after diffusion, long molecular wires based on ethynylene bridges are formed, which is unambiguously confirmed by the excellent agreement of the experimental non-contact atomic force microscopy measurements with the theoretical simulations. A final step of annealing to 500 K induces the removal of peripheral bromine atoms and the subsequent emergence of isolated, high-quality, robust, and long anthracene-based polymers. Scanning probe microscopy reveals the shape and energy of the frontier orbitals, which leads to a band gap of 1.5 eV. The theoretical study of the reaction pathways, complemented by high-resolution scanning probe microscopy measurements with a CO tip, illustrates that the homocoupling process is based on an efficient dehalogenation of the molecular precursors and diffusion of the surface-stabilized carbenes, finally leading to coupling and aromatization of the polymeric chain.

Our study introduces a novel strategy to homocouple anthracene precursors, which could be extended to the whole family of oligoacenes. We envision that these results will notably contribute to the development of the field of on-surface chemistry while providing novel avenues to design π-conjugated polymers in the form of molecular chains, with a special emphasis in low-band gap nanomaterials.

Scheme 1 illustrates the suitably synthesized molecular precursor **4BrAn** used for building up the desired anthracene-based polymers. Notably, it incorporates $=CBr_2$ moieties at the positions 9 and 10 of the anthraquinone backbone to

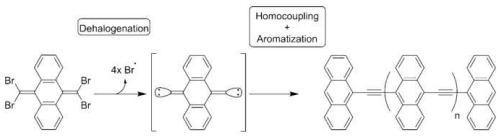

Scheme 1. Reaction sequence of the **4BrAn** (11,11,12,12-tetrabromoanthraquinodimethane) precursor after deposition on Au(111) and subsequent annealing.

control the dehalogenation and subsequent homocoupling upon thermal annealing[24] by undergoing an unprecedented reaction pathway as detailed below. The deposition of a submonolayer coverage of **4BrAn** on Au(111) results in the formation of close-packed islands in a rectangular unit cell (Supporting Information, Figure SI1). At this stage of the reaction, no isolated bromine atoms are detected on the surface, which highlights the integrity of the molecular precursors. A first step of annealing to 400 K leads to the emergence of long polymeric wires (Figure 1 a and Supporting Information, Figure SI2). The molecular precursors have now lost their bromine atoms, which can be found either forming 1D atomic chains on the surface or located in between the polymers, directing their parallel alignment (Figure 1 a and

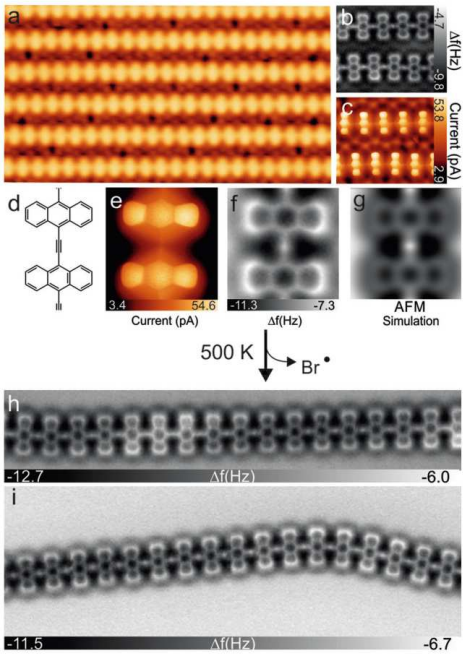

Figure 1. a) Large-scale STM image of the parallelly aligned ethynylene-linked anthracene polymers coexisting with bromine atoms after deposition of a submonolayer coverage of **4BrAn** on Au(111) and subsequent annealing at 400 K ($V_{bias}=100$ mV, $I=10$ pA, image size $=14.9\times8.4$ nm^2). b) Magnified constant-height nc-AFM and c) STM image (size $=3.6\times3.2$ nm^2) of a selected area of (a) acquired at the same time. d) Chemical structure of an ethynylene-bridged anthracene moiety. e) Constant-height STM and f) nc-AFM image resolving the ethylene bond, which matches very well with g) a nc-AFM simulation (1.3×1.3 nm^2). h) Constant-height nc-AFM image of a linear (size $=12\times2$ nm^2) and i) a curved (size $=12\times4$ nm^2) ethynylene-linked anthracene polymer after annealing (a) to 500 K.

Supporting Information, Figure SI2). As illustrated by high-resolution AFM imaging with a CO tip, the polymers are formed by anthracene moieties that are linked by ethynylene bridges. At an adequate distance between tip and sample, the triple bond can be unambiguously distinguished as a bright protrusion (Figure 1 b,f and Supporting Information, Figure SI3), which is in agreement with recently synthesized poly(*p*-phenylene ethynylene) molecular wires on Au(111).[25] The excellent match between the experimental and simulated AFM images confirms the bridge as an ethynylene moiety (see Figure 1 f,g), which differs from the previously reported formation of cumulene bridges by dehalogenative homocoupling of alkenyl gem-dibromides.[24]

At this step of annealing, a small fraction of ethynylene-bridged anthracene dimers and trimers is present. High-resolution AFM resolves the conformation of these oligomers (Supporting Information, Figure SI4). The dimers are not planar due to the presence of terminal C atoms of the $=CBr_2$

moiety at each terminus of the dimer, which strongly interact with the substrate. This assumption is confirmed by the excellent agreement between the experimental and the simulated images. Notably, the trimer features a planar central anthracene, whereas the two terminal moieties are bent due to the interaction of the carbon termini with the gold support. Statistically, 90% of the molecular precursors are incorporated into the polymeric wires after a typical annealing of 30 min at 400 K. The edge of these wires always has the same C termination, resulting in terminal anthracene moieties that are bent towards the surface (Supporting Information, Figure SI4).

Importantly, the dehalogenated species diffuse as surface-stabilized carbenes until they connect and form the ethynylene-bridged anthracene polymers. This behavior is also typically encountered in the homocoupling of aryl halides on Au(111).[24–27] It is worth to highlight that the formation of anthracene polymers results in the aromatization of the quinoid precursors, since ethynylene bridges are preferred over cumulene bridges, regardless of the length of the polymer. The pro-aromatic nature of the quinoid precursor seems to be the driving force leading to the aromatization of the anthraquinoid core through electronic rearrangement. This scenario is fully supported by DFT calculations of the total energy, which also reveal the presence of the ethynylene bridges. The optimized structure of the polymer is almost planar, located 3.4 Å above the Au(111) substrate, and dominantly bonded by dispersion forces.

Further annealing of the sample to 500 K enables the desorption of the remaining bromine atoms, giving rise to isolated, long, and very high-quality ethynylene-bridged anthracene polymers (Figure 1h and Supporting Information, Figure SI5). Notably, the wires exhibit a remarkable degree of flexibility, allowing open curvatures up to 130° through minor bending of the ethynylene links (see Figure 1i). Additionally, the bond is robust and withstands tip-induced lateral manipulations, which results in a change in curvature of the polymer while preserving its chemical structure (Supporting Information, Figure SI6), thus indicating promising prospects for flexible electronics.

At this stage of annealing, the major termini of the polymers have lost the remaining carbon and are passivated by residual atomic hydrogen, as illustrated in Figures SI7 and SI8 (Supporting Information). Defects within the molecular chain are rare and structurally perfect ethynylene-bridged anthracene polymers with a length up to 30 nm are frequently observed.

To elucidate the electronic structure of the π-conjugated polymers, we simulated a freestanding polymer using the B3LYP density functional (Figure 2a), which reveals the presence of dispersive valence (VB) and conduction (CB) bands separated by a band gap of about 1.4 eV. The calculated projected density of states of the polymer on Au(111) indicates that the dispersion of both the CB and the VB remains practically unaltered with only a slight reduction of the band gap due to additional electron screening from the metal substrate (Supporting Information, Figure SI9).

Spatially resolved scanning tunneling spectra were recorded over the molecular wires and the clean Au(111)

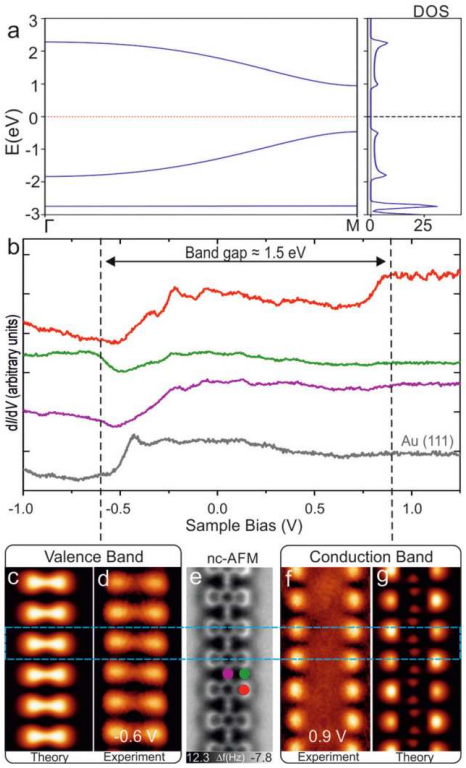

Figure 2. a) Calculated (B3LYP) electronic structure of a free-standing ethynylene-linked anthracene polymer. b) dI/dV scanning tunneling spectra of the polymer on Au(111) at selected points indicated by the colored dots in (e). c) Simulated STM image of the valence band. d) Experimental dI/dV map of the valence band at constant current. e) nc-AFM image of an ethynylene-linked anthracene polymer (size = 1.9×4.3 nm^2). f) Experimental dI/dV map of the conduction band at constant current. g) Simulated STM image of the conduction band.

surface. As illustrated in Figure 2b, two frontier resonances can be distinguished at −0.6 eV (green curve) and 0.9 eV (red curve), which are tentatively assigned to the VB and CB edges, respectively. Note that the VB and CB edges are not located at the same position in space; the VB edge appears in between the anthracene moieties and the CB edge on top of them. Within the band gap, the downshifted surface state convoluted with tip states is observed. In agreement with the point spectra, the dI/dV map at the VB edge (Figure 2d) does not show maxima over the anthracene moieties, but shows states over the bridges and, remarkably, also on the voids adjacent to the links. The dI/dV map of the CB, on the contrary, shows states located over the edges of the anthracene moieties (Figure 2f). The calculated dI/dV maps (Figure 2c,g) match very well with the experiment, validating the

character of the band structure predicted by the DFT calculations. Analysis of the experimental STS spectra reveals a band gap of 1.5 eV. The polymer thereby shows a band gap circa 2 eV smaller than the 3.6 eV value recently reported for the HOMO–LUMO gap of a pure anthracene monomer on Au(111).[28] Notably, our results highlight the versatility of on-surface synthesis for designing polymers with varied band gaps going from large values in the case of poly(*meta*-phenylene)-like (3.7 eV)[29] or poly(*para*-phenylene) (3.2 eV)[30] polymers to small quantities (1.5 eV) as reported here.

Finally, we studied the reaction pathway for the homocoupling of **4BrAn** on Au(111) with DFT-based transition state theory. The most favorable mechanism in which complete dehalogenation of the molecule initiates the reaction is shown in Figure 3. An alternative reaction pathway is

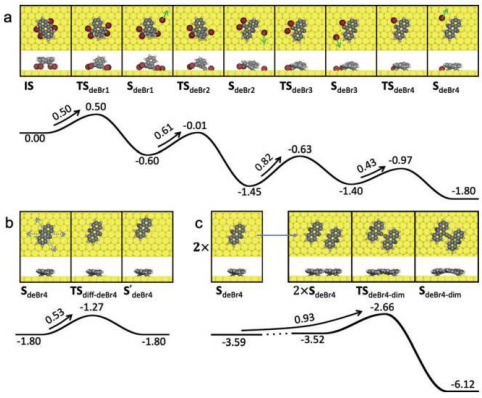

Figure 3. a–c) Energetically most favorable reaction pathway for the dehalogenative homocoupling of **4BrAn** precursors on Au(111), depicting top and side views of local minima (**S**$_x$) and transition states (**TS**$_x$) with the corresponding energy profile with respect to the initial state (**IS**): (a) Initial dehalogenation cascade, (b) diffusion of the dehalogenated molecule, and (c) coupling of two dehalogenated molecules. Energies in eV.

illustrated in Figure SI10 (Supporting Information) and discarded due to higher activation barriers. Removal of the third bromine has the highest activation energy (0.82 eV) and the full dehalogenation is highly exothermic with a reaction energy of −1.80 eV. The dehalogenated species (**S**$_{deBr4}$) can then diffuse along two of the main directions of the substrate (Figure 3b) with a barrier of 0.53 eV. Finally, the activation energy for two molecules to approach each other and couple (Figure 3c) is 0.93 eV, similar to the dehalogenation step with the highest barrier. The coupling is a second-order process and one may expect the occurrence of non-coupled **S**$_{deBr4}$ species. However, this would require sufficient time for a thermal equilibration of **S**$_{deBr4}$ while avoiding coupling, that is, the excess heat released during dehalogenation could explain the absence of monomers following the initial annealing. Notably, the coupling between two molecules is highly exothermic, as expected for the linking between two surface-stabilized carbenes.[26]

In conclusion, we report a strategy for the on-surface synthesis of ethynylene-bridged anthracene π-conjugated polymers. To this aim, we rely on the combination of scanning tunneling microscopy and non-contact atomic force microscopy complemented with state-of-the-art density functional theory. The deposition of quinoid moieties functionalized with $=CBr_2$ termini on Au(111) and subsequent annealing enable a unique reaction pathway. A first annealing step to 400 K results in the detachment of the bromine atoms and the diffusion of the resulting surface-stabilized carbenes until they couple, forming high-quality 1D molecular wires. Non-contact atomic force microscopy combined with simulations elucidates the structure of these ribbons as unprecedented ethynylene-bridged anthracene polymers. A second annealing step to 500 K enables the desorption of bromine, giving rise to long flexible polymers that preserve the integrity of the ethynylene bridge. These polymers exhibit a low experimental band gap of 1.5 eV, which is of potential relevance for near-infrared applications.

Importantly, preliminar results on Ag(111) also reveal the formation of ethynylene-linked anthracene polymers, thus expanding the scope of the reported reaction to other surfaces. Our results herald novel pathways to engineer π-conjugated polymers on surfaces, addressing the relevant family of acenes and thus contributing to the development of the field of on-surface chemistry and guiding the design of modern low-band-gap polymers.

Acknowledgements

This work was supported by the Comunidad de Madrid (Projects Y2018/NMT-4783 (QUIMTRONIC-CM), S2013/MIT-3007 (MAD2D), and S2018/NMT (NANOMAGCOST-CM)), the European Research Council (ERC-320441-Chirallcarbon and ERC-766555-ELECNANO), the Spanish Ramón y Cajal programme (No. RYC-2012-11133), and the MINECO of Spain (Projects FIS 2015-67287-P, CTQ2017-83531-R, and CTQ2016-81911-REDT). The IMDEA Nanociencia acknowledges support from the Severo Ochoa Programme for Centers of Excellence in R&D (MINECO, Grant SEV-2016-0686). P.J. acknowledges support from the Praemium Academie of the Academy of Science of the Czech Republic, MEYS LM2015087 and GACR 18–09914S, and the Operational Programme Research, Development, and Education financed by the European Structural and Investment Funds and the Czech Ministry of Education, Youth, and Sports (Project No. CZ.02.1.01/0.0/0.0/16 019/0000754). The authors acknowledge the support from the Czech Science Foundation under Project No. 19-27454X. J.B. and J.R. acknowledge financial support from the Swedish Research Council (642-2013-2080), the Swedish Strategic Research Area in Materials Science on Functional Materials at Linköping University (Faculty Grant SFO-Mat-LiU No 2009 00971), and computational resources at the National Supercomputer Centre, Sweden, allocated by SNIC. The authors thank Dr. Oliver Gröning for fruitful discussions.

Conflict of interest

The authors declare no conflict of interest.

Keywords: acenes · low-band-gap semiconductors · polymers · scanning probe microscopy · surface chemistry

How to cite: *Angew. Chem. Int. Ed.* **2019**, *58*, 6559–6563
Angew. Chem. **2019**, *131*, 6631–6635

[1] A. J. Heeger, *Angew. Chem. Int. Ed.* **2001**, *40*, 2591–2611; *Angew. Chem.* **2001**, *113*, 2660–2682.
[2] X. Guo, M. Baumgarten, K. Müllen, *Prog. Polym. Sci.* **2013**, *38*, 1832–1908.
[3] A. Facchetti, *Chem. Mater.* **2011**, *23*, 733–758.
[4] L. Grill, M. Dyer, L. Lafferentz, M. Persson, M. V. Peters, S. Hecht, *Nat. Nanotechnol.* **2007**, *2*, 687–691.
[5] J. Cai, P. Ruffieux, R. Jaafar, M. Bieri, T. Braun, S. Blankenburg, M. Muoth, A. P. Seitsonen, M. Saleh, X. Feng, et al., *Nature* **2010**, *466*, 470–473.
[6] A. Wiengarten, K. Seufert, W. Auwärter, D. Ecija, K. Diller, F. Allegretti, F. Bischoff, S. Fischer, D. A. Duncan, A. C. Papageorgiou, et al., *J. Am. Chem. Soc.* **2014**, *136*, 9346–9354.
[7] Q. Fan, J. M. Gottfried, J. Zhu, *Acc. Chem. Res.* **2015**, *48*, 2484–2494.
[8] L. Talirz, P. Ruffieux, R. Fasel, *Adv. Mater.* **2016**, *28*, 6222–6231.
[9] Q. Shen, H.-Y. Gao, H. Fuchs, *Nano Today* **2017**, *13*, 77–96.
[10] F. Klappenberger, Y.-Q. Zhang, J. Björk, S. Klyatskaya, M. Ruben, J. V. Barth, *Acc. Chem. Res.* **2015**, *48*, 2140–2150.
[11] B. Cirera, N. Gimenez-Agullo, J. Bjork, F. Martinez-Pena, A. Martin-Jimenez, J. Rodriguez-Fernandez, A. M. Pizarro, R. Otero, J. M. Gallego, P. Ballester, et al., *Nat. Commun.* **2016**, *7*, 11002.
[12] Q. Sun, R. Zhang, J. Qiu, R. Liu, W. Xu, *Adv. Mater.* **2018**, *30*, 1705630.
[13] T. Tseng, C. Urban, Y. Wang, R. Otero, S. L. Tait, M. Alcami, D. Ecija, M. Trelka, J. M. Gallego, N. Lin, et al., *Nat. Chem.* **2010**, *2*, 374–379.
[14] L. Gross, B. Schuler, N. Pavliček, S. Fatayer, Z. Majzik, N. Moll, D. Peña, G. Meyer, *Angew. Chem. Int. Ed.* **2018**, *57*, 3888–3908; *Angew. Chem.* **2018**, *130*, 3950–3972.
[15] J. Krüger, F. Eisenhut, T. Lehmann, J. M. Alonso, J. Meyer, D. Skidin, R. Ohmann, D. A. Ryndyk, D. Pérez, E. Guitián, et al., *J. Phys. Chem. C* **2017**, *121*, 20353–20358.
[16] S. Kawai, O. Krejčí, A. S. Foster, R. Pawlak, F. Xu, L. Peng, A. Orita, E. Meyer, *ACS Nano* **2018**, *12*, 8791–8797.
[17] J. Krüger, N. Pavliček, J. M. Alonso, D. Pérez, E. Guitián, T. Lehmann, G. Cuniberti, A. Gourdon, G. Meyer, L. Gross, et al., *ACS Nano* **2016**, *10*, 4538–4542.
[18] J. Krüger, F. Eisenhut, J. M. Alonso, T. Lehmann, E. Guitián, D. Pérez, D. Skidin, F. Gamaleja, D. A. Ryndyk, C. Joachim, et al., *Chem. Commun.* **2017**, *53*, 1583–1586.
[19] J. I. Urgel, H. Hayashi, M. Di Giovannantonio, C. A. Pignedoli, S. Mishra, O. Deniz, M. Yamashita, T. Dienel, P. Ruffieux, H. Yamada, et al., *J. Am. Chem. Soc.* **2017**, *139*, 11658–11661.
[20] R. Zuzak, R. Dorel, M. Kolmer, M. Szymonski, S. Godlewski, A. M. Echavarren, *Angew. Chem. Int. Ed.* **2018**, *57*, 10500–10505; *Angew. Chem.* **2018**, *130*, 10660–10665.
[21] R. Zuzak, R. Dorel, M. Krawiec, B. Such, M. Kolmer, M. Szymonski, A. M. Echavarren, S. Godlewski, *ACS Nano* **2017**, *11*, 9321–9329.
[22] J. Krüger, F. García, F. Eisenhut, D. Skidin, J. M. Alonso, E. Guitián, D. Pérez, G. Cuniberti, F. Moresco, D. Peña, *Angew. Chem. Int. Ed.* **2017**, *56*, 11945–11948; *Angew. Chem.* **2017**, *129*, 12107–12110.
[23] C. Moreno, M. Vilas-Varela, B. Kretz, A. Garcia-Lekue, M. V. Costache, M. Paradinas, M. Panighel, G. Ceballos, S. O. Valenzuela, D. Peña, et al., *Science* **2018**, *360*, 199.
[24] Q. Sun, B. V. Tran, L. Cai, H. Ma, X. Yu, C. Yuan, M. Stöhr, W. Xu, *Angew. Chem. Int. Ed.* **2017**, *56*, 12165–12169; *Angew. Chem.* **2017**, *129*, 12333–12337.
[25] Q. Sun, X. Yu, M. Bao, M. Liu, J. Pan, Z. Zha, L. Cai, H. Ma, C. Yuan, X. Qiu, et al., *Angew. Chem. Int. Ed.* **2018**, *57*, 4035–4038; *Angew. Chem.* **2018**, *130*, 4099–4102.
[26] J. Björk, F. Hanke, S. Stafström, *J. Am. Chem. Soc.* **2013**, *135*, 5768–5775.
[27] L. Dong, P. N. Liu, N. Lin, *Acc. Chem. Res.* **2015**, *48*, 2765–2774.
[28] J. Krüger, F. Eisenhut, D. Skidin, T. Lehmann, D. A. Ryndyk, G. Cuniberti, F. García, J. M. Alonso, E. Guitián, D. Pérez, et al., *ACS Nano* **2018**, *12*, 8506–8511.
[29] I. Piquero-Zulaica, A. Garcia-Lekue, L. Colazzo, C. K. Krug, M. S. G. Mohammed, Z. M. Abd El-Fattah, J. M. Gottfried, D. G. de Oteyza, J. E. Ortega, J. Lobo-Checa, *ACS Nano* **2018**, *12*, 10537–10544.
[30] N. Merino-Díez, A. Garcia-Lekue, E. Carbonell-Sanromà, J. Li, M. Corso, L. Colazzo, F. Sedona, D. Sánchez-Portal, J. I. Pascual, D. G. de Oteyza, *ACS Nano* **2017**, *11*, 11661–11668.

Manuscript received: December 12, 2018
Accepted manuscript online: February 14, 2019
Version of record online: March 12, 2019

Angewandte Chemie
Eine Zeitschrift der Gesellschaft Deutscher Chemiker

Supporting Information

On-Surface Synthesis of Ethynylene-Bridged Anthracene Polymers

Ana Sánchez-Grande, Bruno de la Torre, José Santos, Borja Cirera, Koen Lauwaet, Taras Chutora, Shayan Edalatmanesh, Pingo Mutombo, Johanna Rosen, Radek Zbořil, Rodolfo Miranda, Jonas Björk, Pavel Jelínek,* Nazario Martín,* and David Écija**

anie_201814154_sm_miscellaneous_information.pdf

Experimental and theoretical methods.

Experiments were performed in a two independent custom designed ultra-high vacuum systems that host a low-temperature Omicron and a Createc scanning tunneling microscope, respectively, where the base pressure was below 5×10^{-10} mbar. STM images were acquired with electrochemically etched tungsten tips, or cut and sharpened by focus ion beam (FIB) Pt/Ir tips, applying a bias (V_b) to the sample at a temperature of ~4 K. Precursing molecule (11,11,12,12-tetrabromoanthraquinodimethane) was synthesized following a procedure described elsewhere.[1] The Au(111) substrate was prepared by standard cycles of Ar^+ sputtering (800 eV) and subsequent annealing at 723 K for 10 minutes. Molecular precursor was deposited by organic molecular-beam epitaxy (OMBE) from a quartz crucible maintained at 373 K onto a clean Au(111) at room temperature. Whenever necessary samples were annealed to the desired temperature and subsequently transferred to the STM stage, which was maintained at 4 K. In AFM imaging, a metal tip mounted on a qplus sensor (resonant frequency ≈ 30 kHz; stiffness ≈ 1800 N/m) was oscillated with a constant amplitude of 50 pm. The tip apex was functionalized with a CO-molecule, and all images were captured in constant height mode.

The optimised 1D anthracene polymers on the Au(111) surface were calculated by the FHI-AIMS[2] and Fireball[3] program packages based on the *ab initio* density functional theory. The theoretical AFM images were calculated using an AFM probe particle simulator.[4] Theoretical dI/dV maps were calculated by PP-STM code[5] with s-like orbital tip.

Reaction pathways were calculated with the VASP code[6] within the framework of density functional theory, using the projector-augmented wave method[7] and a planewave basis set expanded to a kinetic energy cut-off of 400 eV. Exchange-correlation effects were described by the van der Waals density functional (vdW-DF)[8] with the version by Hamada denoted as rev-vdWDF2.[9] The Au(111) surface was represented by a four layered slab. Calculations on a single molecule were done using a $p(7\times7)$ surface unit cell together with a 3×3 *k*-point sampling, while a $p(8\times8)$ surface unit cell together with a 2×2 *k*-point sampling was used for dimerization reactions. Transition states were found using the climbing image nudged elastic band (CI-NEB)[10] and Dimer method,[11] and all local minima and saddle points were optimized until the residual forces on all atoms were smaller than 0.01 eV/Å, except for the bottom two layers of the slab which were kept fixed.

[1] S. Pola, C.-H. Kuo, W.-T. Peng, M. M. Islam, I. Chao, Y.-T. Tao, *Chem. Mater.* **2012**, *24*, 2566-2571.

[2] V. Blum, R. Gehrke, F. Hanke, P. Havu, V. Havu, X. Ren, K. Reuter, M. Scheffler, *Comput. Phys. Commun.* **2009**, *180*, 2175-2196.

[3] J. P. Lewis, P. Jelínek, J. Ortega, A. A. Demkov, D. G. Trabada, B. Haycock, H. Wang, G. Adams, J. K. Tomfohr, E. Abad, H. Wang, D. A. Drabold, *Phys. Status Solidi B* **2011**, *248*, 1989-2007.
[4] P. Hapala, G. Kichin, C. Wagner, F. S. Tautz, R. Temirov, P. Jelínek, *Phys. Rev. B* **2014**, *90*, 085421.
[5] O. Krejčí, P. Hapala, M. Ondráček, P. Jelínek, *Phys. Rev. B* **2017**, *95*, 045407.
[6] G. Kresse, J. Furthmüller, *J. Phys. Rev. B* **1996**, *54*, 11169-11186.
[7] P. E. Blöchl, *Phys. Rev. B* **1994**, *59*, 17953-17979.
[8] M. Dion, H. Rydberg, E. Schröder, D. C. Langreth, B. I. Lundqvist, *Phys. Rev. Lett.* **2004**, *92*, 246401.
[9] I. Hamada, *Phys. Rev. B* **2014**, *89*, 121103(R)-121107(R).
[10] G. Henkelman, B. P. Uberuaga, H. Jónsson, *J. Chem. Phys.* **2000**, *113*, 9901-9904.
[11] J. Kästner, P. Sherwood, *J. Chem. Phys.* **2008**, *128*.

Integrity of molecular species and close-packed self-assembly.

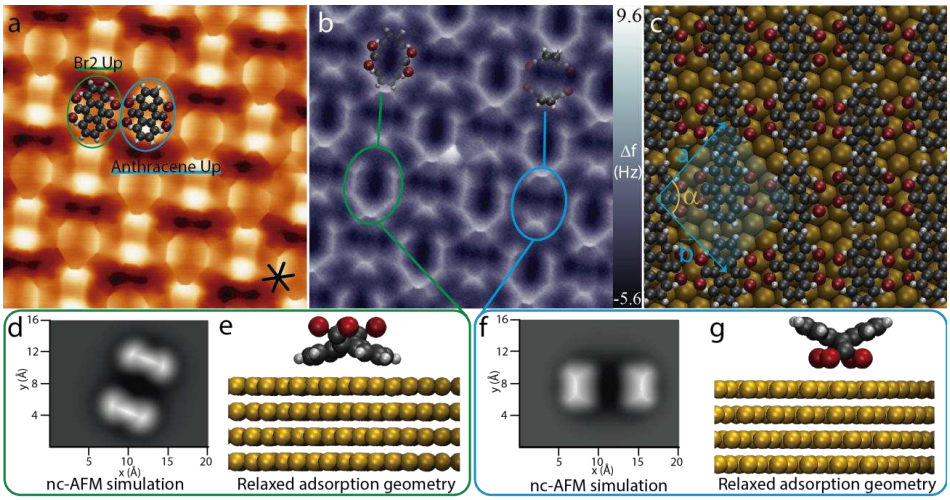

Figure SI1. a) STM image of the supramolecular self-assembly showing two different adsorption geometries, with the Br_2 groups or the lateral aryl moieties pointing away from the surface, highlighted in green and blue, respectively (5×5 nm^2, 20pA, -60mV). b) nc-AFM image showing the different appearance of the species (5×5 nm^2, 10 mV). c) Ball-and-stick model with the unit cell (blue) and the unit cell vector |a|=|b|= 13.7 ± 0.5 Å, enclosing angle α = 95 ± 1°. d) nc-AFM simulation of the configuration where the Br_2 groups are pointing away from the substrate (highlighted in green in b), calculated for the relaxed adsorption geometry presented in e (E^1_{ads}= -2.47 eV). f-g) nc-AFM simulation of the configuration where the Br_2 groups are pointing towards the substrate (highlighted in blue in b) (E^2_{ads} = -2.49 eV).

Formation and self-assembly of high quality ethynylene bridged anthracene polymers on Au(111).

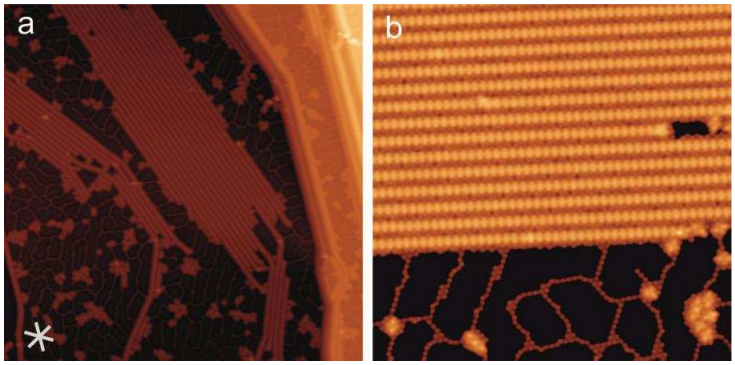

Figure SI2. a,b) STM images of ethynylene bridged polymers, coexisting with isolated oligomers and bromine atoms. The white cross depicts the close-packed high symmetry directions of the surface. Scanning tunneling parameters: a,b) V_{bias} = 100 mV, I = 10 pA. Size: a) 100 x 100 nm^2 and b) 30 x 30 nm^2

Visualization of ethynylene bridge at different tip-sample distances

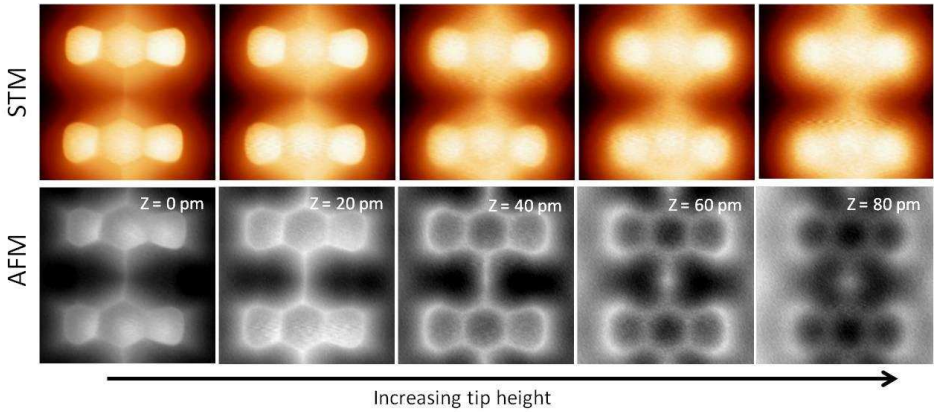

Figure SI3. STM and AFM high-resolution images of single-triple-single bridge at different tip heights with a CO-tip. Scanning parameters: V_{bias} = 3 mV. Size: 1.3 x 1.3 nm^2

Identification of chemical termination of ethylene linked anthracene oligomers and chains.

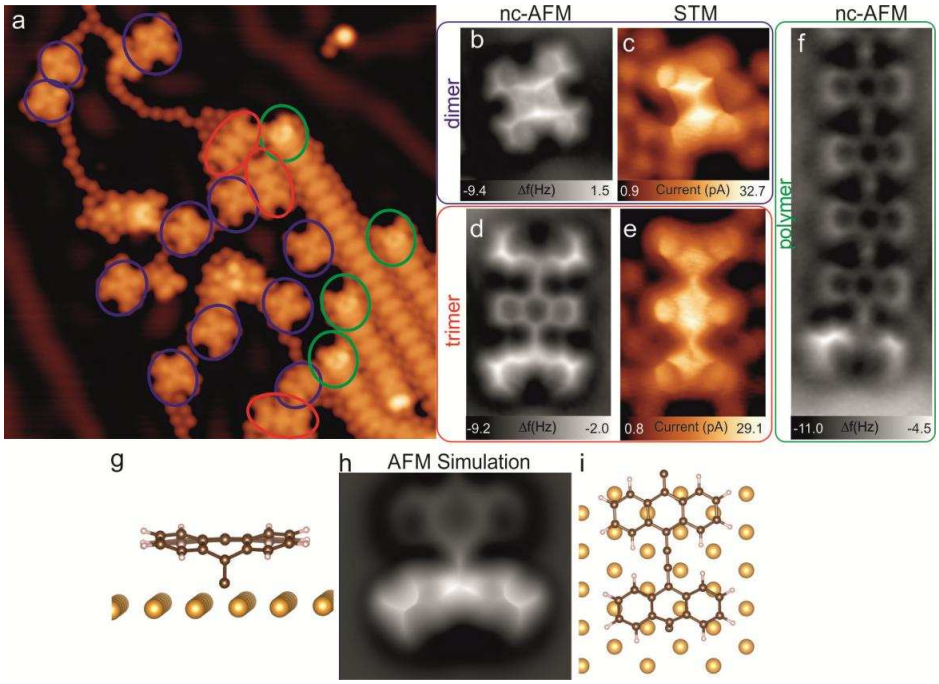

Figure SI4. a) Large scale STM image showing the coexistance of dimers, trimers and polymeric chains, after depositing 4Br-anthracene on Au(111) and annealing at 400 K (Vbias = -100 mV, I = 50 pA, size = 17.9 x 17.9 nm^2). b) nc-AFM image and c) constant height STM topograph of a dimer (size = 2 x 2 nm^2). d) nc-AFM image and e) constant height STM topograph of a trimer (size = 1.7 x 2.4 nm^2). f) nc-AFM of the ending of a chain (size = 1.6 x 4.3 nm^2). g) Side view DFT simulation, h) nc-AFM simulation, and i) Top view DFT simulation of the end of a chain, allowing to relax the edge monomer.

On-surface design of high quality ethynylene linked anthracene polymers on Au(111).

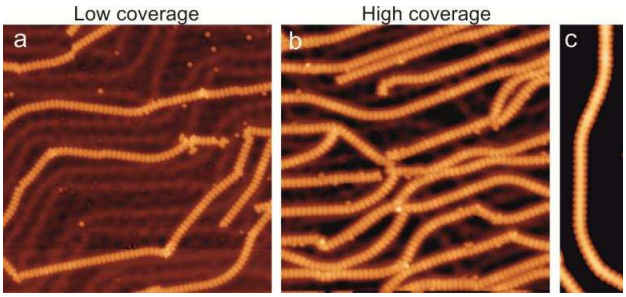

Figure SI5. Large scale STM image of a) low coverage and b) high coverage curved polymer. c) Long and flexible defect-free polymer. Scanning tunneling parameters: a) V_{bias} = 2mV, I = 10 pA, b) Vbias = 50 mV, I = 10 pA, and c) V_{bias} = 1.8 V, I = 850 pA. Image size: a) 40 x 40 nm^2, b) 35 x 35 nm^2, and c) 29.2 x 6.7 nm^2.

Flexibility of ethynylene linked anthracene polymers.

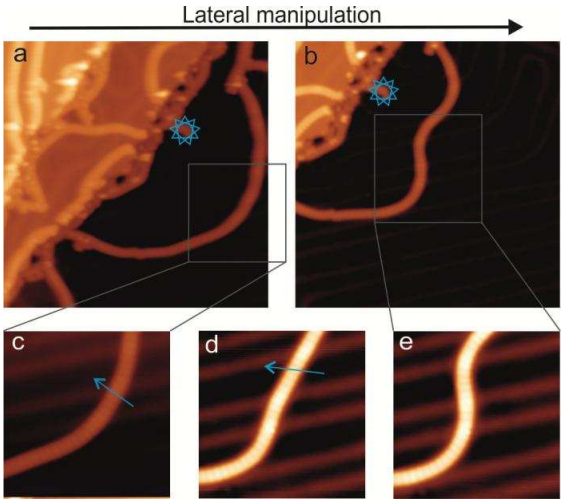

Figure SI6. STM topographs of a) the initial (size = 40.3 x 40.3 nm^2) and b) the final shape (size = 40 x 40 nm^2) of an ethynylene bridged anthracene polymer after tip induced lateral manipulation. The blue star indicates a point of reference. High resolution STM images of c) stage 1, d) stage 2, and e) final stage of the portion shape of the curved polymer after performing a two stepwise tip induced lateral manipulation. c-e) Size = 15.7 x 15.7 nm^2. Direction and sense of each manipulation is indicated by blue curves. Scanning tunneling parameters for a-e: V_{bias} = -1V, 150 pA. Lateral manipulation parameters for all processes: V_{bias} = -100 mV, I = 20 nA, t = 30 ms.

Passivation with hydrogen the terminal edges of ethynylene bridged anthracene chains.

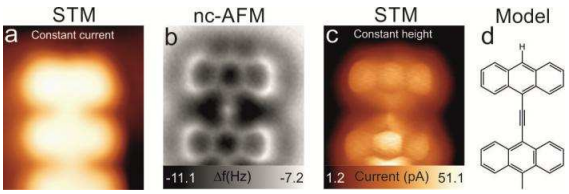

Figure SI7. a) High resolution constant current STM topograph (V_{bias}= 100 mV, I = 300 pA, size = 1.8 x 2.1 nm^2), b) nc-AFM image (size = 1.5 x 1.5 nm^2), c) constant height STM topograph (size = 1.5 x 1.5 nm^2), and d) chemical structure of the edge of a ethylene bridged anthracene polymer, after depositing **4BrAn** on Au(111) and annealing to 500 K, which enables desorption of bromine atoms and passivation of polymer termini by hydrogen.

Calculated AFM image of H-terminated end of anthracene polymer on Au(111)

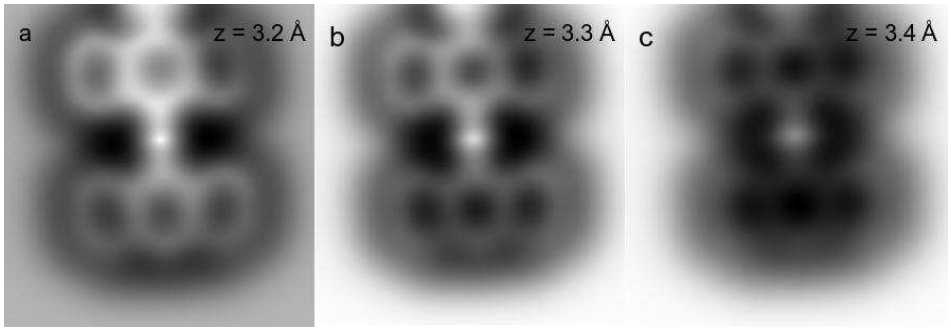

Figure SI8. Simulated AFM image of H-terminated anthracene chain on Au(111) substrate using the probe particle model at three different heights: a) 3.2, b) 3.3 and c) 3.4 Å.

Comparison of calculated projected density of states of freestanding anthracene polymer and on Au(111) surface

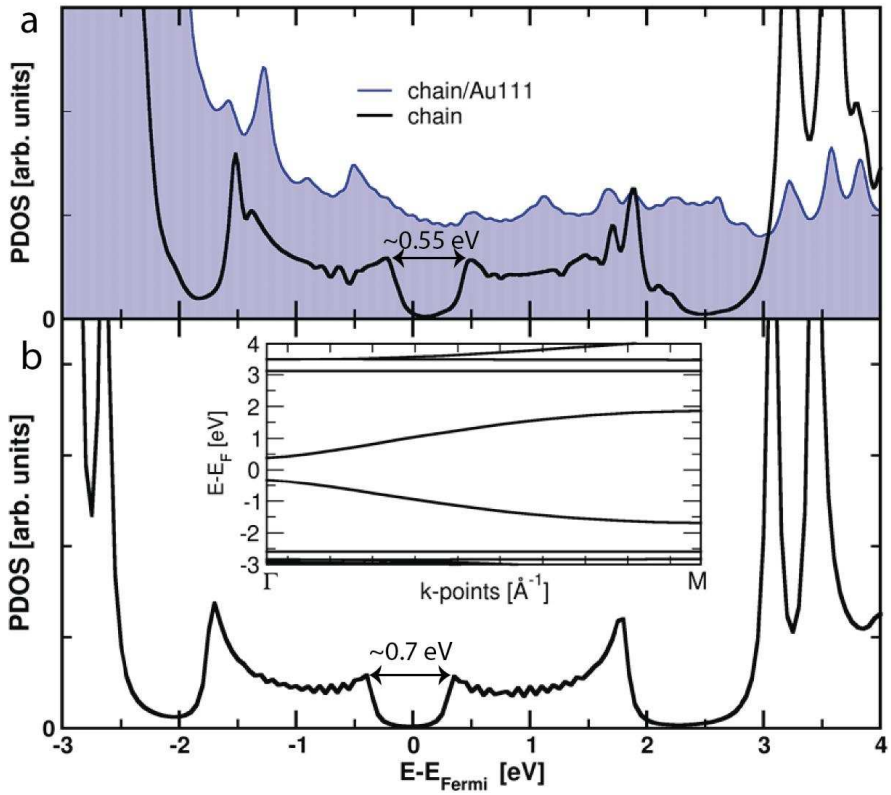

Figure SI9. a) Calculated PDOS of anthracene polymer on Au(111) substrate using DFT GGA-BLYP functional, blue line represents total density of states including both the polymer and the Au(111) surface, black line shows projected density of states of the polymer only, the Fermi level is set to zero. b) Calculated PDOS of a freestanding anthracene polymer using DFT GGA-BLYP functional. Inset of Figure B shows corresponding calculated band structure of the freestanding polymer, which has very similar dispersive character of the valence/conduction bands as more computationally expensive hybrid B3LYP (see Figure 2a in the main text). Nevertheless, GGA BLYP functional gives much lower band gap ~0.7 eV comparing to 1.4 eV for the hybrid B3LYP functional. Unfortunately, full calculation of the anthracene polymer including the Au(111) substrate with the hybrid B3LYP functional is computationally not feasible with current computer resource. Therefore, we analyzed the effect of the metallic surface using the GGA BLYP functional, which provides reasonable description of the band structure saving the band gap problem. The calculation shows that the dispersive character of VB and CB does not change, only the band gap of the polymer on Au(111) surface is reduced to ~0.55 eV, due to additional screening from surface electrons. This reveals only weak electronic coupling of the polymer with the metallic substrate.

Alternative coupling pathway.

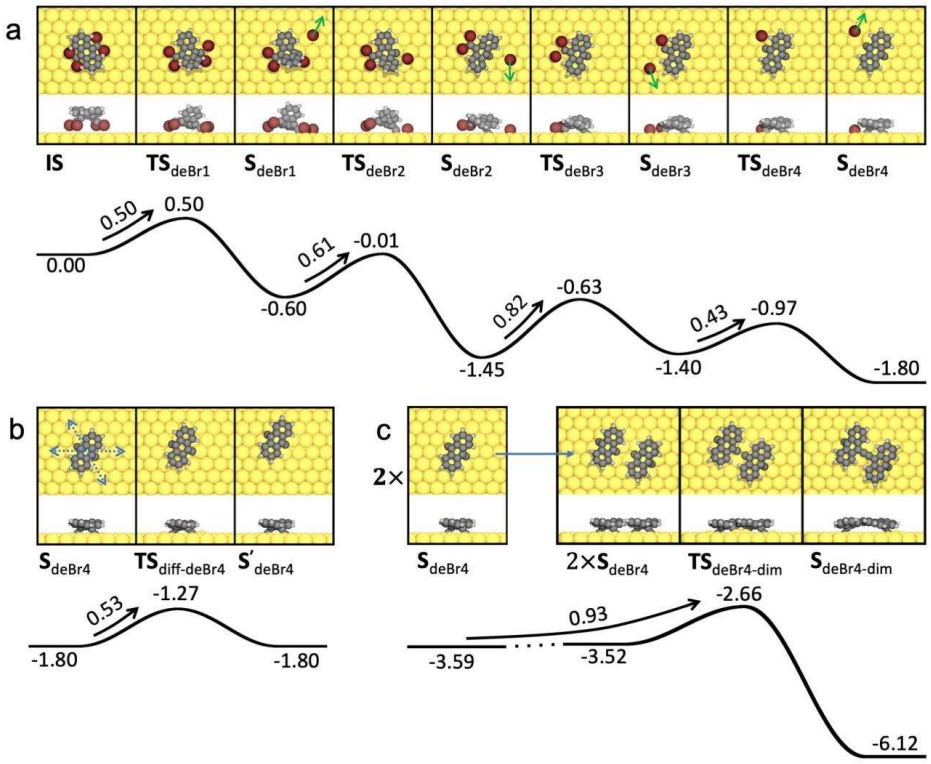

Figure SI10. Alternative pathway for the coupling, following two initial dehalogenation steps of **4BrAn** on Au(111), i.e. from the $\mathbf{S}_{deBr2}$ state, depicting top and side views of local minima ($\mathbf{S}_x$) and transition states ($\mathbf{TS}_x$) with corresponding energy profile with respect to the initial state (**IS**): (a) diffusion of $\mathbf{S}_{deBr2}$ molecule, and (b) coupling of two $\mathbf{S}_{deBr2}$ molecules. Units in eV.

One may imagine the coupling of two molecules with one of the CBr_2 groups dehalogenated ($\mathbf{S}_{deBr2}$ in Figure 3a), in particular considering the high activation energy of the third dehalogenation step. The diffusion barrier of $\mathbf{S}_{deBr2}$ is close to that of $\mathbf{S}_{deBr4}$, but the activation energy of coupling is significantly higher (cf. Figure SI10) and the alternative pathway can be discarded. Our theoretical insight matches well with experimental results, where no oligomer or polymer with intact terminal $=CBr_2$ groups were detected.

Conclusion

This thesis is focused on the study of molecular structures on metal surfaces. We used SPM techniques to study various carbon-based molecular nanostructures on Au(111) surface in UHV environment. Additionally, we tested a promising candidate for tip functionalization. The main results of this doctoral thesis can be summarized by the three following topics:

(I) Formation and characterization of fullerene-based nanostructures at RT.

We presented a combined theoretical and experimental study of modified fullerene-based structures on Au(111) surface. STM images revealed that fullerene molecules form islands or chains at terrace edges of monoatomic gold steps at RT due to a low surface diffusion barrier. After 120 eV Ar^+ ion irradiation, bright features appear at the Au(111) herringbone corners with lower apparent height of about 1.5 Å with respect to fullerenes islands as revealed by topographic line profiles. We attribute these bright features to be defective fullerene molecules with single vacancies artificially generated by the soft sputtering process. DFT calculations lead C_{59} fullerenes with single defects are fully consistent with the experimental results. The single vacancy created by the removal of a carbon atom from the fullerene increases the molecular reactivity. As a result, the C_{59} molecules adsorbed with the defect close to the surface, having a binding energy 1.6 eV higher than that of pristine fullerene.

(II) N_2O as new molecular candidate for AFM tip functionalization.

We have investigated functionalization of the AFM tip apex by vertical manipulation of N_2O molecules adsorbed on a Au(111) surface at temperatures below 10 K. N_2O molecules adsorb parallel to the surface, arranging in triangular clusters. We functionalized a metallic tip apex with a single N_2O molecule by picking it up from the Au(111) substrate. The functionalization of the tip with N_2O can be achieved with co-adsorbed FePc molecules. The performance of the N_2O tips was evaluated via sub-molecular imaging and site-specific force ($\triangle f(z)$) spectroscopies on FePc molecules. The high-resolution images of FePc obtained with a N_2O decorated tip are qualitatively equivalent to those acquired with a CO-tip. However, images obtained with a N_2O tip show noticeable asymmetry and the force spectroscopy reveals higher interaction energies. These findings, in addition to DFT calculations, indicate a bent adsorption geometry and strong charge redistribution of the N_2O on the tip apex in comparison to a CO-tip.

(III) On-surface synthesis and characterization of anthracene-based polymers.

We have presented a strategy for on-surface synthesis of ethynylene-bridged anthracene π-conjugated polymers. The deposition of precursor molecules 4BrAn

on Au(111) surface and subsequent annealing triggered an on-surface chemical reaction with a unique pathway. An initial annealing step to 400 K enables dehalogenation and subsequent homocoupling. As a result, high-quality 1D anthracene-based polymeric wires were formed. A second annealing step to 500 K leads to desorption of bromine atoms which allows the formation of long and flexible polymers preserving the chemical structure of their constituent molecules. We used a combination of LT-STM/AFM experiments supported by DFT calculations to fully characterize their electronic and conformational properties. These polymers have a low experimental band gap of 1.5 eV.

In closing, these results offer a comprehensive study of various molecular structures on the Au(111) surface using SPM techniques in UHV. The methods used in this work provides a pathway for the formation of stable metal–molecule anchors for fullerene-based nanostructures and on-surface polymerization of low bandgap π-conjugated molecular wires. These studies have advanced our understanding of molecular structures on surfaces and provide further insight regarding the origin of sub-molecular resolution in AFM images.

Bibliography

[1] Gordon E Moore. Cramming more components onto integrated circuits. *Proceedings of the IEEE*, 86(1):82–85, 1998.

[2] Jung Han Choi and Krzysztof Iniewski. *High-speed and Lower Power Technologies: Electronics and Photonics*. CRC Press, 2018.

[3] Paven Thomas Mathew and Fengzhou Fang. Advances in molecular electronics: A brief review. *Engineering*, 2018.

[4] Dong Xiang, Xiaolong Wang, Chuancheng Jia, Takhee Lee, and Xuefeng Guo. Molecular-scale electronics: from concept to function. *Chemical Reviews*, 116(7):4318–4440, 2016.

[5] Arieh Aviram and Mark A Ratner. Molecular rectifiers. *Chemical Physics Letters*, 29(2):277–283, 1974.

[6] Gerd Binnig, Heinrich Rohrer, Christoph Gerber, and Edmund Weibel. Tunneling through a controllable vacuum gap. *Applied Physics Letters*, 40(2):178–180, 1982.

[7] Gerd Binnig, Heinrich Rohrer, Christoph Gerber, and Edmund Weibel. Surface studies by scanning tunneling microscopy. *Physical Review Letters*, 49(1):57, 1982.

[8] Amandine Bellec, Jérôme Lagoute, and Vincent Repain. Molecular electronics: Scanning tunneling microscopy and single-molecule devices. *Comptes Rendus Chimie*, 21(12):1287–1299, 2018.

[9] Christian Joachim, James K Gimzewski, Reto R Schlittler, and Corinne Chavy. Electronic transparence of a single C_{60} molecule. *Physical Review Letters*, 74(11):2102, 1995.

[10] Florian Pump, Ruslan Temirov, Olga Neucheva, Serguei Soubatch, Stefan Tautz, Michael Rohlfing, and Gianaurelio Cuniberti. Quantum transport through stm-lifted single ptcda molecules. *Applied Physics A*, 93(2):335–343, 2008.

[11] Barry C Stipe, Mohammad A Rezaei, and Wilson Ho. Single-molecule vibrational spectroscopy and microscopy. *Science*, 280(5370):1732–1735, 1998.

[12] Bruno de la Torre, Martin Švec, Giuseppe Foti, Ondřej Krejčí, Prokop Hapala, Aran Garcia-Lekue, Thomas Frederiksen, Radek Zbořil, Andres

Arnau, Héctor Vázquez, et al. Submolecular resolution by variation of the inelastic electron tunneling spectroscopy amplitude and its relation to the AFM/STM signal. *Physical Review Letters*, 119(16):166001, 2017.

[13] Xiaohui Qiu, George V Nazin, and Wilson Ho. Vibronic states in single molecule electron transport. *Physical Review Letters*, 92(20):206102, 2004.

[14] Andreas J Heinrich, Jay A Gupta, Christopher P Lutz, and Donald M Eigler. Single-atom spin-flip spectroscopy. *Science*, 306(5695):466–469, 2004.

[15] Roland Wiesendanger. Spin mapping at the nanoscale and atomic scale. *Reviews of Modern Physics*, 81(4):1495, 2009.

[16] Noriyuki Tsukahara, Ken-ichi Noto, Michiaki Ohara, Susumu Shiraki, Noriaki Takagi, Yasutaka Takata, Jun Miyawaki, Munetaka Taguchi, Ashish Chainani, Shik Shin, et al. Adsorption-induced switching of magnetic anisotropy in a single iron (ii) phthalocyanine molecule on an oxidized Cu(110) surface. *Physical Review Letters*, 102(16):167203, 2009.

[17] Jascha Repp, Gerhard Meyer, Sladjana M Stojković, André Gourdon, and Christian Joachim. Molecules on insulating films: scanning-tunneling microscopy imaging of individual molecular orbitals. *Physical Review Letters*, 94(2):026803, 2005.

[18] Leo Gross, Nikolaj Moll, Fabian Mohn, Alessandro Curioni, Gerhard Meyer, Felix Hanke, and Mats Persson. High-resolution molecular orbital imaging using a p-wave STM tip. *Physical Review Letters*, 107(8):086101, 2011.

[19] Donald M Eigler and Erhard K Schweizer. Positioning single atoms with a scanning tunnelling microscope. *Nature*, 344(6266):524, 1990.

[20] Barry C Stipe, Mohammad A Rezaei, Wilson Ho, Shiwu Gao, Mats Persson, and Bengt I Lundqvist. Single-molecule dissociation by tunneling electrons. *Physical Review Letters*, 78(23):4410, 1997.

[21] Saw-Wai Hla, Ludwig Bartels, Gerhard Meyer, and Karl-Heinz Rieder. Inducing all steps of a chemical reaction with the scanning tunneling microscope tip: towards single molecule engineering. *Physical Review Letters*, 85(13):2777, 2000.

[22] Yuji Okawa and Masakazu Aono. Linear chain polymerization initiated by a scanning tunneling microscope tip at designated positions. *The Journal of Chemical Physics*, 115(5):2317–2322, 2001.

[23] Gerd Binnig, Calvin F Quate, and Christoph Gerber. Atomic force microscope. *Physical Review Fetters*, 56(9):930, 1986.

[24] Markus Ternes, Christopher P Lutz, Cyrus F Hirjibehedin, Franz J Giessibl, and Andreas J Heinrich. The force needed to move an atom on a surface. *Science*, 319(5866):1066–1069, 2008.

[25] Christian Loppacher, Martin Guggisberg, Oliver Pfeiffer, Ernst Meyer, Martin Bammerlin, Roland Lüthi, Reto Schlittler, James K Gimzewski, Hao Tang, and Christian Joachim. Direct determination of the energy required to operate a single molecule switch. *Physical Review Letters*, 90(6):066107, 2003.

[26] Franz J Giessibl. High-speed force sensor for force microscopy and profilometry utilizing a quartz tuning fork. *Applied Physics Letters*, 73(26):3956–3958, 1998.

[27] Franz J Giessibl. The qplus sensor, a powerful core for the atomic force microscope. *Review of Scientific Instruments*, 90(1):011101, 2019.

[28] Fabian Mohn, Bruno Schuler, Leo Gross, and Gerhard Meyer. Different tips for high-resolution atomic force microscopy and scanning tunneling microscopy of single molecules. *Applied Physics Letters*, 102(7):073109, 2013.

[29] Leo Gross, Fabian Mohn, Nikolaj Moll, Peter Liljeroth, and Gerhard Meyer. The chemical structure of a molecule resolved by atomic force microscopy. *Science*, 325(5944):1110–1114, 2009.

[30] Leo Gross, Bruno Schuler, Niko Pavliček, Shadi Fatayer, Zsolt Majzik, Nikolaj Moll, Diego Peña, and Gerhard Meyer. Atomic force microscopy for molecular structure elucidation. *Angewandte Chemie International Edition*, 57(15):3888–3908, 2018.

[31] Bruno Schuler, Wei Liu, Alexandre Tkatchenko, Nikolaj Moll, Gerhard Meyer, Anish Mistry, David Fox, and Leo Gross. Adsorption geometry determination of single molecules by atomic force microscopy. *Physical Review Letters*, 111(10):106103, 2013.

[32] Leo Gross, Fabian Mohn, Nikolaj Moll, Bruno Schuler, Alejandro Criado, Enrique Guitián, Diego Peña, André Gourdon, and Gerhard Meyer. Bond-order discrimination by atomic force microscopy. *Science*, 337(6100):1326–1329, 2012.

[33] Fabian Mohn, Leo Gross, Nikolaj Moll, and Gerhard Meyer. Imaging the charge distribution within a single molecule. *Nature Nanotechnology*, 7(4):227, 2012.

[34] Prokop Hapala, Martin Švec, Oleksandr Stetsovych, Nadine J Van Der Heijden, Martin Ondráček, Joost Van Der Lit, Pingo Mutombo, Ingmar Swart, and Pavel Jelínek. Mapping the electrostatic force field of single molecules from high-resolution scanning probe images. *Nature Communications*, 7:11560, 2016.

[35] Bruno de la Torre, Martin Švec, Prokop Hapala, Jesus Redondo, Ondřej Krejčí, Rabindranath Lo, Debashree Manna, Amrit Sarmah, Dana Nachtigallová, Jiří Tuček, et al. Non-covalent control of spin-state in metal-organic complex by positioning on N-doped graphene. *Nature Communications*, 9(1):2831, 2018.

[36] Ruslan Temirov, Serguei Soubatch, Olga Neucheva, Adam C Lassise, and Frank S Tautz. A novel method achieving ultra-high geometrical resolution in scanning tunnelling microscopy. *New Journal of Physics*, 10(5):053012, 2008.

[37] Dimas G de Oteyza, Patrick Gorman, Yen-Chia Chen, Sebastian Wickenburg, Alexander Riss, Duncan J Mowbray, Grisha Etkin, Zahra Pedramrazi, Hsin-Zon Tsai, Angel Rubio, et al. Direct imaging of covalent bond structure in single-molecule chemical reactions. *Science*, 340(6139):1434–1437, 2013.

[38] Leonhard Grill, Matthew Dyer, Leif Lafferentz, Mats Persson, Maike V Peters, and Stefan Hecht. Nano-architectures by covalent assembly of molecular building blocks. *Nature Nanotechnology*, 2(11):687, 2007.

[39] Christina Tönshoff and Holger F Bettinger. Photogeneration of octacene and nonacene. *Angewandte Chemie International Edition*, 49(24):4125–4128, 2010.

[40] José I Urgel, Shantanu Mishra, Hironobu Hayashi, Jan Wilhelm, Carlo A Pignedoli, Marco Di Giovannantonio, Roland Widmer, Masataka Yamashita, Nao Hieda, Pascal Ruffieux, et al. On-surface light-induced generation of higher acenes and elucidation of their open-shell character. *Nature Communications*, 10(1):861, 2019.

[41] Emiko Kazuma, Jaehoon Jung, Hiromu Ueba, Michael Trenary, and Yousoo Kim. Real-space and real-time observation of a plasmon-induced chemical reaction of a single molecule. *Science*, 360(6388):521–526, 2018.

[42] Niko Pavliček, Anish Mistry, Zsolt Majzik, Nikolaj Moll, Gerhard Meyer, David J Fox, and Leo Gross. Synthesis and characterization of triangulene. *Nature Nanotechnology*, 12(4):308, 2017.

[43] Niko Pavliček, Bruno Schuler, Sara Collazos, Nikolaj Moll, Dolores Pérez, Enrique Guitián, Gerhard Meyer, Diego Peña, and Leo Gross. On-surface generation and imaging of arynes by atomic force microscopy. *Nature Chemistry*, 7(8):623, 2015.

[44] Josh A Lipton-Duffin, Oleksandr Ivasenko, Dmitrii F Perepichka, and Federico Rosei. Synthesis of polyphenylene molecular wires by surface-confined polymerization. *Small*, 5(5):592–597, 2009.

[45] Lei Dong, Zi'Ang Gao, and Nian Lin. Self-assembly of metal–organic coordination structures on surfaces. *Progress in Surface Science*, 91(3):101–135, 2016.

[46] Jinming Cai, Pascal Ruffieux, Rached Jaafar, Marco Bieri, Thomas Braun, Stephan Blankenburg, Matthias Muoth, Ari P Seitsonen, Moussa Saleh, Xinliang Feng, et al. Atomically precise bottom-up fabrication of graphene nanoribbons. *Nature*, 466(7305):470, 2010.

[47] Richard P Feynman. There's plenty of room at the bottom: An invitation to enter a new field of physics. 1959.

[48] Gerd Binnig, Heinrich Rohrer, Christoph Gerber, and Eduard Weibel. 7×7 reconstruction on Si(111) resolved in real space. *Physical Review Letters*, 50(2):120, 1983.

[49] Gerd Binnig and Heinrich Rohrer. Scanning tunneling microscopy—from birth to adolescence. *Reviews of Modern Physics*, 59(3):615, 1987.

[50] Randall M Feenstra. Scanning tunneling spectroscopy. *Surface Science*, 299:965–979, 1994.

[51] Sebastian Loth, Markus Etzkorn, Christopher P Lutz, Donald M Eigler, and Andreas J Heinrich. Measurement of fast electron spin relaxation times with atomic resolution. *Science*, 329(5999):1628–1630, 2010.

[52] Peter Zeppenfeld, Christopher P Lutz, and Donald M Eigler. Manipulating atoms and molecules with a scanning tunneling microscope. *Ultramicroscopy*, 42:128–133, 1992.

[53] Phaedon Avouris. Manipulation of matter at the atomic and molecular levels. *Accounts of Chemical Research*, 28(3):95–102, 1995.

[54] Ludwig Bartels, Gerhard Meyer, and Karl-Heinz Rieder. Basic steps of lateral manipulation of single atoms and diatomic clusters with a scanning tunneling microscope tip. *Physical Review Letters*, 79(4):697, 1997.

[55] Michael F Crommie, Christopher P Lutz, and Donald M Eigler. Confinement of electrons to quantum corrals on a metal surface. *Science*, 262(5131):218–220, 1993.

[56] Bert Voigtländer. *Scanning Probe Microscopy.* Springer, 2016.

[57] C Julian Chen. *Introduction to scanning tunneling microscopy*, volume 4. Oxford University Press on Demand, 1993.

[58] John Bardeen. Tunnelling from a many-particle point of view. *Physical Review Letters*, 6(2):57, 1961.

[59] Jerry Tersoff and Donald R Hamann. Theory and application for the scanning tunneling microscope. *Physical Review Letters*, 50(25):1998, 1983.

[60] Yossi Martin, Clayton C Williams, and Kumar H Wickramasinghe. Atomic force microscope–force mapping and profiling on a sub 100-Å scale. *Journal of Applied Physics*, 61(10):4723–4729, 1987.

[61] Thomas R Albrecht, Peter Grütter, David Horne, and Daniel Rugar. Frequency modulation detection using high-Q cantilevers for enhanced force microscope sensitivity. *Journal of Applied Physics*, 69(2):668–673, 1991.

[62] Stefan Torbrügge, Oliver Schaff, and Jörg Rychen. Application of the kolibri sensor to combined atomic-resolution scanning tunneling microscopy and noncontact atomic-force microscopy imaging. *Journal of Vacuum Science & Technology B, Nanotechnology and Microelectronics: Materials, Processing, Measurement, and Phenomena*, 28(3):C4E12–C4E20, 2010.

[63] Franz J Giessibl. Advances in atomic force microscopy. *Reviews of Modern Physics*, 75(3):949, 2003.

[64] Hendrik Hölscher and Udo D Schwarz. Theory of amplitude modulation atomic force microscopy with and without Q-control. *International Journal of Non-Linear Mechanics*, 42(4):608–625, 2007.

[65] John E Sader, Takayuki Uchihashi, Michael J Higgins, Alan Farrell, Yoshikazu Nakayama, and Suzanne P Jarvis. Quantitative force measurements using frequency modulation atomic force microscopy—theoretical foundations. *Nanotechnology*, 16(3):S94, 2005.

[66] Franz J Giessibl. A direct method to calculate tip-sample forces from frequency shifts in frequency-modulation atomic force microscopy. *Applied Physics Letters*, 78(1):123–125, 2001.

[67] John E Sader and Suzanne P Jarvis. Accurate formulas for interaction force and energy in frequency modulation force spectroscopy. *Applied Physics Letters*, 84(10):1801–1803, 2004.

[68] A Mark Lantz, Hans-Josef Hug, Regina Hoffmann, JA Pieter Van Schendel, Peter Kappenberger, Sophie Martin, Alexis Baratoff, and Hans Joachim Güntherodt. Quantitative measurement of short-range chemical bonding forces. *Science*, 291(5513):2580–2583, 2001.

[69] Manuel Nonnenmacher, Michael P o'Boyle, and Kumar H Wickramasinghe. Kelvin probe force microscopy. *Applied Physics Letters*, 58(25):2921–2923, 1991.

[70] John Edward Jones. On the determination of molecular fields.—II. from the equation of state of a gas. *Proceedings of the Royal Society of London. Series A, Containing Papers of a Mathematical and Physical Character*, 106(738):463–477, 1924.

[71] Hans Lüth and H Lèuth. *Solid surfaces, interfaces and thin films*, volume 4. Springer, 2001.

[72] Scientaomicron. https://www.scientaomicron.com.

[73] Createc. https://createc.de/.

[74] Gerhard Meyer. A simple low-temperature ultrahigh-vacuum scanning tunneling microscope capable of atomic manipulation. *Review of Scientific Instruments*, 67(8):2960–2965, 1996.

[75] Felix Hanke and Jonas Björk. Structure and local reactivity of the Au(111) surface reconstruction. *Physical Review B*, 87(23):235422, 2013.

[76] Flemming Besenbacher, Jeppe V Lauritsen, Trolle R Linderoth, Erik Lægsgaard, Ronnie T Vang, and Stefan Wendt. Atomic-scale surface science phenomena studied by scanning tunneling microscopy. *Surface Science*, 603(10-12):1315–1327, 2009.

[77] Harald Ibach. *Physics of surfaces and interfaces*, volume 12. Springer, 2006.

[78] Falko P Netzer and Alessandro Fortunelli. *Oxide materials at the two-dimensional limit*, volume 234. Springer, 2016.

[79] James K Schoelz, Peng Xu, Steven D Barber, Dejun Qi, Matthew L Ackerman, Gobind Basnet, Cameron T Cook, and Paul M Thibado. High-percentage success method for preparing and pre-evaluating tungsten tips for atomic-resolution scanning tunneling microscopy. *Journal of Vacuum*

Science & Technology B, Nanotechnology and Microelectronics: Materials, Processing, Measurement, and Phenomena, 30(3):033201, 2012.

[80] Jhon P Ibe, Paul P Bey Jr, Susan L Brandow, Robert A Brizzolara, Nancy A Burnham, Daniel P DiLella, Kok P Lee, Christie RK Marrian, and Richard J Colton. On the electrochemical etching of tips for scanning tunneling microscopy. *Journal of Vacuum Science & Technology A: Vacuum, Surfaces, and Films*, 8(4):3570–3575, 1990.

[81] Centre for Analysis of Functional Materials (SAFMAT). http://xroads.fzu.cz/laboratories/centre-analysis-functional-materials.

[82] Ole Albrektsen, HWM Salemink, Anders K Mo/rch, and AndersR Thölen. Reliable tip preparation for high-resolution scanning tunneling microscopy. *Journal of Vacuum Science & Technology B: Microelectronics and Nanometer Structures Processing, Measurement, and Phenomena*, 12(6):3187–3190, 1994.

[83] David K Biegelsen, Fernando A Ponce, Joseph C Tramontana, and Selina M Koch. Ion milled tips for scanning tunneling microscopy. *Applied Physics Letters*, 50(11):696–698, 1987.

[84] Antonio Cricenti, Ernesto Paparazzo, Manuela Scarselli, Luciano Moretto, and Stefano Selci. Preparation and characterization of tungsten tips for scanning tunneling microscopy. *Review of Scientific Instruments*, 65(5):1558–1560, 1994.

[85] Johannes V Barth, Giovanni Costantini, and Klaus Kern. Engineering atomic and molecular nanostructures at surfaces. In *Nanoscience And Technology: A Collection of Reviews from Nature Journals*, pages 67–75. World Scientific, 2010.

[86] Timothy A Su, Madhav Neupane, Michael L Steigerwald, Latha Venkataraman, and Colin Nuckolls. Chemical principles of single-molecule electronics. *Nature Reviews Materials*, 1(3):16002, 2016.

[87] Christian Joachim, Jim K Gimzewski, and Aviram Arieh. Electronics using hybrid-molecular and mono-molecular devices. *Nature*, 408(6812):541, 2000.

[88] James K Gimzewski and Christian Joachim. Nanoscale science of single molecules using local probes. *Science*, 283(5408):1683–1688, 1999.

[89] Michael Salinas and Marcus Halik. Photoactive self-assembled monolayers for optically switchable organic thin-film transistors. *Applied Physics Letters*, 102(20):92_1, 2013.

[90] Susan M Barlow and Rasmita Raval. Complex organic molecules at metal surfaces: bonding, organisation and chirality. *Surface Science Reports*, 50(6-8):201–341, 2003.

[91] Xing-Qiang Shi, Michel A Van Hove, and Rui-Qin Zhang. Survey of structural and electronic properties of C_{60} on close-packed metal surfaces. *Journal of Materials Science*, 47(21):7341–7355, 2012.

[92] Michael Paßens, Rainer Waser, and Silvia Karthäuser. Enhanced fullerene-Au(111) coupling in $(22 \times \sqrt{3})$ R30 superstructures with intermolecular interactions. *Beilstein Journal of Nanotechnology*, 6(1):1421–1431, 2015.

[93] Xin Zhang, Feng Yin, Richard E Palmer, and Quanmin Guo. The C_{60}/Au(111) interface at room temperature: A scanning tunnelling microscopy study. *Surface Science*, 602(4):885–892, 2008.

[94] Jules A Gardener, George Andrew D Briggs, and Martin R Castell. Scanning tunneling microscopy studies of C_{60} monolayers on Au(111). *Physical Review B*, 80(23):235434, 2009.

[95] Ikutaro Hamada and Masaru Tsukada. Adsorption of C_{60} on Au(111) revisited: A van der waals density functional study. *Physical Review B*, 83(24):245437, 2011.

[96] Guillaume Schull and Richard Berndt. Orientationally ordered (7×7) superstructure of C_{60} on Au (111). *Physical Review Letters*, 99(22):226105, 2007.

[97] James K Gimzewski, Silvio Modesti, Christoph Gerber, and Reto R Schlittler. Observation of a new Au(111) reconstruction at the interface of an adsorbed C_{60} overlayer. *Chemical Physics Letters*, 213(3-4):401–406, 1993.

[98] Eric I Altman and Richard J Colton. Nucleation, growth, and structure of fullerene films on Au(111). *Surface Science*, 279(1-2):49–67, 1992.

[99] Wenbo Chen, Jonathan R Widawsky, Héctor Vázquez, Severin T Schneebeli, Mark S Hybertsen, Ronald Breslow, and Latha Venkataraman. Highly conducting π-conjugated molecular junctions covalently bonded to gold electrodes. *Journal of the American Chemical Society*, 133(43):17160–17163, 2011.

[100] Zhanling Cheng, Rachid Skouta, Hector Vazquez, Jonathan R Widawsky, Severin Schneebeli, W Chen, Mark S Hybertsen, Ronald Breslow, and Latha Venkataraman. In situ formation of highly conducting covalent Au-C contacts for single-molecule junctions. *Nature Nanotechnology*, 6(6):353, 2011.

[101] Harold W Kroto, James R Heath, Sean C O'Brien, Robert F Curl, and Richard E Smalley. C_{60}: Buckminsterfullerene. *Nature*, 318(6042):162, 1985.

[102] Frank Rioux. Quantum mechanics, group theory, and C_{60}. *Journal of Chemical Education*, 71(6):464, 1994.

[103] Robert D Johnson, Gerard Meijer, and Donald S Bethune. C_{60} has icosahedral symmetry. *Journal of the American Chemical Society*, 112(24):8983–8984, 1990.

[104] Ryan Yamachika. *Probing atomic-scale properties of organic and organometallic molecules by scanning tunneling spectroscopy.* PhD thesis, UC Berkeley, 2009.

[105] Robert F Curl and Richard E Smalley. Probing C_{60}. *Science*, 242(4881):1017–1022, 1988.

[106] Dennis L Lichtenberger, Kenneth W Nebesny, Charles D Ray, Donald R Huffman, and Lowell D Lamb. Valence and core photoelectron spectroscopy of C_{60}, buckminsterfullerene. *Chemical Physics Letters*, 176(2):203–208, 1991.

[107] John H Weaver. Fullerenes and fullerides: photoemission and scanning tunneling microscopy studies. *Accounts of Chemical Research*, 25(3):143–149, 1992.

[108] Susumu Saito and Atsushi Oshiyama. Cohesive mechanism and energy bands of solid C_{60}. *Physical Review Letters*, 66(20):2637, 1991.

[109] Q-M Zhang, Jae-Yel Yi, and Jerzy Bernholc. Structure and dynamics of solid C_{60}. *Physical Review Letters*, 66(20):2633, 1991.

[110] Steven G Louie and Eric L Shirley. Electron excitation energies in fullerites: Many-electron and molecular orientational effects. *Journal of Physics and Chemistry of Solids*, 54(12):1767–1777, 1993.

[111] Angelika Kühnle. Self-assembly of organic molecules at metal surfaces. *Current Opinion in Colloid & Interface Science*, 14(2):157–168, 2009.

[112] Yangchun Xie. *An STM study of C_{60} molecule on Au(111): close-packed single layer and magic number clusters.* PhD thesis, University of Birmingham, 2014.

[113] Heekeun Shin, A Schwarze, RD Diehl, Katariina Pussi, Arthur Colombier, Émilie Gaudry, Julian Ledieu, GM McGuirk, LN Serkovic Loli, Vincent Fournée, et al. Structure and dynamics of C_{60} molecules on Au(111). *Physical Review B*, 89(24):245428, 2014.

[114] Pavel Jelínek. High resolution spm imaging of organic molecules with functionalized tips. *Journal of Physics: Condensed Matter*, 29(34):343002, 2017.

[115] Nadine Hauptmann, Fabian Mohn, Leo Gross, Gerhard Meyer, Thomas Frederiksen, and Richard Berndt. Force and conductance during contact formation to a C_{60} molecule. *New Journal of Physics*, 14(7):073032, 2012.

[116] AM Sweetman, Samuel Paul Jarvis, Hongqian Sang, Ioannis Lekkas, Philipp Rahe, Yu Wang, Jianbo Wang, Neil R Champness, Lev Kantorovich, and Philip Moriarty. Mapping the force field of a hydrogen-bonded assembly. *Nature Communications*, 5:3931, 2014.

[117] Akitoshi Shiotari, Takafumi Odani, and Yoshiaki Sugimoto. Torque-induced change in configuration of a single no molecule on Cu(110). *Physical Review Letters*, 121(11):116101, 2018.

[118] Harry Monig, Diego R Hermoso, Oscar Diaz Arado, Milica Todorovic, Alexander Timmer, Simon Schuer, Gernot Langewisch, Ruben Perez, and Harald Fuchs. Submolecular imaging by noncontact atomic force microscopy with an oxygen atom rigidly connected to a metallic probe. *ACS nano*, 10(1):1201–1209, 2015.

[119] Jinbo Peng, Jing Guo, Prokop Hapala, Duanyun Cao, Runze Ma, Bowei Cheng, Limei Xu, Martin Ondráček, Pavel Jelínek, Enge Wang, et al. Weakly perturbative imaging of interfacial water with submolecular resolution by atomic force microscopy. *Nature Communications*, 9(1):122, 2018.

[120] Franz J Giessibl. Atomic resolution of the silicon (111)-(7×7) surface by atomic force microscopy. *Science*, 267(5194):68–71, 1995.

[121] Leo Gross. Recent advances in submolecular resolution with scanning probe microscopy. *Nature Chemistry*, 3(4):273, 2011.

[122] Nikolaj Moll, Bruno Schuler, Shigeki Kawai, Feng Xu, Lifen Peng, Akihiro Orita, Junzo Otera, Alessandro Curioni, Mathias Neu, Jascha Repp, et al. Image distortions of a partially fluorinated hydrocarbon molecule in atomic force microscopy with carbon monoxide terminated tips. *Nano letters*, 14(11):6127–6131, 2014.

[123] Bruno Schuler. *Characterizing and identifying single molecules by scanning probe microscopy using functionalized tips*. PhD thesis, 2015.

[124] Xiaojun Xin, Li-Yong Gan, Michel A Van Hove, Xinguo Ren, Hongyan Wang, Chun-Sheng Guo, and Yong Zhao. Exploring molecules beyond CO as tip functionalizations in high-resolution noncontact atomic force microscopy: A first principles approach. *ACS Omega*, 1(5):1004–1009, 2016.

[125] Alan J Heeger. Semiconducting and metallic polymers: the fourth generation of polymeric materials (nobel lecture). *Angewandte Chemie International Edition*, 40(14):2591–2611, 2001.

[126] Antonio Facchetti. π-conjugated polymers for organic electronics and photovoltaic cell applications. *Chemistry of Materials*, 23(3):733–758, 2010.

[127] Nestor Merino-Diez, Aran Garcia-Lekue, Eduard Carbonell-Sanroma, Jingcheng Li, Martina Corso, Luciano Colazzo, Francesco Sedona, Daniel Sanchez-Portal, Jose I Pascual, and Dimas G de Oteyza. Width-dependent band gap in armchair graphene nanoribbons reveals fermi level pinning on Au(111). *ACS nano*, 11(11):11661–11668, 2017.

[128] Florian Klappenberger, Yi-Qi Zhang, Jonas Bjork, Svetlana Klyatskaya, Mario Ruben, and Johannes V Barth. On-surface synthesis of carbon-based scaffolds and nanomaterials using terminal alkynes. *Accounts of Chemical Research*, 48(7):2140–2150, 2015.

[129] Xin Guo, Martin Baumgarten, and Klaus Müllen. Designing π-conjugated polymers for organic electronics. *Progress in Polymer Science*, 38(12):1832–1908, 2013.

[130] Ewan Smith and Ian Collins. Photoaffinity labeling in target-and binding-site identification. *Future Medicinal Chemistry*, 7(2):159–183, 2015.

[131] Philipp Alexander Held, Harald Fuchs, and Armido Studer. Covalent-bond formation via on-surface chemistry. *Chemistry–A European Journal*, 23(25):5874–5892, 2017.

[132] Shigeki Kawai, Ondrej Krejci, Adam S Foster, Rémy Pawlak, Feng Xu, Lifen Peng, Akihiro Orita, and Ernst Meyer. Diacetylene linked anthracene oligomers synthesized by one-shot homocoupling of trimethylsilyl on Cu(111). *ACS nano*, 12(8):8791–8797, 2018.

[133] Christophe Nacci, Francisco Ample, David Bleger, Stefan Hecht, Christian Joachim, and Leonhard Grill. Conductance of a single flexible molecular

wire composed of alternating donor and acceptor units. *Nature Communications*, 6:7397, 2015.

[134] Qitang Fan, J Michael Gottfried, and Junfa Zhu. Surface-catalyzed C-C covalent coupling strategies toward the synthesis of low-dimensional carbon-based nanostructures. *Accounts of Chemical Research*, 48(8):2484–2494, 2015.

[135] Ignacio Piquero-Zulaica, Aran Garcia-Lekue, Luciano Colazzo, Claudio K Krug, Mohammed SG Mohammed, Zakaria M Abd El-Fattah, J Michael Gottfried, Dimas G de Oteyza, J Enrique Ortega, and Jorge Lobo-Checa. Electronic structure tunability by periodic meta-ligand spacing in one-dimensional organic semiconductors. *ACS nano*, 12(10):10537–10544, 2018.

[136] Someshwar Pola, Chi-Hsien Kuo, Wei-Tao Peng, Md Minarul Islam, Ito Chao, and Yu-Tai Tao. Contorted tetrabenzocoronene derivatives for single crystal field effect transistors: correlation between packing and mobility. *Chemistry of Materials*, 24(13):2566–2571, 2012.

List of Abbreviations

- STM: Scanning Tunneling Microscopy
- AFM: Atomic Force Microscopy
- nc-AFM: Non-contact Atomic Force Microscopy
- STS: Scanning Tunneling Spectroscopy
- LDOS: Local Density of Electronic States
- RT: Room Temperature
- SPM: Scanning Probe Microscopy
- DFT: Density Functional Theory
- LT: Low Temperature
- STHM: Scanning Tunneling Hydrogen Microscopy
- UHV: Ultra-High Vacuum
- VT: Variable Temperature
- DOS: Density of States
- THA: Tersoff - Hamann Approximation
- FM: Frequency Modulation
- AM: Amplitude Modulation
- PLL: Phase-Lock Loop
- CPD: Contact Potential Difference
- vdW: van der Waals
- LEED: Low Energy Electron Diffraction
- QMS: Quadrupole Mass Spectrometer
- NMR: Nuclear Magnetic Resonance
- DSP: Digital Signal Processor
- ADC: Analogue to Digital Converter

- KPFM: Kelvin Probe Force Microscopy
- ES: Electrostatic
- CB: Chemical Bonding
- IGP: Ion Getter Pumps
- TSP: Titanium Sublimation Pumps
- TMP: Turbo Molecular Pumps
- FCC: Face-Centered Cubic
- HCP: Hexagonal Close-Packed
- P-FIB: Plasma Focused Ion Beam
- SEM: Scanning Electron Microscope
- CO: Carbon Monoxide

About author

List of publications

1. A. Sánchez-Grande, B. de la Torre, J. Santos, B. Cirera, K. Lauwaet, T. Chutora, S. Edalatmanesh, P. Mutombo, J. Rosen, R. Zbořil, R. Miranda, J. Bjork, P. Jelínek, N. Martín, D. Ecija. *On-surface synthesis of ethynylene bridged anthracene polymers.* Angewandte Chemie International Edition. (2019).

2. T. Chutora, B. de la Torre, P. Mutombo, J. Hellerstedt, J. Kopeček, P. Jelínek, M. Švec. *Nitrous oxide as an effective AFM tip functionalization: a comparative study.* Beilstein Journal of Nanotechnology, 10(1), 315-321., 2019.

3. J. Hellerstedt, A. Cahlík, M. Švec., B. de la Torre, M. Moro-Lagares, T. Chutora, B. Papoušková, G. Zoppellaro, P. Mutombo, R. Ruben, R. Zbořil and P. Jelínek. *On-surface structural and electronic properties of spontaneously formed Tb_2Pc_3 single molecule magnets* Nanoscale, 10.33: 15553-15563., 2018.

4. I. D. Karbovnyk, I. Olenych, I. N. Kukhta, A. Lugovskii, G. Sasnouski, T. Chutora, A. P. Luchechko, I. Khalakhan, A. Kukhta. *Electric field oriented nanostructured organic thin films with polarized luminescence* Nanoscale Research Letters, 12.1:166, 2017

5. T. Chutora, J. Redondo, B. de la Torre, M. Švec, P. Jelínek,and H. Vázquez. *Stable Au–C bonds to the substrate for fullerene-based nanostructures* Beilstein Journal of Nanotechnology, 8: 1073, 2017.

Conference participation

1. NanoNet International Workshop, 2016, Prague (Czech Republic).
   STM study of activated fullerene – Au(111) coupling (poster presentation).

2. QMol, Monte Verità, Ascona, (Swetzerland), 2017.
   Simultaneous AFM/STM high-resolution images of PTCDA on Ag(111) with Xenon and CO functionalized tip (poster presentation).

3. Fuerzas y Tunel, Jaca (Spain), 2018.
   Nitrous oxide: a suitable new tip functionalization for sub-molecular resolution with STM/AFM (oral presentation).

4. ICN+T, Brno (Czech Republic) 2018.
   Nitrous oxide: a suitable new tip functionalization for sub-molecular resolution with STM/AFM (oral presentation).

5. SPM workshop 2019 (Czech Republic) 2019.
   On-surface synthesis of ethynylene bridged anthracene polymers. (oral presentation).